Structure and Dynamics of HIV-1 Env trimer

Thesis by

Haoqing Wang

In Partial Fulfillment of the Requirements for the degree of

Doctor of Philosophy

CALIFORNIA INSTITUTE OF TECHNOLOGY

Pasadena, California

2019

(Defended December 14, 2018)

Haoqing Wang

ORCID: 0000-0003-0277-3018

ACKNOWLEDGEMENTS

I would like to thank my advisor Prof. Pamela Bjorkman for her mentorship. She is a role model scientist, always critical thinking, always honest, and always high standard. We argue a lot but I still believe (or at least I hope) these arguments all end up as enlightening scientific discussion. With that we were able to drive some progresses in the field of HIV structural biology and I feel proud of them. Besides, she is extremely supportive of my career. I hope she can keep supporting me in the future.

I would also like to thank other faculty members on my thesis committee as well: Prof. William "Bil" Clemons, Prof. Grant Jensen, and Prof. Doug Rees. Bil has always been a thoughtful coordinator for all BMB graduate students and he gave me a lot of support. Grant is also a tough mentor and thanks to him I can have a solid electron microscopy background. Doug, as the nicest person on my committee, offered me advice in and out of science. I feel very fortunate to have them on my committee.

I thank all the Bjorkman lab members. Literally everyone has helped me somehow throughout the past 5 years. Dr. Rachel Galimidi took me into the lab after my rotation. Dr. Louise Scharf has introduced me to the Env trimer structural biology world. After that, I'm fortunate to work with an amazing team of experts, including direct collaborators Dr. Harry Gristick, Dr. Christopher Barnes, Dr. Anthony West, Dr. Beth Stadtmueller, Dr. Stuart Sievers, Alex Cohen, Zhi Yang, and Han Gao. Besides, other lab members, including Dr. Jennifer Keefe, Dr. Yunji Wu, Dr. Andrew Flayk, Dr. Aaron Coey, Dr. Collin Kieffer, Dr. Gwen Owens, Dr. Blaise Ndjamen Mark Ladinsky, Morgan Abernathy, Kim Dam, Shannon Esswein, Magnus Hoffman, Pri Gnanapragasam, Beth Huey-Tubman, Erica Lee, Alisa Voll, Stone Jiang, Albert Liu, and many many others that I must forget. I'm really glad to join Bjorkman lab and have the chance to work with such an amazing team.

I would like to thank specific members of Jensen and Rees lab, including Dr. Alasdair McDowall, Dr. Songye Chen, Dr. Andrey Malyutin, Dr. Elitza Tocheva, Dr. Matt Swulius, Dr. Yiwei Chang, Dr. Ariane Briegel, Dr. Limei Zhang, Dr. Jens Kaiser, Sara Weaver, Belinda Wenke, Chengcheng Fan. Besides, I really want to say that my research benefits a lot from the collaborative environment at Caltech, a lot of people such as Dr. Jost Vielmetter and the whole PEC team,

Shyam Saladi, Shuai Wang, and Welison Floriano have solved my problems many times. I feel really fortunate to be able to do my PhD at Caltech.

I also want to thank many collaborators outside Caltech. I want to thank our long-term collaborator Dr. Michel Nussenzweig at Rockefeller University and Dr. Natalia Freund in his lab. I've learned a lot about cryo-EM and collected a lot of data at Janelia farm with the help of Dr. Zhiheng Yu, Dr. Chuan Hong, Dr. Rick Huang, and Dr. Huiting Chou. Dr. Gabriel Lander, Dr. Kelly Dryden, and many others have given me useful cryo-EM advice and suggestions as well.

Many people have persuaded me directly or indirectly to pursue a scientific career during my undergraduate. Prof. Zhihong Guo, my undergrad thesis supervisor, has taught me a lot about organic chemistry, enzymology, and crystallography. Prof. King-Lau Chow, my undergrad program coordinator, has taught me the responsibility of being a scientist to your colleagues and to the general public. Prof. Virginia Cornish at Columbia University and Prof. Ed Chapman at University of Wisconsin Madison took me in their labs while I was an exchange student. Other names on the list include my hands-on trainers Dr. Xiaolei Chen, Dr. Haigang Song, Dr. Chaoran Jing, and Dr. Zhao Wang.

I want to give a special thank to Dr. Minhui Su. She has given me a lot of helpful scientific and career advice throughout the past 9 years. She always tells me to follow my interest rather than the trend and do beneficial research to the community. I've learned a lot from her and hopefully we can collaborate more in the future at Stanford.

Finally I want to thank my parents, Dr. Chengxia Wu and Juhou Wang, to whom I dedicate this thesis. They've given me enough freedom to pursue my interest while giving me economic support. I am forever grateful.

ABSTRACT

The human immunodeficiency virus-1 (HIV-1) infects CD4+ helper T cells by fusing its lipid membrane to the host cell plasma membrane. HIV-1 Envelope (Env) glycoprotein, a trimer of gp120-gp41 heterodimers, is the fusion machinery that mediates viral and host cell membrane fusion, which is initiated by interaction between the host cell receptor CD4 and viral glycoprotein gp120. Receptor binding induces conformational changes in the Env trimer such that coreceptor CCR5/CXCR4 can bind to gp120 and trigger subsequent membrane fusion steps. Previous cryo-electron tomography (cryoET) and spectroscopy studies have shown that CD4 binding induces changes in Env trimer from the closed, prefusion conformation to an open, CD4-bound conformation. However, the CD4-bound Env trimer is dynamic and flexible such that structural biology study of CD4-bound Env trimer is difficult.

As the sole glycoprotein located on HIV-1 viral surface, Env trimer is the only target for neutralizing antibodies. Since HIV-1 mutates rapidly, most neutralizing antibodies are strain-specific. However, a small percent of HIV-1 infected patients can develop broadly neutralizing antibodies (bNAbs) that neutralize a wide spectrum of viruses. In 2011, our collaborator isolated a bNAb called 8ANC195. To understand how 8ANC195 recognizes Env trimer and prevents infection, we used a combination of structural biology and biochemistry tools. Interestingly, we found that 8ANC195 can recognize Env trimer in both its prefusion and CD4-bound conformations by targeting an epitope at gp120-gp41 interface. Furthermore, 8ANC195 stabilizes the Env-CD4 complex, allowing us to investigate the conformational changes induced by CD4 in atomic resolution. By solving and comparing single-particle cryo-EM structures of Env trimer in complex with CD4 and/or antibodies, we found that: 1) CD4 binding induces coreceptor binding site exposure through a β-sheet rearrangements in each gp120 monomer. Several key residues allosterically regulate this coreceptor binding site exposure. 2) CD4 binding induces Env trimer opening together with gp41 conformational changes, which represents an intermediate between prefusion gp41 and postfusion gp41. 3) Env trimer opening is necessary but not sufficient for coreceptor binding site exposure, while CD4 binding induces both, some antibodies can open Env trimer without exposing the coreceptor binding site. These conclusions further illuminate how Env trimer mediates membrane fusion and inform potential strategies blocking viral entry.

PUBLISHED CONTENT AND CONTRIBUTIONS

Wang, Haoqing*, Christopher O. Barnes*, Zhi Yang, Michel C. Nussenzweig, and Pamela J. Bjorkman. "Partially Open HIV-1 Envelope Structures Exhibit Conformational Changes Relevant for Coreceptor Binding and Fusion." *Cell host & microbe* 24, no. 4 (2018): 579-592.
doi: 10.1016/j.chom.2018.09.003
H.W. participated in the conception of the project, prepared cryo-EM samples, collected and processed cryo-EM data, solved and analyzed structures, and prepared the manuscript.

Gristick, Harry B., Haoqing Wang, and Pamela J. Bjorkman. "X-ray and EM structures of a natively glycosylated HIV-1 envelope trimer." *Acta Crystallographica Section D 73*, no. 10 (2017): 822-828.
doi: 10.1107/S2059798317013353
H.W. analyzed the structure and prepared the manuscript.

Wang, Haoqing, Harry B. Gristick, Louise Scharf, Anthony P. West Jr, Rachel P. Galimidi, Michael S. Seaman, Natalia T. Freund, Michel C. Nussenzweig, and Pamela J. Bjorkman. "Asymmetric recognition of HIV-1 Envelope trimer by V1V2 loop-targeting antibodies." *Elif*e 6 (2017): e27389.
doi: 10.7554/eLife.27389.001
H.W. participated in the conception of the project, prepared EM samples, collected and processed EM data, solved and analyzed structures, and prepared the manuscript.

Freund, Natalia T., Haoqing Wang*, Louise Scharf*, Lilian Nogueira, Joshua A. Horwitz, Yotam Bar-On, Jovana Golijanin et al. "Coexistence of potent HIV-1 broadly neutralizing antibodies and antibody-sensitive viruses in a viremic controller." *Science translational medicine* 9, no. 373 (2017): eaal2144.
doi: 10.1126/scitranslmed.aal2144
H.W. prepared negative-stain EM samples, collected and processed negative-stain EM data, solved and analyzed structures, and prepared the manuscript.

Wang, Haoqing, Alexander A. Cohen, Rachel P. Galimidi, Harry B. Gristick, Grant J. Jensen, and Pamela J. Bjorkman. "Cryo-EM structure of a CD4-bound open HIV-1 envelope trimer reveals structural rearrangements of the gp120 V1V2 loop." *Proceedings of the National Academy of Sciences* 113, no. 46 (2016): E7151-E7158.
doi: 10.1073/pnas.1615939113
H.W. participated in the conception of the project, prepared cryo-EM samples, collected and processed cryo-EM data, solved and analyzed structures, and prepared the manuscript.

Scharf, Louise, Haoqing Wang, Han Gao, Songye Chen, Alasdair W. McDowall, and Pamela J. Bjorkman. "Broadly neutralizing antibody 8ANC195 recognizes closed and open states of HIV-1 Env." *Cell* 162, no. 6 (2015): 1379-1390.
doi: 10.1016/j.cell.2015.08.035
H.W. prepared negative-stain EM and cryo-ET samples, collected and processed negative-stain EM and cryo-ET data, solved and analyzed structures, and prepared the manuscript.

TABLE OF CONTENTS

Chapter 1

Introduction

HIV-1 Env mediated membrane fusion

The human immunodeficiency virus (HIV) is a single-stranded, positive-sense, enveloped RNA virus. It causes HIV infection and eventually leads to acquired immunodeficiency syndrome (AIDS). Between the two species of HIV (HIV type I or HIV-1 and HIV type II or HIV-2), HIV-1 has been the major cause of HIV infections globally and remains a thread to public health, while HIV-2-infected patients remain mostly asymptomatic, with low plasma viral loads (Kanki et al., 1994). HIV-1 targets CD4+ helper T cells, which regulate the activity of B cells and cytotoxic T cells in adaptive immune system (Murphy and Reiner, 2002). Viral infection happens through fusion of the viral and host cell lipid bilayers to allow the HIV-1 capsid and its genetic material to enter the target cell. Then the viral RNA genome is reversely transcribed into proviral DNA, which is then integrated into host cell genome (Laskey and Siliciano, 2014). Following that, integrated DNA is transcribed into viral RNA, which is then translated into viral proteins using host cell machinery inside cytoplasm. Viral proteins assemble with the viral RNA genome at the cell surface and release through membrane budding to produce immature virions. The budding event is mediated by the host ESCRT (endosomal sorting complexes required for transport) machinery (Sundquist and Kräusslich, 2012). Imature virions mature via proteolytic processing mediated by the viral protease, which ultimately results in mature virions that are capable of infecting new cells (Freed, 2015) (Figure 1.1).

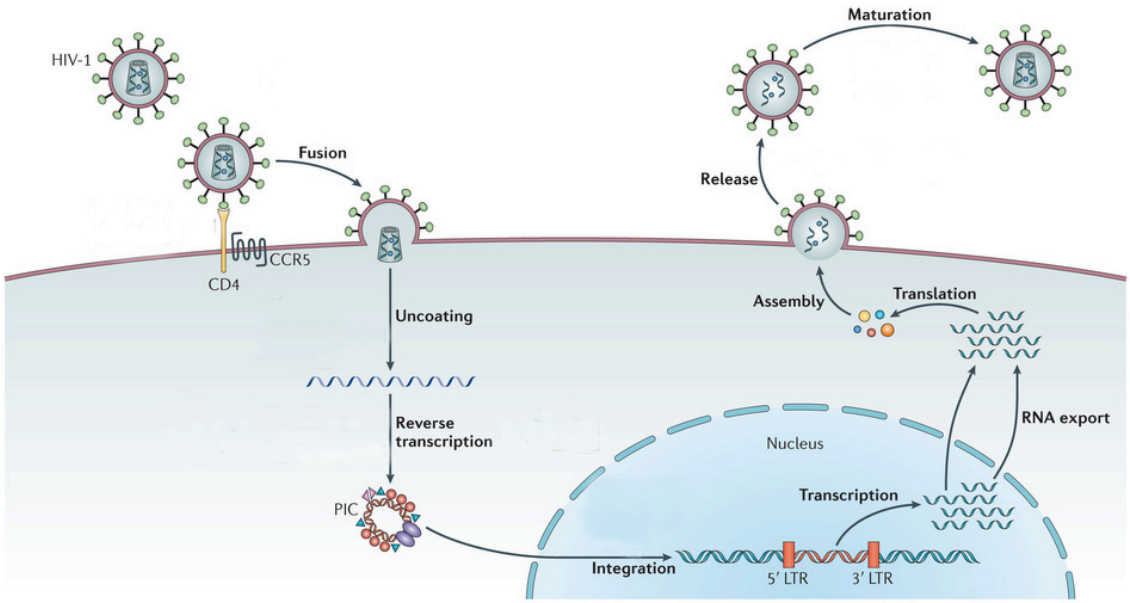

Figure 1. 1. HIV life cycle. Adapted from (Barre-Sinoussi et al., 2013).

Viral and host cell membrane fusion is accomplished by the HIV-1 Envelope (Env) trimer, a class I viral fusion protein and the sole glycoprotein located on HIV-1 lipid membrane surface (Harrison, 2015). Env trimer is encoded by *env* gene in HIV-1 genome. The mature, full-length product of the *env* gene is a homotrimer of heterodimers. Each heterodimer contains two subunits, the extracellular surface protein gp120 and the membrane-associated gp41. While inside the target cell cytoplasm, the *env* gene encodes gp160 protein, which is cleaved by the host cell protease furin, into gp120 and gp41. In the mature, active form of Env trimer, three gp120s and three gp41s are non-covalently associated to serve as a functional fusion protein. The gp120 subunit contains receptor and coreceptor binding sites, and is thus responsible for receptor and coreceptor binding. The gp41 protein, which can be further divided into ecto domain, transmembrane domain (TM) and cytoplasmic tail (CT), will undergo conformational changes upon receptor/coreceptor binding and leads to membrane fusion through a spring loaded mechanism (Carr and Kim, 1993). The HIV-1 Env trimer mediated membrane fusion is similar to other class I viral membrane fusion such as influenza hemagglutinin mediated membrane fusion. Receptor binding initiates fusion process. After that, the fusion peptide from gp41 will be inserted into host cell membrane, and thus creating the pre-hairpin conformation. From the pre-hairpin conformation, gp41 will undergo further

conformational changes to form helical bundles. During this process the target cell membrane and viral membrane will also be brought closer and lead to hairpin formation. The formation of multiple gp41 helical bundles is needed for a fusion pore to form. Finally, the target cell membrane and viral membrane are fused together and gp41 will switch into postfusion conformation, in which the fusion peptides and TM regions likely interact with each other (Chan and Kim, 1998).

Typically, the very first step during HIV-1 infection is gp120 binding to host cell receptor CD4. CD4 binding will induce conformational changes of Env that expose the binding site for coreceptor, either CC-chemokine receptor 5 (CCR5) or CXC-chemokine receptor 4 (CXCR4). Studies have suggested that the HIV-1 can infect target cell through a CD4-independent manner in which the coreceptor-binding site is constantly exposed (Endres et al., 1996; Hoffman et al., 1999). Nevertheless, for most HIV-1 strains the coreceptor binding site on gp120 is occluded during the prefusion state such that CD4 binding is required to induce the conformational changes that are necessary for coreceptor binding and membrane fusion initiation. Coreceptor binding will induce further conformational changes, including insertion of fusion peptide into target cell membrane (Kong et al., 2016), gp120 dissociation (Moore et al., 1990), etc. Eventually, these conformational changes will lead to fusion of the two lipid bilayers (Pancera et al., 2017).

As mentioned above, HIV-1 Env trimer belongs to the classic, and still best characterized class I viral fusion protein. Other examples include influenza virus hemagglutinin (HA) and MHV spike glycoprotein (Harrison, 2015; Walls et al., 2016; Walls et al., 2017). Figure 1. 2 shows the closed, prefusion and postfusion conformation of HIV-1 Env and the presumed sequence of states that links the two conformations. One signature state representing the transition is the prehairpin intermediate, in which the fusion peptide at the N-terminus of gp41 inserted into the target membrane, creating a bridge between the two bilayers destined to fuse. Evidence for this

intermediate is indirect (Chan and Kim, 1998).

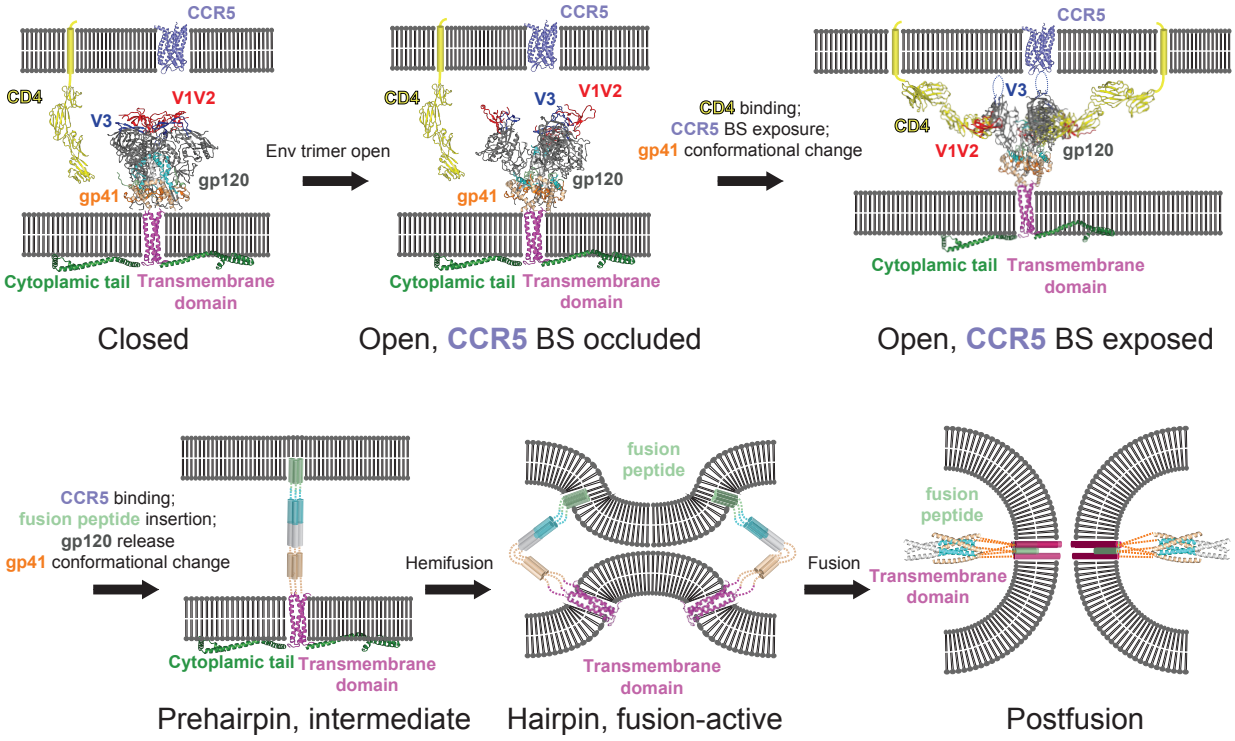

Fig 1. 2. Schematic diagram of HIV-1 Env mediated membrane fusion.

Broadly Neutralizing Antibodies

As the sole glycoprotein on HIV-1 virion surface, Env trimer is the only target for neutralizing antibodies. Several features of Env trimer enable HIV-1 to evade human antibody response. First, HIV-1 mutates at a high rate and produces diverse Env variants in infected people, resulting in a continuing race between newly developed antibodies and the rapidly mutating Env trimer (Roberts et al., 1988). This extraordinary potential enables HIV-1 to escape from developing antibodies. Secondly, the many N-linked glycans covering the surface of Env form a shield that reduces access to protein epitopes. These glycans are attached by the same host cell machinery as host glycoproteins, and thus usually indistinguishable from host glycans, impeding development of neutralizing antibodies targeting glycans (Scanlan et al., 2007). Thirdly, conformational masking of conserved functional sites on Env trimer diminishes the effects of antibodies that

target these regions by restricting access (Kwong et al., 2002). For example, the coreceptor-binding site is not exposed until gp120 is engaged by CD4 receptor (Trkola et al., 1996). Similarly the fusion machinery in the membrane-proximal external region (MPER) of gp41 is not exposed until the fusion process begins. Last but not least, the potency of antibodies is reduced by their limited ability to bind with avidity to the small number of spikes on viral surface (Klein and Bjorkman, 2010). While most viruses present dense arrays of antigens, HIV-1 displays only ~14 Env trimers per virion (Zhu et al., 2006). The sparse distribution of Env trimers makes it difficult to achieve bivalent antibody binding to two adjacent spikes. Furthermore, the Env trimer geometry generally prevents bivalent antibody binding to epitopes on adjacent monomers in the same trimer. This idea is supported by the small differences between IgG potency and Fab potency of HIV-1 antibodies (Klein and Bjorkman, 2010).

However, a small percentage of HIV-1-infected individuals can still produce antibodies that neutralize a broad range of viral strains. By targeting CD4-binding site, MPER, and the variable loops, these antibodies neutralize multiple lab-adapted and primarily isolated HIV-1 strains with low potency. These broadly neutralizing antibodies (bNAbs) establish the principle that antibodies to HIV-1 can have neutralization breadth (Burton et al., 1994).

With the introduction of single-cell cloning techniques, new bNAbs have been cloned from B cells of infected patients (Scheid et al., 2009). The best of these are two to three orders of magnitude more potent than the previously characterized antibodies and can still neutralize up to 90% of the HIV-1 strains tested. The targets of these new antibodies can be divided into the following major groups: (1) CD4-binding site, (2) MPER, (3) V1V2 loop located at the apex of Env trimer, and (4) V3 loop, which contains the coreceptor bindng site and partially shielded by V1V2 loop. In addition, there are yet to be defined conformational epitopes, e.g., antibody 3BC176 (Klein et al., 2012a) (Figure 1.3).

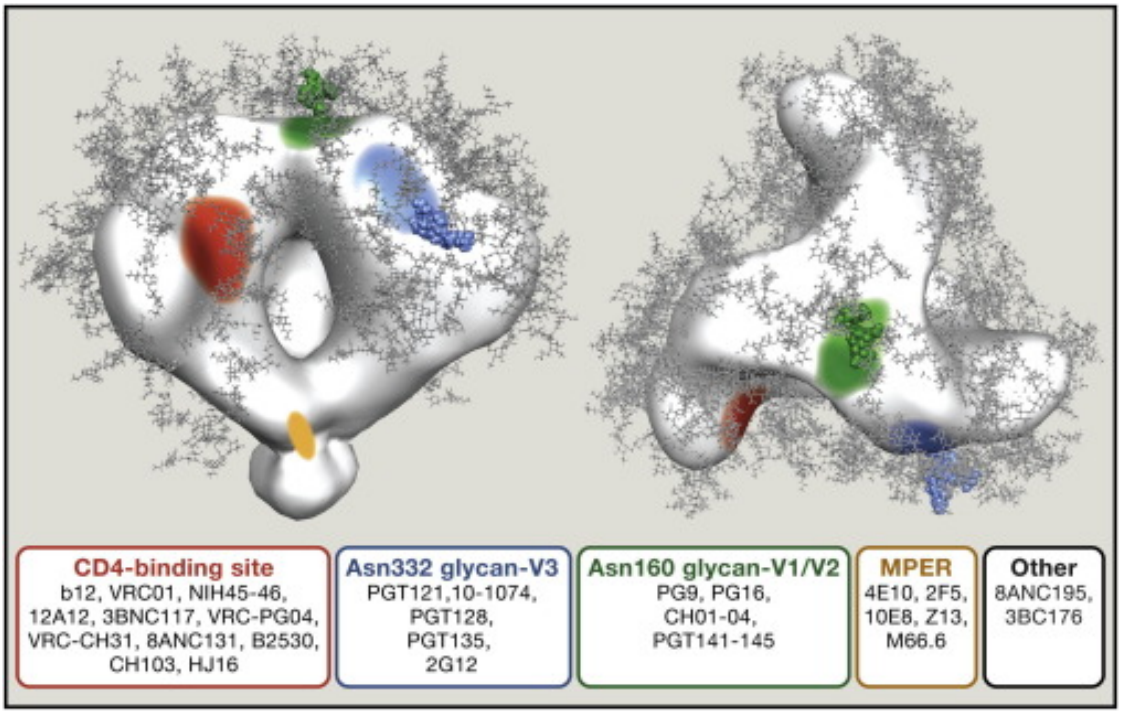

Figure 1.3. Major groups of epitopes of bNAbs on HIV-1 Env. Adapted from (West et al., 2014)

It has been shown that HIV-1 infection in humanized mice can be blocked by passive transfer of bNAbs (Klein et al., 2013b). Therefore, it is believed that a vaccine that can elicit bNAbs would be effective in preventing HIV-1 infection. However, extensive experiments in animal models and clinical trials in humans failed to elicit bNAbs by vaccination (McCoy and Weiss, 2013). Molecular characterization of bNAbs and their interactions with Env trimer has provided clues to understand why these antibodies are difficult to elicit. First, many bNAbs have unusually long CDRH3 loops. For example, In humans the average CDRH3 is 16 residues (Tiller et al., 2007), but in bNAb PGT145 the CDRH3 is 33 residues. These antibodies with very long CDRH3 loops are frequently deleted at the first tolerance checkpoint (Meffre et al., 2001). Another feature shared by all bNAbs is a high degree of somatic hypermutation. Most affinity-matured human V_H domains carry 15–20 somatic mutations at the nucleotide level (Tiller et al., 2007), while bNAbs are generally more extensively mutated (Scheid et al., 2009). These mutations are essential for the binding and neutralizing activity of the bNAbs since reverting the antibodies to their germline coding sequence results in loss of neutralizing activity (Klein et al., 2013a).

Interestingly, bNAbs are frequently polyreactive, but they appear to be not removed (Haynes et al., 2005) even though polyreactive antibodies are supposed to be removed from the B cell repertoire during development (Wardemann et al., 2003). One possible explanation is that the low viral surface density of Env trimer and Env trimer geometry prevent bivalent binding. Therefore, polyreactivity is selected to provide a second binding interaction for bNAbs and thus improve avidity effects (Mouquet et al., 2010).

The interactions between bNAbs and Env trimer have been intensively investigated in molecular details by biochemistry and structural biology. Unfortunately, the initial attempt of eliciting bNAbs in animal models using immunogens designed based on these interactions failed (Burton et al., 2012; Kwong and Mascola, 2012). One problem of the design is that the germline precursors of bNAbs do not bind to Env trimer with high affinity (Klein et al., 2013a). Therefore, these immunogens were not able to recruit B cells producing bNAb precursors such that they failed to induce expected immune responses. New strategies have been proposed in order to overcome this issue. For example, germline antibody recognition of HIV-1 immunogens has been studied to design new immunogens that can bind to both bNAbs and their precursors with high affinity (Scharf et al., 2016). Besides, immunologists are searching for bNAbs with lower degree of somatic hypermutation while maintaining reasonable breadth and potency. These antibodies are potentially better targets to elicit (Gristick et al., 2016).

In collaboration with Michel Nussenzweig's molecular immunology group at Rockefeller University, I'm involved in a long-term team effort to characterize new bNAbs isolated from HIV-1 infected patients using structural biology and biochemistry. Using single particle cryo-EM and cryoET, I've not only discovered novel epitopes on Env trimer targeted by these new bNAbs, but demonstrated the molecular mechanism of their neutralizing activity as well (Freund et al., 2017; Wang et al., 2017). These studies add new descriptions of the host immune response to HIV and provide critical information for vaccine design.

Conformational changes of Env

As the sole glycoprotein on HIV-1 membrane surface, Env trimer is responsible for both receptor/coreceptor binding and membrane fusion. In order to perform these sophisticated functions, Env trimer, including both gp120 and gp41, adopt different conformations in different stages throughout the membrane fusion process.

Low-resolution subtomogram averaging structures of Env trimers on HIV-1 virions revealed distinct Env conformations including the prefusion, closed conformation in which Env trimer is unliganded and a soluble CD4 (sCD4)-bound, open conformation in which the gp120 subunits were displaced and outwardly rotated to disrupt the interaction at the trimer apex (Liu et al., 2008). Subsequent crystallography and single particle cryo-EM studies of native-like Env trimers lacking TM regions and cytoplasmic tails and with stabilizing mutations (SOSIPs) (Sanders et al., 2013) resulted in higher-resolution Env structures of the prefusion conformation. These structures revealed how gp120 V1V2 loops interact at the trimer apex and shield the coreceptor binding site on V3 loops (Ward and Wilson, 2017). Later on, advances in single particle cryo-EM enabled the solution of sCD4-bound SOSIPs structures at near atomic resolution. (Ozorowski et al., 2017; Wang et al., 2018; Wang et al., 2016a). Consistent with subtomogram averaged structures of sCD4-bound Envs on virion surface (Liu et al., 2008), high resolution single-particle cryo-EM structures of sCD4-bound SOSIPs demonstrated rotation and displacement of gp120s, an ~40Å movement of V1V2 to the sides of Env trimer to expose the coreceptor binding site on V3, and minor rearrangements of gp41.

The conformational states of HIV-1 Envs has been studied by single-molecule Förster resonance energy transfer (smFRET), in which donor and acceptor fluorophores were placed within a gp120 monomer in a Env trimer on virion surface, allowing intra-subunit dynamics of Env trimers to be monitored over time (Ma et al., 2018; Munro et al., 2014; Munro and Lee, 2018; Munro and Mothes, 2015). These studies suggested that Env trimers transition between three states (States 1, 2, and 3), with State 1 corresponding to unliganded state. Adding antibodies or small molecule HIV-1 entry inhibitors (Li et al., 2013) stabilized State 1 (Munro et al., 2014). Unfortunately, due to the size and flexibility of fluorophores, distances measured in smFRET cannot be directly correlated

with Env structures, resulting in a gap in understanding the relationship between Env structure and dynamics. In addition, most atomic-resolution Env structures were solved using SOSIP Envs, while the smFRET studies were mainly done on virion-bound Envs. Within the 20Å resolution limitation (Liu et al., 2008), the closed and open conformations of native Envs on virion surface revealed by cryo-ET superimpose with closed and open conformations of SOSIP Envs. But whether SOSIP Envs structures represent the biologically relevant conformations adopted by virion-bound Envs still requires detailed assessment.

The conformational states of SOSIP Envs have also been investigated by double electron-electron resonance (DEER) spectroscopy, in which the SOSIP Envs were spin-labeled with a nitroxide free radical (Stadtmueller et al., 2018). In DEER spectroscopy, size and flexibility of probes are minimized so that the distances measured can be directly correlated with structures. The DEER measurements of unliganded SOSIP Envs show consistence with closed structures. Furthermore, the distance distribution diagram demonstrated homogeneity at Env trimer apex and flexibility near Env trimer base, and thus suggested decoupling between the base and apex. After adding CD4, the distances distribution suggested increased inter-subunit distances and heterogeneity, consistent with conformational changes required for coreceptor binding. These results indicate that SOSIP Envs show similarities with Envs on native virions.

Summary

Although our understanding of Env trimer structures and dynamics has increased tremendously over the last decade, there are many questions that remain unanswered. For instance, what conformational changes induced by CD4 allow coreceptor to bind, i.e., what is the structural basis of coreceptor binding site exposure? The work presented here answers this fundamental question by providing high-resolution structures of CD4-bound Env trimer and gives insight into the mechanism of Env trimer mediated membrane fusion. Chapter 2 presents the cryoET and negative stain EM structures of Env trimer in CD4-bound, coreceptor binding site-exposed conformation. These structures not only showed that 8ANC195, a bNAb isolated from HIV-1 infected patient, can neutralize Env trimer in both prefusion and CD4-bound conformation, but also suggested that 8ANC195 can be used to stabilize CD4-bound Env trimer for structural biology studies. With this

knowledge, Chapter 3 presents two high-resolution structures of Env trimer in CD4-bound conformations. By comparing our structures with other high-resolution Env trimer structures in different conformations, we were able to draw a very interesting conclusion, that the Env trimer opening and coerceptor binding site exposure are two independent steps. Finally, in Chapter 4, we present structural biology studies of BG1, another bNAb isolated from HIV-1 infected donor. The results suggested that BG1 recognize symmetric Env trimer's V1V2 loop in a novel, asymmetric mechanism, demonstrating that there is more diversity in recognizing V1V2 epitope than previously assumed.

In summary, the thesis lead important progress in HIV structural biology field, including (1) proposing a model describing mechanistic details of CD4 induced coreceptor binding site exposure, (2) describing elements of conformational plasticity of Env trimer, especially in CD4-bound conformation, (3) suggesting an order for Env trimer conformational changes, and (4) revealing the structures of V1V2 regions in both prefusion and CD4-bound conformations. These findings further our understanding of Env trimer mediated membrane fusion and indicated how we can block membrane fusion by targeting epitopes on Env trimer.

C h a p t e r I I

Antibody 8ANC195 Targets Env in Both Prefusion and CD4-Bound Conformations

Abstract

Only limited regions on HIV-1 Env contains are epitopes for broadly neutralizing antibodies (bNAbs), those regions are usually conserved regions among all HIV-1 viral strain, and neutralizing antibodies targeting other regions are usually strain specific. The epitope of antibody 8ANC195, defined by crystal structures of monomeric gp120-sCD4-8ANC195 complex and BG505 SOSIP-8ANC195 complex, showed that 8ANC195 binds to the gp120-gp41 interface and insert into a glycan gap. To determine if 8ANC195 recognizes Env in CD4-bound conformation that has been shown as a state before coreceptor binding and fusion, we solved cryoET and negative stain EM structures of an BG505 SOSIP-sCD4-17b-8ANC195 complex. The results suggested 8ANC195 can bind to Env in both prefusion, closed and CD4-bound, open conformations. Furthermore, 8ANC195 binding partially reversed the CD4 induced Env opening, and lead to a previously unseen partially-open conformation. Overall, these discoveries showed that HIV-1 Env can exist in different conformations, confirming its structural plasticity.

Adapted from

Scharf, L., Wang, H., Gao, H., Chen, S., McDowall, A.W., and Bjorkman, P.J. (2015). Broadly Neutralizing Antibody 8ANC195 Recognizes Closed and Open States of HIV-1 Env. Cell *162*, 1379-1390.

Introduction

HIV-1 Env is the glycoprotein located on viral membrane surface. It's a homotrimer of gp120-gp41 heterodimer. Since HIV-1 viruses are assembled within target cells and release through membrane budding, the viral membrane is the same as host cell membrane. Therefore, Env trimer will be the only target of neutralizing antibodies and thus the focus on vaccine design efforts. A small subset of HIV-1 infected patients has developed broadly neutralizing antibodies (bNAbs) targeting conserved epitopes on Env trimer. It has been shown in humanized mouse that bNAbs can prevent and treat infection (Klein et al., 2012b). Moreover, bNAbs exhibited efficacy against HIV-1 in a human clinical trial (Caskey et al., 2015).

Previously, there were four defined bNAbs epitopes on HIV-1 Env trimer: the CD4 binding site epitope, the V1V2 epitope, the V3 epitope, and the gp41 membrane-proximal external region (MPER) (West et al., 2014). In 2014, three bNAbs were discovered to recognize new regions around gp120-gp41 interface, including PGT151 and 35O22, that are subunit-spanning, trimer specific bNAbs (Blattner et al., 2014; Huang et al., 2014), and 8ANC195, that is gp120-gp41-spanning, recogzning both Env trimer and monomeric gp120 (Scharf et al., 2014; Scheid et al., 2011).

Originally, 8ANC195 was isolated in a screen that discovered many bNAbs recognizing CD4 binding site. But 8ANC195's epitope, defined based on neutralization assay, did not match conventional CD4 binding site Abs (Scheid et al., 2011). In 2013, our group applied computational analyses, used neutralization assay data to predict that N-linked glycosylation at position 234 and 276 on gp120 are essential for the neutralizing activity of 8ANC195. The results suggested a model that 8ANC195 fit to a pocket between N-linked glycans at Asn234 and Asn276 and bind to gp120-gp41 interface. After that, our group has solved a crystal structure of 8ANC195 Fab in complex with monomeric gp120 and soluble CD4 (sCD4), further confirmed our previous prediction that 8ANC195 make contacts with N-linked glycans at Asn276 and Asn234, recognizing gp120-gp41 interface region that is not targeted by other bNAbs (Scharf et al., 2014).

In order to further illustrate 8ANC195's epitopes in the context of HIV-1 Env trimer, we used a native-like soluble Env trimer (BG505 SOSIP.664, usually refered to as BG505 SOSIP) (Sanders et al., 2013). We first solved a low resolution, negative stain single particle EM structure of BG505 SOSIP in complex with 8ANC195 to show that the binding pattern of 8ANC195 on Env trimer is the same as it is been shown using monomeric gp120 (Scharf et al., 2014). All together, these data demonstrated that 8ANC195 could bind to Env trimer and neutralize viral activity by preventing CD4-induced conformational changes required for Env mediated membrane fusion, rather than directly binding to CD4 binding site and prevent CD4 from binding.

Because the low resolution negative stain EM structure cannot precisely describe how 8ANC195 recognize residues and glycans on Env trimer, our group went further and solved a crystal structure of BG505 SOSIP in complex with 8ANC195 Fab (Scharf et al., 2015). The structure, at atomic resolution, defined 8ANC195 epitope. Since the previous crystal structure of 8ANC195 in complex with monomeric gp120 was obtained while gp120 was also bound to sCD4, we were interested in whether 8ANC195 can recognize CD4-bound Env trimer as well. Our group applied binding studies using SPR to confirm that 8ANC195 can recognize CD4-bound Env trimers. Thus, it would be either that the conformational changes induced by CD4 did not change 8ANC195 binding site, or 8ANC195's binding is robust enough such that it can accommodate the conformational changes. To further answer this question and visualize the conformational changes induced by CD4, we used 3D EM reconstruction to demonstrate that 1) CD4 binding induced opening on Env trimer, while 8ANC195's epitope regions did not undergo conformational changes during this process 2) 8ANC195 binding partially close Env trimer, leading to a partially-open conformation. These results provide structural biology evidence of 8ANC195 recognizing both closed and open conformational states of HIV-1 Env and suggest its ability to prevent the full opening of Env trimer that is associated with coreceptor binding and viral-host cell membrane fusion.

Results

To elucidate 8ANC195's epitope on CD4-boun Env trimer, we solved cryoET and negative stain EM structures of a more potent 8ANC195 variant, $\gamma52_{HC}\kappa5_{LC}$ (Scharf et al., 2014) (referred to as $8ANC195_{G52K5}$), complexed with BG505 SOSIP, sCD4, and bNAb 17b. We prepared complexes of BG505 SOSIP Env trimers, sCD4, 17b Fab, and $8ANC195_{G52K5}$ Fab for EM structure determination. 17b, as a CD4 induced bNAb, binds to the coreceptor binding site (CoBS) on Env trimer (Sullivan et al., 1998). We added 17b because: 1) binding of 17b Fab to a CD4-bound open trimer would further stabilize the complex in CD4-bound conformation and, 2) With 17b bound, the Env-sCD4 complex is bulkier, potentially provide a more random orientation distribution on EM grids and facilitate 3D reconstruction (Naydenova and Russo, 2017). To ensure that the Env trimers were in CD4-bound conformation before $8ANC195_{G52K5}$ binding, we first purified BG505 SOSIP-sCD4-17b complexes by SEC, added $8ANC195_{G52K5}$ Fab, and then subjected the four-component mixture to SEC again, obtaining stable quaternary complexes, as confirmed by SDS-PAGE (Supplementary Figure 2.1A).

We want to obtain a totally reference-free reconstruction of the BG505 SOSIP-sCD4-17b-$8ANC195_{G52K5}$ complex that excludes presumptions about Env conformation or how ligands were bound. We determined a 23 Å resolution structure by sub-tomogram averaging of cryo-ET data obtained from 3D reconstruction of a tilt series of 2D projections (Figures 2.1A and Supplementary Figure 2.1B-C). With no symmetry imposed, the sub-tomogram-averaged structure showed a 3-fold symmetric particle with densities for three 17b Fabs at the CoBS, three sCD4 molecules, and three $8ANC195_{G52K5}$ Fabs at the gp120-gp41 interface. Since a co-crystal structure of monomeric gp120-sCD4-17b is stable enough to be considered as a rigid body, we can fit gp120-sCD4-17b as a whole into EM structures of CD4-bound Env trimers (Harris et al., 2011; Liu et al., 2008). We first fit the density with gp120-sCD4-17b coordinates (PDB: 1RZK), resulting in a 3-fold symmetric distribution of gp120, sCD4, and 17b. We next fit 8ANC195 Fab (PDB: 4P9M) into three densities at the predicted 8ANC195 epitopes (Figures 2.1A).

To verify the subtomogram averaged structure and obtain more structural details about the complex, we proceeded to determine a negative stain EM structure of BG505 SOSIP-sCD4-17b-8ANC195$_{G52K5}$ by single particle analysis (Figures 2.1B). 3D classification procedure after reference-free 2D classification resulted in selection of approximately half of the initially selected particles from good 2D classes, and the final 3D Refined reconstruction was improved to ~17 Å resolution (Supplementary Figure 2.2C). The negative stain EM structure showed density for three copies of 8ANC195$_{G52K5}$, 17b, and sCD4 bound to BG505 SOSIP, and we again fit the density using coordinates for gp120-sCD4-17b and 8ANC195 Fab structures (Figure 2.1B). The two reconstructions showed similar placements of three gp120s, three sCD4s, and six Fabs (Figure 2.1C). We used the negative stain EM single-particle reconstruction for following analyses and discussions.

By comparing to other Fab- and/or Fab-sCD4-Env structures in different conformations, it is evident that the Env trimer in our BG505 SOSIP-sCD4-17b-8ANC195$_{G52K5}$ complex structure is not in a prefusion, closed conformation (Figure 2.2 and Supplementary Table 2.1). To determine whether the trimer in the EM structure is fully open as seen in some other CD4-bound Env structures, we investigated the positions of 17b Fabs, noting that they are arranged differently in the BG505 SOSIP-sCD4-17b-8ANC195$_{G52K5}$ structure than in open trimer structures (Figures 2.2A and 2.2B) (Harris et al., 2011; Liu et al., 2008; Tran et al., 2012), suggesting that the Env in the BG505 SOSIP-sCD4-17b-8ANC195$_{G52K5}$ complex adopt a new conformation in comparison to other Env structures. To more precisely describe the conformational state of the Env trimer in the BG505 SOSIP-sCD4-17b-8ANC195$_{G52K5}$ complex, we measured distances between a CD4bs residue in each gp120 protomer of the trimer and compared them to the corresponding distances in structures of trimers in different conformational states (Figures 2.2C and Supplementary Table 2.1). This measurement showed that the Env trimer in the BG505 SOSIP-sCD4-17b-8ANC195$_{G52K5}$ structure adopts a previously unseen partially open state conformation that is in between the prefusion, closed conformation and the CD4-bound, open conformation observed for the sCD4/17b-bound open trimer (Merk and Subramaniam, 2013). Thus, addition of 8ANC195$_{G52K5}$ Fab to the BG505 SOSIP-sCD4-17b complex resulted in partial closure of the open trimer, suggesting that stabilized 8ANC195$_{G52K5}$ binding is incompatible with fully open Env

trimer conformation. Therefore, 8ANC195 can block viral infection by partially reversing CD4 induced Env trimer opening, which is an essential conformational change leading to fusion between the viral and host membranes.

Discussion

In addition to recognizing both monomeric gp120 and closed Env trimer, we also provide structural biology evidence that 8ANC195 can bind to Env trimers complexed with sCD4 and the CD4-induced bNAb 17b. CD4 binding normally induces an open conformation of virion-bound and soluble HIV-1 Env trimers involving both translational and rotational movements of gp120 monomers away from the trimer 3-fold axid (Harris et al., 2011; Liu et al., 2008; Tran et al., 2012).

8ANC195, however, binds to both CD4-bound Env trimers and closed Env trimers with similar affinity (Scharf et al., 2015). Suggesting the gp120-gp41 regions it recognizes undergo small or no conformational changes upon CD4 binding.

When Env trimer binds to CD4, 8ANC195 could stabilize a partially open conformation in equilibrium with fully open CD4-bound Env. Taken together with our crystal structure showing a closed 8ANC195$_{G52K5}$-bound Env trimer despite pre-incubation of trimer with sCD4 (Scharf et al., 2015), the observation that the trimer in the BG505 SOSIP-sCD4-17b-8ANC195$_{G52K5}$ complex is partially open, rather than fully open, implies that 8ANC195 prefers binding to the closed trimer. 8ANC195's preference of binding closed trimer suggests that its mechanism of neutralization likely involves preventing the complete conformational change necessary for the trimer to bind co-receptor and/or expose the fusion peptide and fuse with the target cell membrane.

Although our results indicate that 8ANC195 preferentially recognizes closed Env trimers, its ability to recognize other Env conformations suggests that 8ANC195 can neutralize virions regardless of Env conformational state, including virions with constitutively open Env trimer such as those found on CD4-independent strains (White et al., 2011; White et al., 2010). The fact that 8ANC195 can recognize other Env trimer conformations also suggests that, in addition to neutralizing free virions, 8ANC195 could neutralize virions engaged by CD4 at target cell membrane. By neutralizing CD4 engaged virions, 8ANC195 could inhibit cell-to-cell spread of HIV-1, which is most effectively prevented by Abs that bind triggered Env conformations (Abela

et al., 2012). Finally, recent evidence from single-molecule FRET studies (Munro et al., 2014) and molecular ruler measurements of virion-associated Env trimers (Galimidi et al., 2015) suggests that Env on free virions can exhibit multiple conformations, including CD4-bound like, open conformation; thus, recognition of Env states other than the closed state should be useful for neutralization of cell-bound as well as free virions.

The finding that the trimer in our BG505 SOSIP-sCD4-17b-8ANC195$_{G52K5}$ complex structure was partially open, rather than fully open, as observed in previous CD4-, 17b-, and CD4/17b-bound trimer structures (Harris et al., 2011; Liu et al., 2008; Tran et al., 2012), suggests that the trimer re-closed upon 8ANC195 binding. This result implies more structural plasticity of HIV-1 Env than previously assumed. We hypothesize that, when 8ANC195 engages a CD4-bound (open) trimer, it partially recloses the trimer or captures and stabilizes a pre-existing conformation because the complex with a partially open nv trimer is more favorable for Ab binding. This model suggests that CD4 engagement of HIV-1 spike trimers does not lead to an immediate irreversible conformational change. Alternatively, the highly stabilized design of SOSIP trimers may be responsible for the apparent reversibility of CD4-induced conformational changes.

Combinations of bNAbs are being considered for treatment and prevention of HIV-1 infection by passive delivery methods because mixtures of active molecules (bNAbs or small molecule drugs) are required to prevent the appearance of escape mutants in a rapidly mutating virus such as HIV-1 (Horwitz et al., 2013; Klein et al., 2012b). Two or more bNAbs targeting different epitopes are favored because the virus is presumed unable to mutate several potentially conserved sites simultaneously. In addition to targeting gp120-gp41 interface epitope distinct from other known bNAbs, 8ANC195 can accommodate different conformational states (including CD4-bound conformation), making it an attractive candidate for use in combination therapies with bNAbs that (1) do not bind to gp120-gp41 interface, (2) are unable to engage a CD4-bound Env trimer, and/or (3) allow HIV-1 to spread through cell-to-cell transmission, as is the case for potent CD4-binding site Abs in the VRC01 family (Abela et al., 2012). 8ANC195 may also be a target for vaccine development since it targets conserved regions on Env such as gp41 and the Asn276$_{gp120}$ glycan.

Methods

Protein Production and Purification

8ANC195$_{G52K5}$ and 17b Fabs were produced by transient transfection and purified using affinity chromatography and SEC, as described in previous studies (Scharf et al., 2014). sCD4 (domains 1 and 2; residues 1–186 of mature CD4) was produced in baculovirus-infected Hi5 insect cells and was purified using affinity chromatography and SEC, as described previously (Diskin et al., 2011; Scharf et al., 2014). Untagged BG505 SOSIP.664 was constructed, expressed, and purified as described (Sanders et al., 2013). In brief, HEK293-6E cells treated with 5 μM kifunensine (Sigma) were co-transfected with plasmids encoding BG505 SOSIP.664 and soluble furin, and trimers were purified from cell supernatants using a 2G12 immunoaffinity chromatography and SEC.

BG505 SOSIP-sCD4-17b-8ANC195$_{G52K5}$ complex samples were produced by incubating BG505 SOSIP with a 3-fold molar excess of sCD4 and were purified by SEC. The resulting complex was incubated with a 3-fold molar excess of 8ANC195G52K5 Fab and purified by SEC.

Cryoelectron Tomography

Purified BG505 SOSIP-sCD4-17b-8ANC195G52K5 complexes were diluted to 60 μg/ml in TBS immediately before plunge freezing to avoid complex dissociation at low concentration. Quantifoil R2/2 NH2 copper finder grids were vitrified in liquid ethane using a Mark IV Vitrobot (FEI Company) and Tilt series (±60°, 1° angular increments) were collected on a FEI Tecnai G2 Polara transmission electron microscope equipped with 300 keV FEG, a Gatan energy filter, and a Gatan K2 Summit direct detector using the UCSF tomography software package (Zheng et al., 2007) under low-dose conditions (120 e–/Å2 total for the tilt series at ~8 μm underfocus) at a nominal magnification of 41,000× so that each pixel represented 2.6 Å. Tomographic reconstructions and CTF corrections were calculated using IMOD (Kremer et al., 1996). Subtomogram averaging of 1,745 subvolumes was performed using PEET (Nicastro et al., 2006) without an external reference or applying C3 symmetry, resulting in a ~23 Å structure estimated by a 0.143 gold-standard Fourier shell correlation (FSC) calculated using IMOD (Kremer et al., 1996).

Negative-Stain Single-Particle EM

Purified BG505 SOSIP-sCD4-17b-8ANC195$_{G52K5}$ complexes were diluted to 10 μg/ml in TBS immediately before adding 3 μl to a glow discharged ultrathin C film on holey carbon support film, 400 mesh, Cu grids (Ted Pella) followed by cross-linking using glutaraldehyde vapor and staining with uranyl acetate. Data were collected using a FEI Tecnai T12 transmission electron microscope operating at 120 keV equipped with a Gatan Ultrascan 2k × 2k CCD using a 0.5 s exposure time at a nominal magnification of 42,000× at 1 μm defocus, resulting in 2.5 Å per pixel. A total of 23,951 particles were picked using EMAN2.1 (Tang et al., 2007) and RELION (Scheres, 2012), and the CTF correction was done using EMAN2.1. Initial reference-free 2D class averaging was performed using RELION, and the particles were further sorted using 3D classification in RELION. Refinement was conducted using 80 Å low-pass-filtered structures calculated from models of 8ANC195-sCD4-17b docked onto gp120 cores of partially open (PDB: 3DNL) trimer and 7,174 particles with C3 symmetry applied. The resolution of the final reconstruction was ~17 Å calculated with RELION (Scheres, 2012) using a gold-standard FSC and a 0.143 cutoff, as recommended for resolution estimations for single-particle EM reconstructions (Scheres and Chen, 2012). Coordinates from crystal structures were fit into the sub-tomogram averaged or negative-stain single-particle EM structures using UCSF Chimera (Pettersen et al., 2004).

Figures

Figure 2.1

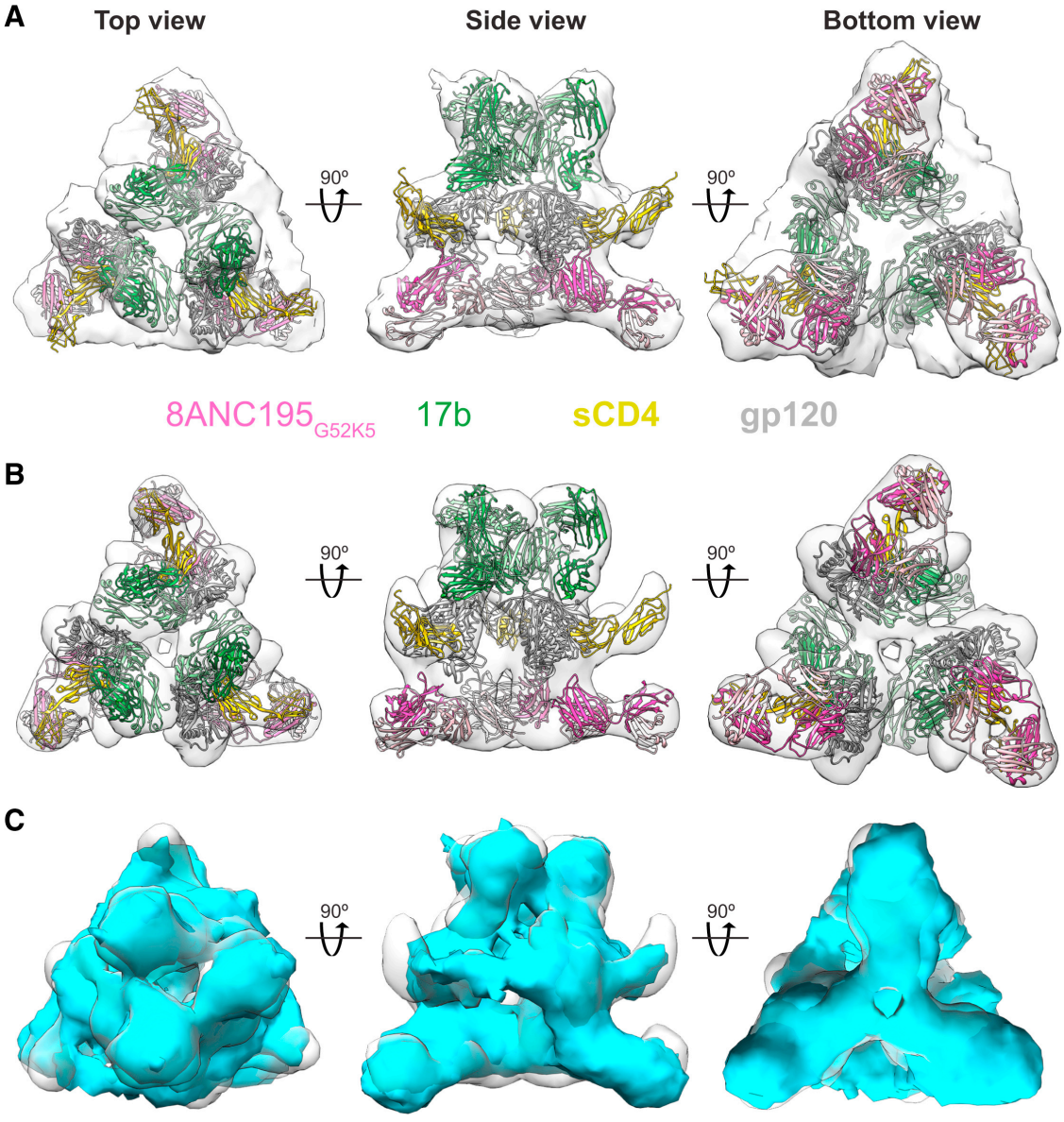

Figure 2.1 EM Reconstructions of BG505 SOSIP-sCD4-17b-8ANC195$_{G52K5}$ Complex

Crystal structures of a monomeric gp120-sCD4-17b complex (PDB: 1RZK) and 8ANC195 Fab (PDB: 4P9M) were fit to EM densities and are shown from top (left), side (middle), and bottom (right).

(A) ~23 Å resolution EM density derived from cryo-ET and sub-tomogram averaging.

(B) ~17 Å resolution EM density derived from negative-stain single-particle reconstruction.

(C) Superposition of densities from cryo-ET/sub-tomogram averaging (cyan) and negative-stain single-particle (light gray) reconstructions.

Figure 2.2

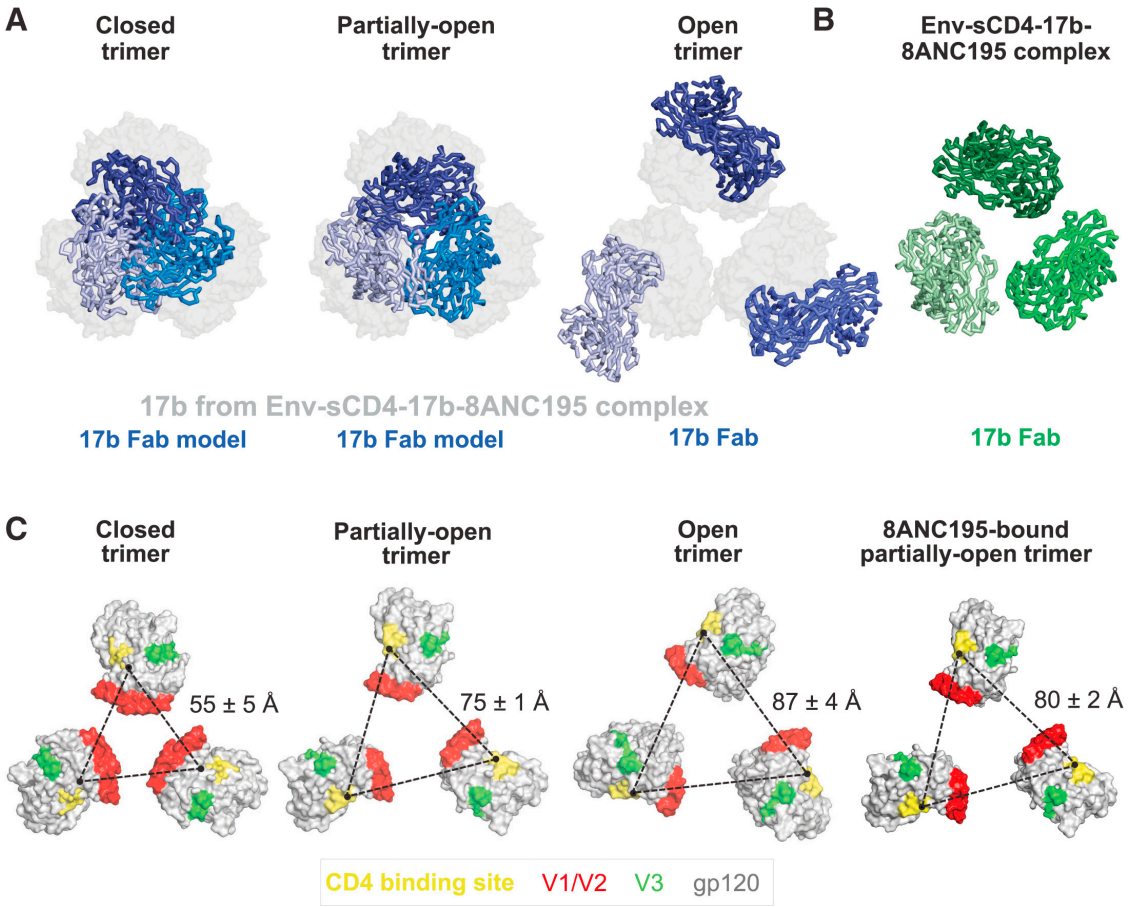

Figure 2.2 Comparison of Different Conformations of Env Trimers in BG505 SOSIP-sCD4-17b-8ANC195G52K5 and Other Env Trimer Complexes Illustrated by 17b and gp120 Positions

(A) Overlay of 17b Fabs from BG505 SOSIP-sCD4-17b-8ANC195G52K5 complex (gray space-filling representations) with 17b Fabs complexed with Env trimers in different conformational states (thick Ca traces in shades of blue). 17b Fabs shown after superimposition of gp120s from trimers (trimers and other ligands not shown). (Left) 17b modeled onto 3DNN coordinates of a closed trimer. (Middle) 17b modeled onto 3DNL coordinates of a partly open trimer. (Right) 17b taken from 3DNO structure of a CD4- and 17b-bound open trimer. Note that three 17b Fabs cannot be accommodated without clashes when modeled onto the gp120s of closed and partly open trimer structures.

(B) Ca trace of the three 17b Fabs from the BG505 SOSIP-sCD4-17b-8ANC195G52K5 complex.

(C) Positions of gp120s (gray space-filling representation with locations of CD4-binding site in yellow, V3 loop in green, and base of V1V2 domain in red) in Env trimers adopting the indicated conformations. The locations of Asp368gp120 are shown as a black dot for each trimer conformation, with the distance between the Cα of this residue in adjacent protomers indicated. Distances are presented as the mean and SD for the analogous distance in representative structures in each conformation.

Supplementary Figures

Supplementary Figure 2.1

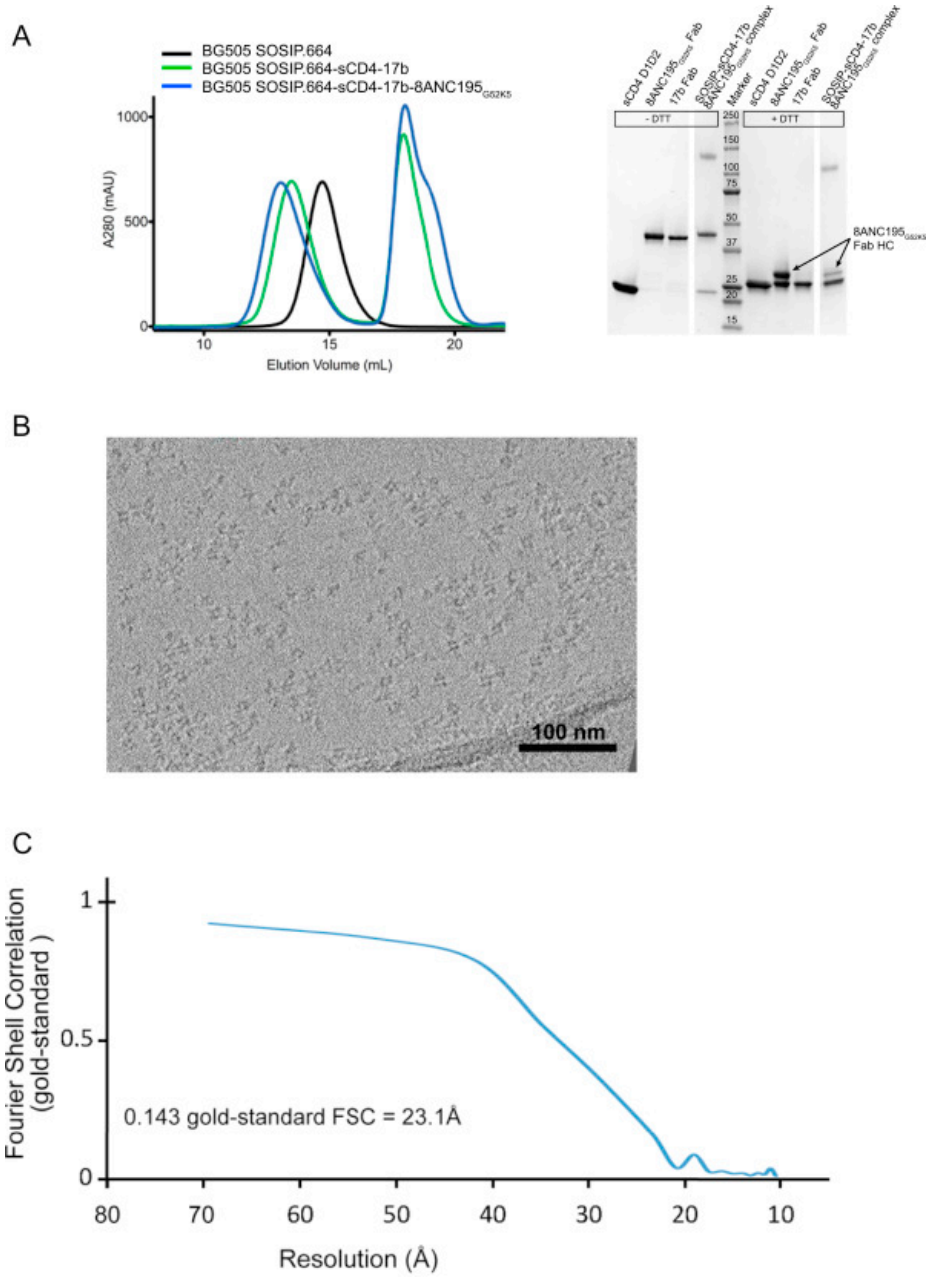

Supplementary Figure 2.1 BG505 SOSIP.664-sCD4-17b-8ANC195G52K5 Complex Analyzed by Cryo-ET and Sub-Tomogram Averaging

(A) Left: Size exclusion chromatography profile and associated SDS-PAGE analysis of fractions for the BG505 SOSIP.664-sCD4-17b-8ANC195G52K5 complex used for EM studies compared with migration of BG505 SOSIP.664 alone and a BG505 SOSIP.664-sCD4-17b complex. Right: SDS-PAGE analysis under non-reducing (-DTT) and reducing (+DTT) conditions to assess complex formation compared with control Fabs and sCD4. Irrelevant lanes were digitally removed as indicated by a space between lanes 3/4 and 8/9 in the panel.

(B) Slice of cryo-EM image volume from samples containing BG505 SOSIP.664-sCD4-17b-8ANC195G52K5 complexes.

(C) Gold-standard Fourier shell correlation (FSC) curve for refinement. The resolution corresponding to the 0.143 FSC cutoff was ~23 Å.

Supplementary Figure 2.2

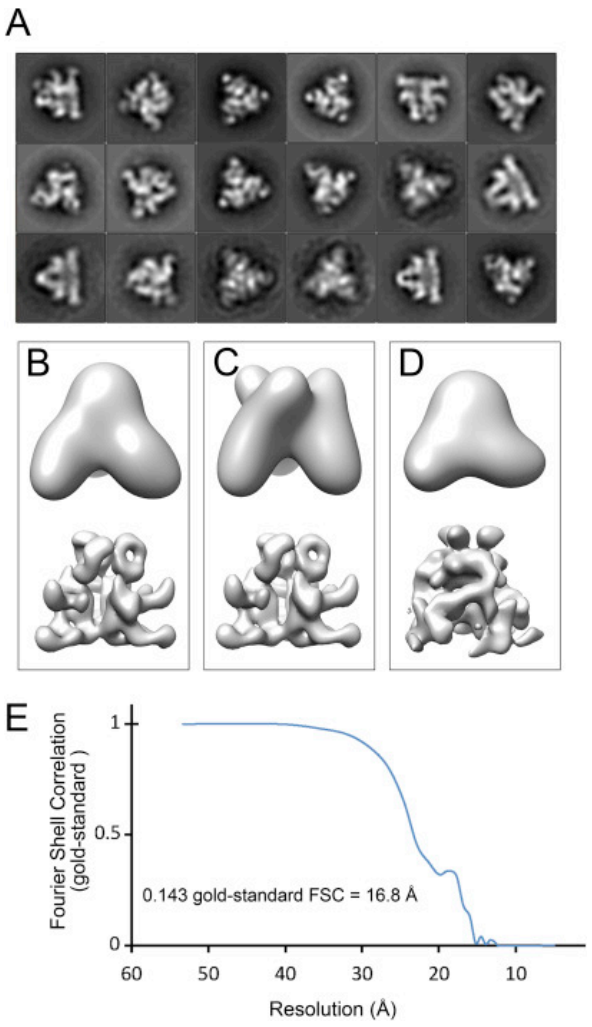

Supplementary Figure 2.2 Negative-Stain EM Data for the BG505 SOSIP.664-sCD4-17b-8ANC195G52K5 Complex

(A) 2D class averages of trimer-sCD4-17b-8ANC195G52K5 complexes. A total of 23,951 particles were picked and 2D class averaging was performed using 2D classification in RELION (Scheres, 2012). The following options were used: Number of classes = 480; Regularization

parameter T = 2; In-plane angular sampling = 5; Offset search range = 5 pixels; Offset search step = 1 pixel.

(B–D) Reference models for refinement were generated using 80 Å low-pass filtered density maps calculated from models of 8ANC195, sCD4, and 17b docked onto partially open (PDB 3DNL) (B); open (PDB 3DNO) (C); or closed (PDB 3DNN) (D) trimer structures. Low-pass filtered reference models are shown at the top of each panel, and the corresponding results after refinement are shown at the bottom. Reference models based on partially open and open structures generated similar structures at < 20 Å resolution, while the model generated with the closed trimer structure did not generate an interpretable structure. The final refinement for the BG505 SOSIP.664–sCD4-17b-8ANC195G52K5 structure was performed using RELION (Scheres, 2012) 3D auto-refine functions with the following options: Reference: as shown in (B) (top); Particle Mask diameter = 320 Å; Symmetry = C3; Mask individual particles with zeros; Initial angular sampling = 7.5 degrees; Initial offset range = 5 pixels; initial offset step = 1 pixel; local searches from auto-sampling = 1.8 degrees. Density for 8ANC195G52K5 Fab was apparent after refinement when starting with an initial reference model that included only sCD4, 17b, and Env trimer (data not shown).

(E) Gold-standard Fourier shell correlation (FSC) curve for refinement. Resolutions corresponding to 0.143 FSC cutoff was 16.8 Å. We used the 0.143 FSC cutoff as recommended for single particle EM reconstruction to report a resolution of ~17 Å for the BG505 SOSIP.664–sCD4-17b-8ANC195G52K5 complex.

Supplementary Tables

Supplementary Table 2.1

Table S5: Distance comparisons in Env trimer structures, Related to Figure 6.

Trimer conformational state	Ligand	+/- sCD4	Trimer type	Method	EMDB/PBD ID	Resolution (Å)	Distance between CD4bs (D368) (Å)
closed	8ANC195$_{G52K5}$	-	BG505 SOSIP.664	crystal structure	this study	3.58	54
closed	PGT122, 35O22	-	BG505 SOSIP.664	crystal structure	4TVP	3.5	55
closed	PGT122	-	BG505 SOSIP.664	crystal structure	4NCO	4.7	56
closed	PG04	-	BG505 SOSIP.664	single particle cryo-EM	3J5M	5.8	53
closed	VRC03	-	KNH1144 SOSIP.681	single particle cryo-EM	4CC8	6	57
closed	VRC01	-	JRFL SOSIP.681	single particle NS EM	6194	20	55
closed	no ligand	-	BaL virion	cryo-ET, sub-tomogram ave	3DNN	20	63
closed	VRC01	-	BG505 SOSIP.664	single particle NS EM	6252	22	61
closed	VRC01		BaL virion	cryo-ET, sub-tomogram ave	5457	24	68
							55 ± 5
partially open	A12	-	BaL virion	cryo-ET, sub-tomogram ave	5544	N/A	75
partially open	b12	-	BaL virion	cryo-ET, sub-tomogram ave	3DNL	20	76
							75 ± 1
partially open*	8ANC195$_{G52K5}$, sCD4, 17b	+	BG505 SOSIP.664	single particle NS EM	this study	17	79
partially open*	8ANC195$_{G52K5}$, sCD4, 17b	+	BG505 SOSIP.664	cryo-ET, sub-tomogram ave	this study	23	82
							80 ± 2
open	sCD4	+	JR-FL SOSIP.681	cryo-ET, sub-tomogram ave	5322	20	94
open	sCD4	+	KNH1144 SOSIP.681	cryo-ET, sub-tomogram ave	5321	20	94
open	sCD4	+	BaL virion	cryo-ET, sub-tomogram ave	5455	24	82
open	sCD4, 17b	+	BaL virion	cryo-ET, sub-tomogram ave	3DNO	20	87
open	sCD4, 17b	+	KNH1144 SOSIP.681	cryo-ET, sub-tomogram ave	5323	20	87
open	sCD4, 17b	+	JR-FL SOSIP.681	cryo-ET, sub-tomogram ave	5324	20	90
open	sCD4, 17b	+	BG505 SOSIP.664	single particle NS EM	5723	22	85
open	17b	-	KNH1144 SOSIP.681	single particle cryo-EM	5462*	8.8	88
open	17b	-	KNH1144 SOSIP.681	cryo-ET, sub-tomogram ave	5325	20	85
open	17b	-	BaL virion	cryo-ET, sub-tomogram ave	5456	22	85
open	17b, VRC01	-	BaL virion	cryo-ET, sub-tomogram ave	5461	28	88
open	Z13e1	-	KNH1144 SOSIP.681	single particle cryo-EM	5680	18.5	83
							87 ± 4

Supplementary Table 2.1 Distance comparisons in Env trimer structures

Env trimer structures are grouped into four conformational states: closed (unliganded and bound to Fabs), partially open (bound to A12 or b12), partially open* (bound to 8ANC195, sCD4, 17b; this study), and open (bound to sCD4 and/or 17b, or Z13e1). The EMDB or PDB identifier is given for each structure. When available, PDB coordinates for gp120 subunits within a trimer were used to measure the distances between CD4 binding site residue Asp368gp120 on adjacent protomers

(PDB coordinates for EMDB entry 5462, marked with an asterisk, were obtained from Sriram Subramaniam). When PDB coordinates were not available, gp120s were fit to density maps in the EMDB using UCSF Chimera. The mean and standard deviation for distances are listed for each category of trimer structure.

Chapter III

High resolution cryo-EM structures of sCD4, 17b, 8ANC195-bound Env show partially-open conformation, revealing CD4 induced coreceptor binding site exposure

Abstract

HIV-1 Env, a homotrimer of gp120-gp41 heterodimers, mediates membrane fusion after binding host receptor CD4 and coreceptor CCR5 or CXCR4. CD4 receptor binding displaces V1V2 loops from Env's apex, allowing coreceptor binding and opening Env to enable gp41-mediated fusion. We present 3.54 Å cryoelectron microscopy structures of a partially open soluble native-like Env trimers (BG505 SOSIP) bound to CD4. Comparing partially and fully open Envs with closed Envs shows that gp41 rearrangements are independent of the CD4-induced rearrangements that result in V1V2 displacement and formation of a 4-stranded bridging sheet. These findings suggest ordered conformational changes before coreceptor binding: (1) gp120 opening and gp41 conformational changes, including a compact gp41 central helix conformation, and (2) 4-stranded bridging-sheet formation and V1V2 displacement. These analyses illuminate potential receptor-induced Env changes and inform design of therapeutics disrupting viral entry.

Adapted from

Wang, Haoqing*, Christopher O. Barnes*, Zhi Yang, Michel C. Nussenzweig, and Pamela J. Bjorkman. "Partially Open HIV-1 Envelope Structures Exhibit Conformational Changes Relevant for Coreceptor Binding and Fusion." Cell host & microbe 24, no. 4 (2018): 579-592.

Introduction

The first step in HIV-1 infection is fusion of the viral and host cell membrane to allow the HIV-1 capsid to enter the target cell (Harrison, 2015). Fusion is accomplished by HIV-1 Envelope (Env), a trimeric glycoprotein containing three copies of the receptor-binding gp120 and three copies of the membrane-attached gp41 (West et al., 2014). Binding of gp120 to the host cell receptor CD4 induces conformational changes that expose the binding site for GPCR coreceptor, CCR5 or CXCR4, whose binding results in further changes culminating in insertion of the fusion peptide into the host cell membrane and fusion of the two bilayers (Pancera et al., 2017).

cryoET and subtomogram averaging of Env trimers on HIV virions surface revealed different conformations, including unliganded Env in a prefusion, closed state with interaction across the gp120 trimer apex, and CD4-bound, open Env that exhibitd outwardly displaced and rotated gp120 monomers (Liu et al., 2008). The low resolution of these structures precluded detailed interpretations of CD4 induced conformational changes, but higher resolution X-ray and single-particle cryoelectron microscopy (cryo-EM) structures of soluble native-like Env trimers (SOSIPs) (Sanders et al., 2013) in the closed, prefusion conformation were consistent with unliganded virion-bound cryoelectron tomography Env structures, and also revealed juxtaposition of the three gp120 V1V2 loop regions at the trimer apex that shield underlying regions of the coreceptor binding site on V3 (Ward and Wilson, 2017). In 2016, our group published an intermediate resolution (8.9 Å) single-particle cryo-EM structure of an SOSIP Env complexed with soluble CD4 (sCD4), coreceptor-mimicking antibody 17b (Sullivan et al., 1998), and gp120-gp41 spanning antibody 8ANC195 (Scheid et al., 2011). The structure was consistent with the electron tomography structures of CD4-bound Env on virions (Liu et al., 2008) and showed ~40 Å displacement of the V1V2 loops to the sides of the Env trimer to expose V3 (Wang et al., 2016a). These results were verified and extended in a 3.7 Å sCD4-and 17b-bound SOSIP structure, which also described side-chain rearrangements in gp120 and gp41 that were visible at higher resolution, but did not show ordered density for the rearranged V1V2 loops (Ozorowski et al., 2017).

We present two cryo-EM sCD4-bound SOSIP Env structures in complex with CD4-induced (CD4i) coreceptor-mimicking antibodies and with 8ANC195, a broadly neutralizing antibody (bNAb) that recognizes the gp120-gp41 interface (Scharf et al., 2014; Scharf et al., 2015; Scheid et al., 2011). The first structure, a complex of clade A/E BG505 SOSIP Env with sCD4 and Fabs 17b and 8ANC195, was solved to a resolution of 3.54 Å (BG505-sCD4-17b-8ANC195 complex), allowing a detailed description of partial closure of the open sCD4-bound Env state that results from 8ANC195 binding. The second structure, solved at 4.06 Å resolution, is a complex of the clade B B41 SOSIP Env (Pugach et al., 2015) with sCD4, the CD4i antibody 21c (Xiang et al., 2002), and 8ANC195 (B41-sCD4-21c-8ANC195 complex). Despite binding of the 8ANC195 Fab that partially closes the open, sCD4-bound Env conformation, the structures show rearrangements in gp120, including displacement of V1V2, exposure of V3, formation of the 4-stranded bridging sheet, and formation of the α0 helix. In addition, unlike the V1V2 regions in the BG505-sCD4-17b-8ANC195 and B41-sCD4-17b structures, the displaced V1V2 loops in the B41-sCD4-21c-8ANC195 structure exhibited ordered density, allowing the structure of the displaced V1V2 to be determined. Comparisons of the partially open Env structure with fully open structures, including an open B41 Env complexed with b12 antibody against CD4-binding site (Ozorowski et al., 2017), showed that Env opening results in shifting of the gp41 helices to match post-fusion gp41 structures (Chan et al., 1997; Weissenhorn et al., 1997), and that Env opening and structural changes in gp120, such as V1V2 displacement and bridging-sheet formation, are independent steps. These comparisons suggest that Env opening in the absence of V1V2 displacement, a state that may exist in equilibrium with closed Env, triggers gp41 rearrangements as an initial step in the conformational changes required for fusion. A second, CD4-dependent step, involves V1V2 displacement and formation of the gp120 bridging sheet and α0 helix. Analyses of these results further our understanding of HIV-1 Env conformational changes leading to fusion and provide templates for designing agents to disrupt HIV-1 entry into target cells.

Results

EM studies confirmed that recombinant native-like soluble gp140 Env trimers (SOSIPs) (Sanders et al., 2013) can adopt the closed and open architectures seen on virion-bound Env trimers (Harris et al., 2011; Sanders et al., 2013; Tran et al., 2012). Thus the SOSIP substitutions (SOS, a disulfide bond linking gp120 to gp41, and IP, an Ile to Pro mutation in gp41) do not prevent transition to the open Env state, although interpretations of sCD4-induced changes in gp41 must be interpreted cautiously since SOSIP Envs lack the membrane-proximal external regions, the transmembrane domains, and the cytoplasmic tails of gp41. For our cryo-EM structures, each sCD4-bound SOSIP Env was complexed with Fabs from a CD4i coreceptor-mimicking antibody (either 17b or 21c) (Sullivan et al., 1998; Xiang et al., 2002) and from 8ANC195, a gp120-gp41 interface bNAb (Scharf et al., 2014; Scharf et al., 2015; Scheid et al., 2011). CD4i Fabs were added to stabilize the coreceptor-binding site and prevent Env closure because three CD4i Fabs cannot be accommodated on closed Env trimers due to steric clashes (Scharf et al., 2015). 8ANC195 Fab was added to rigidify the gp120-gp41 interface and induce partial closure of fully-open, sCD4-bound Env (Scharf et al., 2015; Wang et al., 2016a), allowing investigation of the partially-open Env conformation.

Env-sCD4-Fab samples were prepared by adding 8ANC195 Fab to pre-formed open Env-sCD4-CD4i Fab complexes. Single-particle cryo-EM structures of BG505-sCD4-17b-8ANC195 and B41-sCD4-21c-8ANC195 complexes were solved to resolutions of 3.54 Å and 4.06 Å, respectively (Figure 3.1; Table 3.1, 3.2; Supplementary Figure 3.1-3.4) (Env sequence alignments and definitions of secondary structural elements are shown in Supplementary Figure 3.5). Each trimeric Env complex included three copies each of sCD4, CD4i Fab, and 8ANC195 Fab. The 17b and 21c Fabs exhibited distinct orientations relative to gp120s (Figure 3.1B,D), each consistent with crystal structures of these Fabs complexed with sCD4-bound gp120 cores (Diskin et al., 2010; Kwong et al., 1998). However, the BG505 and B41 Env trimers in our two structures were similar to each other (Supplementray Table 3.1), thus the binding of 17b versus 21c to the sCD4-bound

Envs did not influence the extent of Env opening or the overall conformation of the Env trimers. As described in the 8.9 Å Env-sCD4-17b-8ANC195 structure (Wang et al., 2016a), the V1V2 loops were displaced from their location at the trimer apex to the sides of the trimer in the new partially-open BG505 and B41 Env structures; however, portions of the displaced V1V2 were ordered in the B41-sCD4-21c-8ANC195 complex structure (Figure 3.1D). As seen in other sCD4-bound Env structures (Ozorowski et al., 2017; Wang et al., 2016a), the rearranged V3 loops were largely disordered in the two partially-open sCD4-bound Envs (Figure 3.1B,D and 3.2A).

To evaluate conformational changes resulting from sCD4 and 8ANC195 Fab binding, we compared the partially-open Env trimers to a 3.7 Å fully-open B41 SOSIP in a B41-sCD4-17b complex (PDB 5VN3) (Ozorowski et al., 2017) and closed SOSIP Env structures (e.g., PDB 5T3X) (Figure 3.2, Supplementary Table 3.3). We also included a 3.6 Å cryo-EM structure of B41 Env complexed with the CD4-binding site bNAb b12 (PDB 5VN8) in which the Env trimer exhibited an open conformation with respect to rotation and displacement of the gp120 subunits, but the V1V2 loops were not displaced to the sides of the Env trimer (Ozorowski et al., 2017).
We illustrated differences in gp120 positions in partially-open, open, and closed Env trimers by measuring distances between gp120 landmarks (the CD4bs, the base of V1V2, and the base of V3) (Supplementary Table 3.1) and highlighting their positions on Env structures (Figure 3.2A). To facilitate visualization of different gp120 orientations, we also highlighted the gp120 landmark residues on Env structures in which the coordinates for V1V2 and V3 residues were removed, demonstrating a progression of gp120 displacement relative to closed Env in partially-open versus open Env structures (Figure 3.2B). The sCD4-bound Envs showed outward displacements and rotations of gp120s compared with closed Env, with the partially-open sCD4-8ANC195-bound structures exhibiting smaller displacements from the closed Env conformation relative to the open, sCD4-bound Env conformation (Figure 3.2B, Supplementary Table 3.1). The b12-bound open Env trimer also showed outward displacement of gp120s similar to the open sCD4-bound Envs (Figure 3.2A,B), but unlike the partially-open and open sCD4-bound Envs in which the V1V2 loops were displaced to the side of Env trimer, the V1V2 loops remained “on top” of the displaced gp120s in b12-bound Env, where it was oriented equivalently with respect to the rest of gp120 as seen in closed Env structures (Figure 3.2D). Thus, opening of the b12-bound Env trimer involves a rigid

body movement of the gp120-V1V2 unit such that the coreceptor binding site on the V3 loop remains largely buried, whereas the opening of gp120 subunits in sCD4-bound Envs includes repositioning of V1V2 to expose the V3 loop (Figure 3.2D). This rigid body movement suggests that Env trimer opening and CD4-induced coreceptor binding site exposure represent two distinct steps.

To evaluate differences in Env trimer openness, we aligned a gp120 monomer of our partially-open BG505-sCD4-17b-8ANC195 structure with gp120 monomers from the partially-open B41-sCD4-21c-8ANC195 structure, closed Env, and the two forms of open Envs. The gp120 subunits of partially-open and fully-open sCD4-bound Envs aligned with low root mean square deviation (rmsd) values in all regions except for the N- and C-terminal strands (β4 and β26), where the rmsds increased to beyond 4 Å (Figure 3.3A). The β4 and β26 strands in the partially-open sCD4-bound Envs were most similar in orientation to closed Envs, with closer agreement to an 8ANC195-bound closed Env structure than a closed Env solved in the absence of 8ANC195 (Figure 3.3A). Taken together, these results suggest that the β4 and β26 strands serve as a pivot point about which the rest of the gp120 subunit moves as a rigid body to either open Env trimer upon sCD4 or b12 binding or to partially close the sCD4-bound Env trimer conformation upon binding to 8ANC195.
We next investigated whether gp41 moves along with the gp120 β4 and β26 strands by aligning gp140s that were superimposed on their gp120-gp41 interface residues (defined as the gp120 and gp41 residues that include atoms within 5 Å of each other) (Figure 3.3B; Supplementary Figure 6). With the exception of interface residues on HR1 and the fusion peptide, the gp120-gp41 interfaces (highlighted in green on Figures 3.3B and Supplementary Figure 6) were mostly unchanged for different degrees of openness (Figure 3.3B). Thus, interactions across the gp120-gp41 interface in SOSIP Envs remain relatively unchanged during trimer opening. If this result extends to full-length Env trimers that do not contain the stabilizing SOSIP mutations, it suggests rigid body displacement of gp120 β4, β26, and the core portion of gp41 except for HR1C.

Each gp41 protomer in Env trimer comprises an N-terminal fusion peptide sequence, followed by two helical regions, HR1 and HR2 (Supplementary Figure 5). The fusion peptides in the partially-

open SOSIP Env structures reside in a pocket at the gp120-gp41 interface as seen in the fully-open Env conformation (Supplementary Figure 7). Although the ordered residues of the fusion peptide in closed and fully-open Env structures form loops, the BG505-sCD4-17b-8ANC195 and B41-sCD4-21c-8ANC195 partially-open Env structures include ordered fusion peptide residues in an a-helical conformation (Supplementary Figure 4E,F; Supplementary Figure 7A). The finding of helical fusion peptide residues likely represents the beginning of the formation of an energetically stable fusion peptide conformation that inserts into the target cell membrane during the fusion process (Harrison, 2015). HR1C, the C-terminal portion of HR1, forms a parallel 3-helix bundle in Env trimers. The HR1C helical bundle in partially-open Env gp41 subunits is extended at its N-termini by ordered residues at the C-termini of HR1N (N-terminal portion of HR1) to form longer and continuous a-helices (Supplementary Figure 7A). We observed extended HR1C helices in fully-open SOSIP Env structures, including the b12-bound open Env, but not in closed Envs (Supplementary Figure 7A). In addition, the HR1C helical bundle is more compact in both partially-open and fully-open Envs than the 3-helical bundles in pre-fusion, closed Env structures (Supplementary Figure 7A). Since the compact HR1C conformation was also observed in the B41-b12 structure (Ozorowski et al., 2017) (Supplementary Figure 7A), these changes do not require V1V2 displacement. Notably, the compact HR1C conformation observed in all forms of open SOSIP Env matches the HR1C conformation seen in post-fusion gp41 structures in which HR1N forms a continuous a-helix with HR1C (Chan et al., 1997; Weissenhorn et al., 1997) (Supplementary Figure 7A,B). Taken together, these observations suggest that the change to a compact HR1C bundle that is extended at its N-terminus with HR1N helical residues represents one of the first intermediate conformations in open structures on the path to the fusion-active conformation (Supplementary Figure 7C). As these changes are also observed in the partially-open Env trimers, 8ANC195 binding and partial closure of the open Env conformation does not reverse HR1C and HR1N changes induced by trimer opening.

gp120 folding topologies are divided into two categories based on formation of the bridging sheet, an antiparallel b-sheet involving gp120 b-strands β2, β3, β20, and β21 (Figure 3.4). The bridging sheet was first observed in structures of gp120 cores (gp120 monomers with truncations in V1V2, V3, and the N- and C-termini) in the presence and absence of sCD4 (Kwon et al., 2012; Kwong et

al., 1998) (Figure 3.4A). However, the sheet is not fully formed in closed, prefusion Env trimers; instead of a 4-stranded anti-parallel β-sheet, the β3, β20, and β21 strands form a mixed parallel and anti-parallel 3-stranded sheet, and the β2 residues adopt an a-helical conformation (Ward and Wilson, 2017) (Figure 3.4B).

The 4-stranded bridging sheet is found in both partially-open sCD4-bound Env structures, with the rearranged V1V2 region located between b2 and b3 strands, similar to the fully-open Env in the B41-sCD4-17b structure (Ozorowski et al., 2017). By contrast, the open Env in the B41-b12 complex adopts the 3-stranded b-sheet conformation of closed Env trimers (Figure 3.4B). Thus, the formation of the 4-stranded bridging sheet correlates with, and is likely required for, V1V2 displacement and exposure of the coreceptor binding site on V3. Also, in common with the open form of B41 bound to sCD4 and 17b (Ozorowski et al., 2017), the partially-open BG505 and B41 Envs include the gp120 α0 helix, which interacts with the HR1 in the gp41 of an adjacent protomer, whereas the α0 region of the gp120s in the b12-bound open B41 Env and in closed Envs formed irregular loops (Figure 3.2C).

The B41-sCD4-17b structure revealed a series of gp120 side chain rearrangements relative to closed Env structures; these side chain rearrangements were not seen in the open B41-b12 complex (Ozorowski et al., 2017) (Figure 3.4A,B; Supplementary Figure 4A), suggesting they are related to 4-stranded bridging sheet formation induced by sCD4 binding rather than Env opening. A subset of the gp120 side chain rearrangements ($Tyr435_{gp120}$, $Trp427_{gp120}$, $Trp112_{gp120}$, $Leu111_{gp120}$, and $Trp69_{gp120}$) were observed in the 17b-bound partially-open structure and monomeric gp120 structures (Figure 3.4A, Supplementary Figure 4A), demonstrating that (*i*) gp120 side chain rearrangements occur both in BG505 and in B41 Envs upon binding to sCD4, (*ii*) 8ANC195 binding and partial Env closure does not reverse these rearrangements, and (*iii*) the rearrangements are related to 4-stranded bridging sheet formation. The fact that the side chain positions found in sCD4-bound Env trimers are also found in monomeric gp120 core structures, whether or not they are complexed with sCD4, indicates that this collection of side chain conformations is related to formation of the 4-stranded bridging sheet (Figure 3.4A).

Discussion

The HIV-1 Env glycoprotein must adopt multiple conformations to function in fusion of the viral and host cell membranes (Ward and Wilson, 2017). Although we cannot define mechanisms for structural transitions from static structures that, by necessity, contain bound ligands and antibodies, by comparing our cryo-EM structures of sCD4-bound partially-open SOSIP Env trimers with structures of Env in other conformational states, we reveal information about how Env trimers rearrange to expose the coreceptor binding site and describe which parts of the rearrangement are reversible upon binding to a gp120-gp41 interface bNAb (Figure 3.5A). In particular, we captured an ordered conformation of the displaced V1V2 loops that move from the trimer apex to the sides of open Env upon sCD4 binding. We also showed that the structural rearrangements of extending and compacting the gp41 central helices are an initial step to achieving an open Env conformation (Figure 3.5) in the SOSIP Env trimers under comparison.

With respect to the coreceptor binding site, the most relevant feature of the closed Env trimer structure is the location of the V1V2 loops at the trimer apex that shield the coreceptor binding site on V3 (Figure 3.5A; panel 1). The apex location of the V1V2 loops and their burial of V3 requires the 3-stranded form of the gp120 bridging sheet. The HR1C region of the three central gp41 helices are relatively separated from each other in the closed conformation, and the a0 region adjacent to HR1C adopts a loop conformation (Figure 3.5A; panel 1).

We hypothesize that a later, but still early, conformation on the pathway towards coreceptor binding site exposure is represented by the b12-bound open conformation of the B41 HIV-1 Env (Figure 3.5A; panel 2) (Ozorowski et al., 2017). In this structure, the gp120 subunits have rotated outwards from the trimer axis. However, although the Env trimer is open, the V1V2 loops are not displaced from their location at the top of each gp120 subunit, thus leaving the V3 loop partially buried by V1V2 (Figure 3.5A; panel 2). It is unclear if the b12 antibody captures a pre-existing open Env state that is in equilibrium with closed Env; if so, this state is not detectable in DEER spectroscopy analyses of SOSIP Env conformations (Stadtmueller et al., 2018). Thus, the b12-

bound open state could either be induced by b12 binding or exist at levels that are spectroscopically undetectable but that can nevertheless can be captured by b12. This state may represent an early intermediate after sCD4 binding to the closed, prefusion state, in which gp120 rotation is a prerequisite to V1V2 displacement (Figure 3.5A; panel 3).

The B41-b12 structure demonstrates that Env trimer can open even without forming the 4-stranded gp120 bridging sheet, likely based on gp41 rearrangements and rotation about the pivot point defined by the gp120 β4 and β26 strands. Moreover, gp120 opening in the absence of 4-stranded bridging sheet formation triggers some of the structural rearrangements seen in sCD4-bound structures; for example, some conserved gp120 side chains ($Trp69_{gp120}$, $His72_{gp120}$, $Leu111_{gp120}$) are rearranged with respect to the closed structure (Figure 3.5A, panels 1 and 2). Interestingly, the HR1C helices adopt the compact conformation found in post-fusion gp41 structures (Chan et al., 1997; Weissenhorn et al., 1997) and also include HR1N residues as part of a longer central gp41 helical region.

The final conformation of open Env on the pathway to coreceptor binding appears in the sCD4-bound Env structures in which the gp120 subunits have opened, as in the b12-bound conformation, but the V1V2 loops have also been displaced to the sides of Env trimer to expose the V3 loop for interactions with coreceptor (Figure 3.5A, panel 3). However, the V3 residues are largely disordered in this structure and in the partially-open Env structures with displaced V1V2 loops, suggesting that flexibility in V3 facilitates interactions with coreceptor. In coreceptor binding site-exposed open conformations, the gp120 bridging sheet adopts a 4-stranded conformation in which the b2 residues form a b-strand connected to the N-terminal strand A of V1V2. The b2 and b3 gp120 elements also swap positions so that the four strands of the bridging sheet are now antiparallel, allowing the displacement of V1V2 from the top of each gp120 to its side, thereby exposing V3. The HR1C helices in gp41 retain their compact configuration with extended helical regions from HR1N residues at their N-termini. Some conserved gp120 residues adopt altered side chain conformations that were proposed to allosterically transfer the signal from the sCD4 binding site to the gp120-gp41 interface, such the structure of gp41 is altered (Ozorowski et al., 2017). For

example, the gp120 a0 residues are now in a helical conformation that tops the HR1C from a neighboring gp41protomer.

The open, coreceptor-binding site exposed conformation goes on to bind CCR5 or CCR4, adopting uncharacterized fusion-active conformation(s) that promotes fusion of the viral and host cell membranes. The only available structures of a conformational state that follows the open, coreceptor binding site-exposed conformation, are structures of 6-helical bundles of HR1 and HR2 portions of gp41 (Chan et al., 1997; Weissenhorn et al., 1997) (Figure 3.5A, panel 5), which presumably represent post-fusion conformations of gp41. These structures contain the continuous HR1N-HR1C helix in a compact 3-helix bundle, which is similar to open, but not closed, Env trimer structures.

Having categorized features of available Env structures in terms of their relationship to each other and to the post-fusion gp41 conformation, our structures address the pliability of the sCD4-bound conformation by showing that the sCD4-bound open conformation can partially close through binding to 8ANC195 (Figure 3.5A), a gp120-gp41 interface bNAb that also binds closed Envs (Scharf et al., 2015). In our two Env-sCD4-8ANC195 structures, the gp120 subunits are not as separated from each other as in fully-open conformations, therefore we refer to this conformation as partially open (Figure 3.5A, panel 4). The complexes for these structure determinations were formed by incubating fully-open, sCD4-bound Env trimers with 8ANC195, suggesting that 8ANC195 either captured a partially-open, sCD4-bound conformation or its binding triggered partial closure of the open conformational state. Whether the partially-open sCD4-bound conformation of Env trimer represents a dead-end conformation of Env or a coreceptor binding site-exposed conformation of Env that could proceed along the pathway to viral/host cell membrane fusion is unknown. In any case, the structural comparisons show that partial closure of the sCD4-bound open state does not reverse the formation of 4-strand bridging sheet, V1V2 displacement, coreceptor binding site exposure, a0 helix conformation, or the formation of compact gp41 HR1C helices with HR1N extensions (Figure 3.5A, panel 4). However, not all of the gp120 side chain rearrangements are conserved with the fully-open sCD4-bound structure. Interestingly, an ordered portion of the gp41 fusion peptide, which adopts a loop conformation in

closed and other open Env structures, is a-helical in both partially-open Env structures. As the fusion peptide is thought to insert into the target membrane as a helix (Harrison, 2015), the partially-open structures show a propensity of the fusion peptide to shift from a loop into a helix in preparation for mediating fusion of the viral and host membranes.

Although disordered in other sCD4-bound complexes, the conformation of the displaced V1V2 region was revealed in the B41-sCD4-21c-8ANC195 complex. The secondary structural elements of V1V2 and regions of flexibility indicated by disorder are mostly maintained whether V1V2 is displaced to the sides of Env trimer, interacts about the apex of a closed Env trimer, or was expressed as a monomeric V1V2 scaffold. This suggests that, in the CD4-bound conformation, the V1V2 secondary structural elements move as a rigid body about the loops extending from strands A and D. Thus the B41-sCD4-21c-8ANC195 structure likely reveals their architecture because of the stabilizing effects of 21c via interactions with the B-C loop region, while in the 17b-bound open structures, the displaced V1V2 occupies multiple positions that are averaged out during map reconstruction.

Comparisons of available Env structures provide clues as to what controls displacement of V1V2 to expose the coreceptor binding site in sCD4-bound structures. We note that in all Env structures with a 4-stranded bridging sheet, including Env trimers in fully- and partially-open conformations as well as gp120 monomer structures plus and minus bound sCD4, the side chain conformations of conserved gp120 residues $Tyr435_{gp120}$, $Trp427_{gp120}$, $Trp112_{gp120}$, $Leu111_{gp120}$, and $Trp69_{gp120}$ are consistent. By contrast, in all structures with 3-stranded bridging sheets (closed Env trimers and b12-bound open Env), the conserved residues adopt distinct conformations. These results suggest that the side chain rearrangements in these residues control the reorganization of the β2, β3, β20, and β21 structural elements and thus regulate 4-stranded bridging sheet formation and coreceptor binding site exposure. Thus, structures of monomeric gp120 cores, which include a 4-stranded bridging sheet, mimic the sCD4-bound and coreceptor binding site-exposed conformation of gp120 in Env trimers, rather than the conformation in closed, pre-fusion Env trimers.

Many structural questions related to Env conformations remain to be elucidated, most notably the fusion-active conformation that results from coreceptor binding. However, the structures reported here provide critical information for understanding steps leading up to coreceptor binding site exposure including: (*i*) suggesting an order for Env conformational changes, (*ii*) describing elements of conformational plasticity in the sCD4-bound Env state, and (*iii*) revealing a structure for the V1V2 regions displaced by sCD4 binding. This information adds mechanistic details to Env-mediated membrane fusion and provides a more complete sCD4-bound structure that serves as a template for understanding non-neutralizing, and potentially neutralizing, antibody responses to open Env conformations.

Methods

Protein Expression and Purification

His_6-tagged Fabs from 17b, and the $8ANC195_{G52K5}$ variant of 8ANC195 were expressed by transient transfection in HEK293-6E cells (National Research Council of Canada) and purified from cell supernatants using Ni-NTA chromatography and size exclusion chromatography (SEC) as described (Scharf et al., 2015). The heavy and light chain genes encoding 21c IgG were isolated as described (West et al., 2010) from an Epstein Barr virus-transformed human B-cell line (Xiang et al., 2002) obtained from James Robinson (Tulane University), and 21c IgG was expressed by transient transfection in HEK 293-6E cells. 21c IgG was isolated from transfected cell supernatants by Protein A chromatography (GE Healthcare), and 21c Fab was obtained by digesting with immobilized papain (Pierce) at 10 mg ml^{-1} and purified by protein A (GE Healthcare) and SEC chromatography as described (Diskin et al., 2010). His_6-tagged sCD4 D1D2 (domains 1 and 2; residues 1–186 of mature CD4) was expressed by transient transfection in HEK293-6E cells and purified by Ni-NTA chromatography and SEC.

BG505 SOSIP.664 v3.2 (in vector pTT5, National Research Council of Canada), a native-like soluble gp140 trimer (Sanders et al., 2013) including the 'SOS' substitutions ($A501C_{gp120}$, $T605C_{gp41}$), the 'IP' substitution ($I559P_{gp41}$), the *N*-linked glycan sequence at residue 332_{gp120} ($T332N_{gp120}$), an enhanced gp120-gp41 cleavage site (REKR to RRRRRR), and a stop codon after residue 664_{gp41} (Env numbering according to HX nomenclature) was expressed in HEK293-6E cells in the absence of kifunensine and was purified from cell supernatants by 2G12 immunoaffinity chromatography and SEC as previously described (Wang et al., 2017). B41 SOSIP.664 v4.2 (Pugach et al., 2015) was expressed in CHO Flp-In™ cells (Invitrogen) using vector pIPP4 (Chung et al., 2014) using cell lines kindly provided by Al Cupo and John Moore (Weill Cornell Medical College) and purified as described for BG505. All proteins were stored at 4˚C in 20 mM Tris, pH 8.0, and 150 mM sodium chloride (TBS buffer) supplemented with 0.02% (w/v) sodium azide.

Sample preparation

BG505-sCD4-17b-8ANC195 and B41-sCD4-21c-8ANC195 complexes were prepared by incubating purified Env with sCD4 at a 1:3 molar ratio (gp140 protomer:sCD4) for 4 h at room temperature, followed by subsequent incubation with a 1:3 molar ratio of CD4i Fab (gp140 protomer:17b or 21c) overnight at 4°C. Complexes were isolated by SEC in TBS (20 mM Tris pH 8.0, 100mM NaCl) using a Superose 6 10/300 column (GE Healthcare) and peak fractions analyzed by SDS-PAGE. Fractions corresponding to the Env-sCD4-CD4i complex were pooled and a 10-fold molar excess of 8ANC195 Fab was added before incubation at room temperature for 2 h. Complexes were again isolated by SEC using a Superose 6 10/300 column (GE Healthcare),analyzed by SDS-PAGE, and pooled. Purified BG505-sCD4-17b-8ANC195 and B41-sCD4-21c-8ANC195 complexes were diluted to 200 μg/mL and 350 μg/mL in TBS, respectively, and vitrified in liquid ethane using a Mark IV Vitrobot (FEI). Sample grids were prepared by adding 3 μL of complex to glow discharged 400 Mesh Quantifoil R1.2/1.3 copper grids.

BG505-sCD4-17b-8ANC195 complex cryo-EM data collection and processing

Images were recorded using SerialEM (Mastronarde, 2005) on a Titan Krios electron microscope equipped with Gatan K2 Summit direct detector. Exposures (15 s) were divided into 50 subframes with a dose rate of 3 electrons·pixel^{-1}·subframe^{-1}. After binning by two, each image was 4k×4k and 1.31 Å per pixel. A total of 3454 movies were collected using a 1-2.5 μm defocus range. The micrographs were motion corrected using MotionCor2 (Zheng et al., 2017) (Supplementary Figure 3.1A) and contrast transfer function (CTF) estimations were calculated using CTFFIND4 (Rohou and Grigorieff, 2015) (Supplementary Figure 3.1B). 2215 micrographs with CTF fitting beyond 4 Å were selected for automated particle picking using EMAN 2.2 (Ludtke et al., 2017). Subsequent steps were performed using RELION2 (Kimanius et al., 2016). A total of 548,229 particles were picked and sorted using initial 2D classifications. 213,791 particles from good 2D classes were selected for another round of 2D classification, which generated 195,755 “good” particles (Supplementary Figure 3.1C). For 3D classification, an intermediate resolution cryo-EM structure of the BG505-sCD4-17b-8ANC195 complex (EMDB 8407) (Wang et al., 2016a) was low-pass filtered to 60 Å to serve as the reference, and then 195,755 particles were classified into 10

different 3D classes assuming only C1 symmetry (Supplementary Figure 3.1C). Using 143,099 particles from six 3D classes as input for 3D refinement with C3 symmetry resulted in the highest resolution (4.68 Å) (Supplementary Figure 3.1C). These particles were movie refined and polished before the final 3D refinement step, during which the Fab C_HC_L and sCD4 D2 domains were masked out. After post-processing, the final resolution estimated by the gold-standard FSC (Scheres and Chen, 2012) was 3.54 Å (Supplementary Figure 3.1C, 3.3A)

B41-sCD4-21c-8ANC195 complex cryo-EM data collection and processing

Images were recorded using SerialEM (Mastronarde, 2005) on a Titan Krios electron microscope equipped with Gatan K2 Summit direct detector. Exposures (10 s) were divided into 50 subframes with a dose rate of 2 electrons·pixel^{-1}·subframe^{-1}. After binning by two, each image was 4k×4k and 1.31 Å per pixel. A total of 2531 movies were collected using a 1.7-3.5 μm defocus range. Subsequent steps were performed in RELION2 (Kimanius et al., 2016). The micrographs were motion corrected using MotionCor2 (Zheng et al., 2017) (Supplementary Figure 3.2A) and CTF estimations were calculated using CTFFIND4 (Rohou and Grigorieff, 2015) (Supplementary Figure 3.2B). Single particles were manually selected in Relion (~1000 particles) and used to create an initial particle stack that was 2D classified to generate a template for autopicking in Relion. Reference free, 2D classification of 474645 auto-picked particles was performed, and 346264 particles corresponding to class averages of the complex were selected (Supplementary Figure 3.2C). For 3D classification, a model structure of the Env-sCD4-21c-8ANC195 complex was generated by replacing 17b Fab with 21c Fab in the partially-open BG505-sCD4-17b-8ANC195 structure (PDB 5THR) (Wang et al., 2016a). The 21c Fab binding angle was determined by aligning gp120s from the gp120-sCD4-21c crystal structure (PDB 3LQA)(Diskin et al., 2010) and the BG505-sCD4-17b-8ANC195 structure. The modeled structure was low-pass filtered to 60 Å to serve as the initial 3D reference, and then 346264 particles were classified into 4 different 3D classes, during which C3 symmetry was assumed and the Fab C_HC_L domains were masked out (Supplementary Figure 3.2C). Using 305049 particles from three 3D classes as input for 3D refinement with C3 symmetry resulted in the highest resolution (4.39 Å) (Supplementary Figure 3.2C). These particles were movie refined and polished before the final 3D refinement step. After post-processing, the final resolution estimated by the gold-standard FSC (Scheres and Chen, 2012)

was 4.06 Å (Supplementary Figure 3.3A). Regions distal to the gp120-gp41 core, including 21c, sCD4, and the displaced V1V2, were further classified and refined in Relion to enable de novo model building (See Supplementary Figure 3.2C, 3.3 for details).

Cryo-EM model building

Coordinates for individual components of the 3.54 Å BG505-sCD4-17b-8ANC195 cryo-EM structure were docked into their corresponding density regions using UCSF Chimera (Pettersen et al., 2004). The following coordinate files were used for docking: gp120 from a B41-sCD4-17b complex structure in an open conformation (PDB 5VN3), gp41 from the same structure, sCD4 D1 domain (PDB 2NXY), 17b Fab (PDB 2NXY) (Zhou et al., 2007), 8ANC195 Fab (PDB 4P9M) (Scharf et al., 2014). The docked coordinates were used as the template for RosettaCM (Song et al., 2013) to build an initial model of BG505 Env, after which the model were manually modified in Coot (Emsley and Cowtan, 2004) to remove residues that did not fit into density or clashed with other components. Coordinates for BG505 plus sCD4 and the Fabs were refined by applying C3 symmetry using Rosetta (Tange, 2011; Wang et al., 2016b). Coordinates for ordered N-linked glycans from PDB 5T3X and PDB 5VN3 Env structures (Gristick et al., 2016; Ozorowski et al., 2017) were fit separately as rigid bodies at potential N-linked glycosylation sites (PNGSs) at which EM density was apparent (Supplementary Figure 3.4B), and glycan rings outside of EM density were removed. The entire complex was refined using phenix.real_space_refine with secondary structure restraints for protein and geometric restraints for protein and N-glycan residues (Adams et al., 2010; Afonine et al., 2018; Agirre et al., 2015; Gristick et al., 2017) (Table 3.1).

An initial model was generated for the 4.06 Å B41-sCD4-21c-8ANC195 cryo-EM map by docking coordinates of individual components into their corresponding density regions with UCSF Chimera (Pettersen et al., 2004). Coordinates for gp120-gp41, sCD4 D1 domain, 21c Fab, and 8ANC195 Fab were obtained from PDB codes 5VN3, 2NXY, 3LMJ, and 4P9M, respectively. Docked coordinates were initially rigid-body refined in Coot (Emsley and Cowtan, 2004), followed by several cycles of refinement in Phenix (Adams et al., 2010; Afonine et al., 2018) and manual rebuilding in Coot. Coordinates for ordered N-linked glycans from PDB 5T3X and PDB 5VN3 Env structures (Gristick et al., 2016; Ozorowski et al., 2017) were fit separately as rigid bodies at

potential N-linked glycosylation sites (PNGSs) where EM densities for N-glycans were apparent (Supplementary Figure 3.4B), and subsequently trimmed and refined in Coot to fit the cryo-EM map.

Density corresponding to the previously-uncharacterized V1V2 residues 129-195 was interpreted in the B41-sCD4-21c-8ANC195 structure as follows. After focus classification and refinement on the 21c, sCD4, V1V2 region (Supplementary Figure 3.2C, Supplementary Figure 3.3), we identified density characteristic of a 2-stranded anti-parallel b-sheet that resembled the strand B–connecting loop–strand C conformation in known V1V2 structures (Supplementary Figure 3.4G). An initial polyalanine model for strand B-connecting loop-strand C residues 154-174 was generated using coordinates from a closed BG505 crystal structure (PDB 5T3Z) and manually docked into density (Supplementary Figure 3.4G). The remaining portions of V1V2 could be placed by first building residues to continue the b2 strand into strand A and residues preceding b3 as strand D. We next found density compatible with a b-strand that could form a b-sheet interaction with strand D and assigned that as the V2 strand. Remaining density appearing to connect strands A and B via a long loop were left unmodeled due to uncertainty of the sequence register. b-strand restraints were applied to strands A-D and V2 throughout refinement in both Coot and Phenix. The entire complex was refined using phenix.real_space_refine with secondary structure restraints for protein and geometric restraints for protein and N-glycan residues (Adams et al., 2010; Afonine et al., 2018; Agirre et al., 2015; Gristick et al., 2017) (Table 3.2).

Figures

Figure 3.1

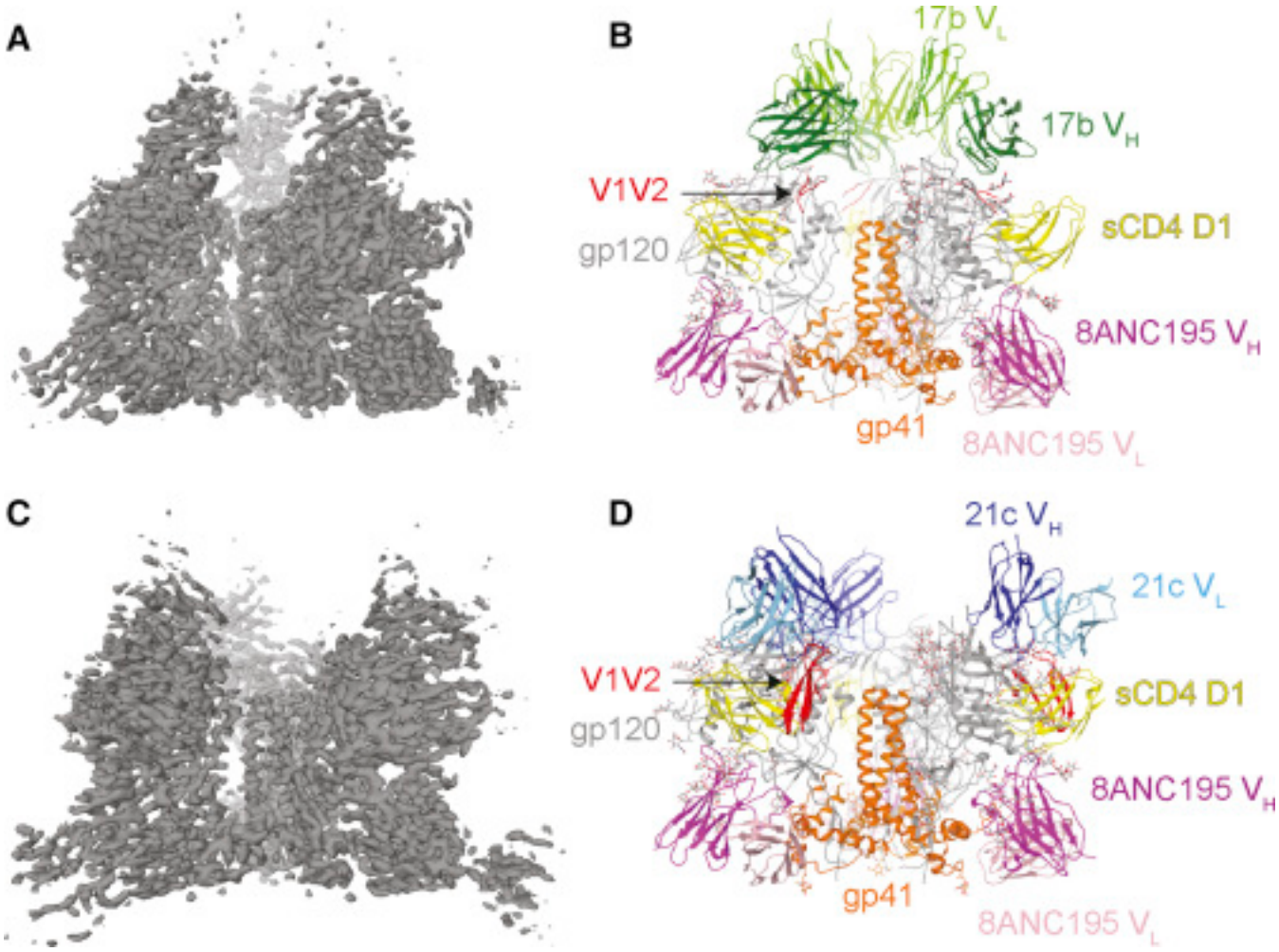

Figure 3.1. Cryo-EM Structures of sCD4-Bound Env Trimers.

(A) 3.54 Å density map of BG505-sCD4-17b-8ANC195 complex.

(B) Fitted coordinates of BG505-sCD4-17b-8ANC195 complex.

(C) 4.06 Å density map of B41-sCD4-21c-8ANC195 complex.

(D) Fitted coordinates of B41-sCD4-21c-8ANC195 complex. The CH and CL domains of the Fabs and D2 domain of sCD4 were disordered in both structures and not fit into density.

Figure 3.2

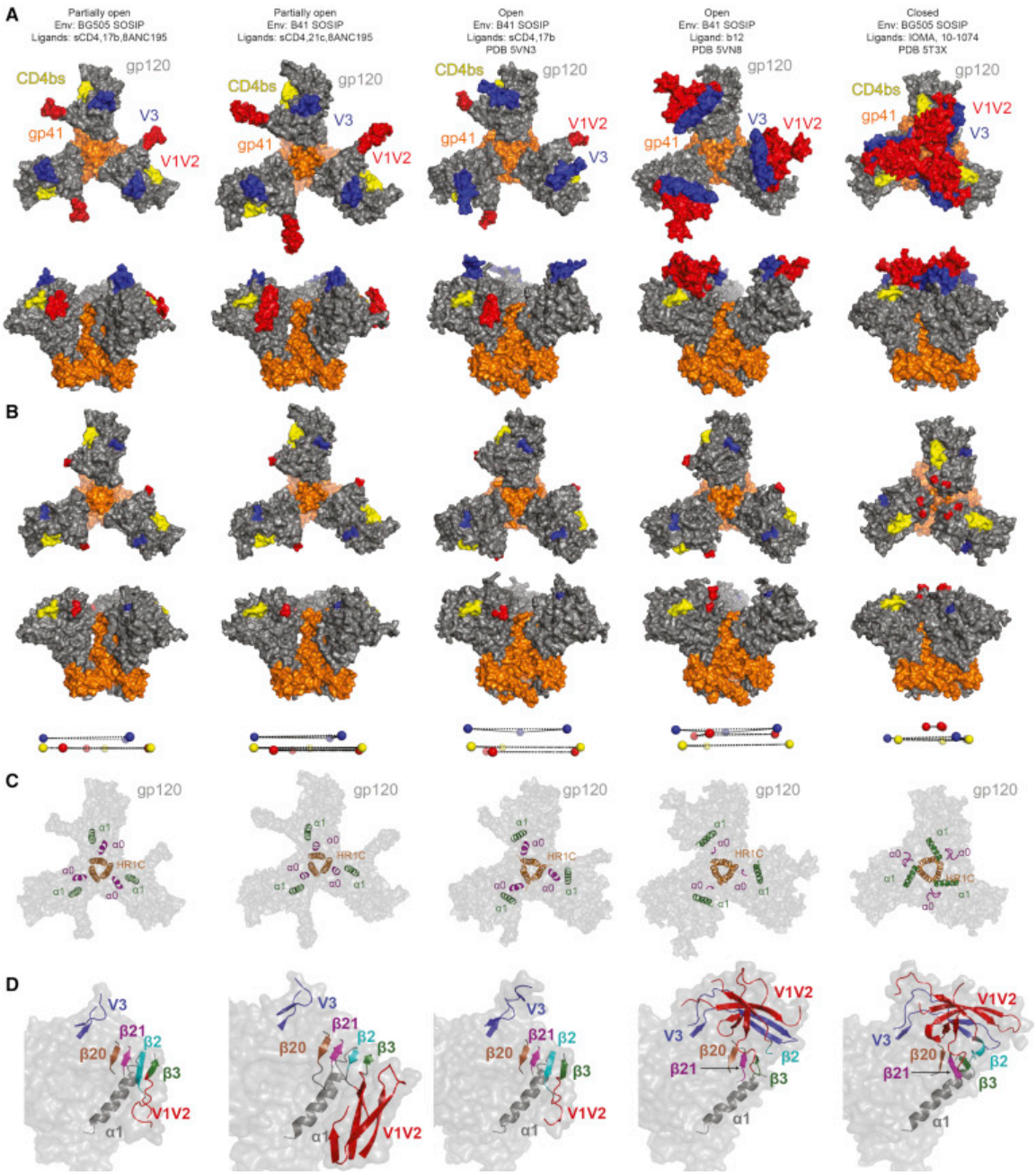

Figure 3.2. Comparison of Env Conformations

(A) Top and side views of surface representations of Env trimers in partially open, sCD4-bound open, b12-bound open, and closed conformations. PDB: 5T3X is shown as a representative

example of a closed Env structure; inter-protomer distances on closed Env structures are similar to each other despite strain-specific sequence differences and binding of different Fab ligands (Stadtmueller et al., 2018).

(B) Structures shown in (A) with coordinates for residues 126–198 in V1V2 and 296–330 in V3 removed to facilitate seeing positions of landmark residues: CD4bs residues 364–372 (yellow), residue 125 and 199 at the base of V1V2 (red), and residues 295 and 331 at the base of V3 (blue). Positions of CD4bs residue 368, V1V2 base residue 124, and V3 base residue 330 are shown as spheres below their respective Env structures.

(C) Conformational changes of α0. Structures in (A) and (B) are shown with coordinates for residues 64–73 in α0 and 98–117 in α1 in cartoon depiction overlaid on a transparent trimer surface.

(D) gp120 monomers from structures shown in (A) and (B). β2, β3, β20, β21, V1V2 residues 126–198, and V3 residues 296–330 are shown in cartoon representations overlaid on a transparent gp120 surface.

Figure 3.3

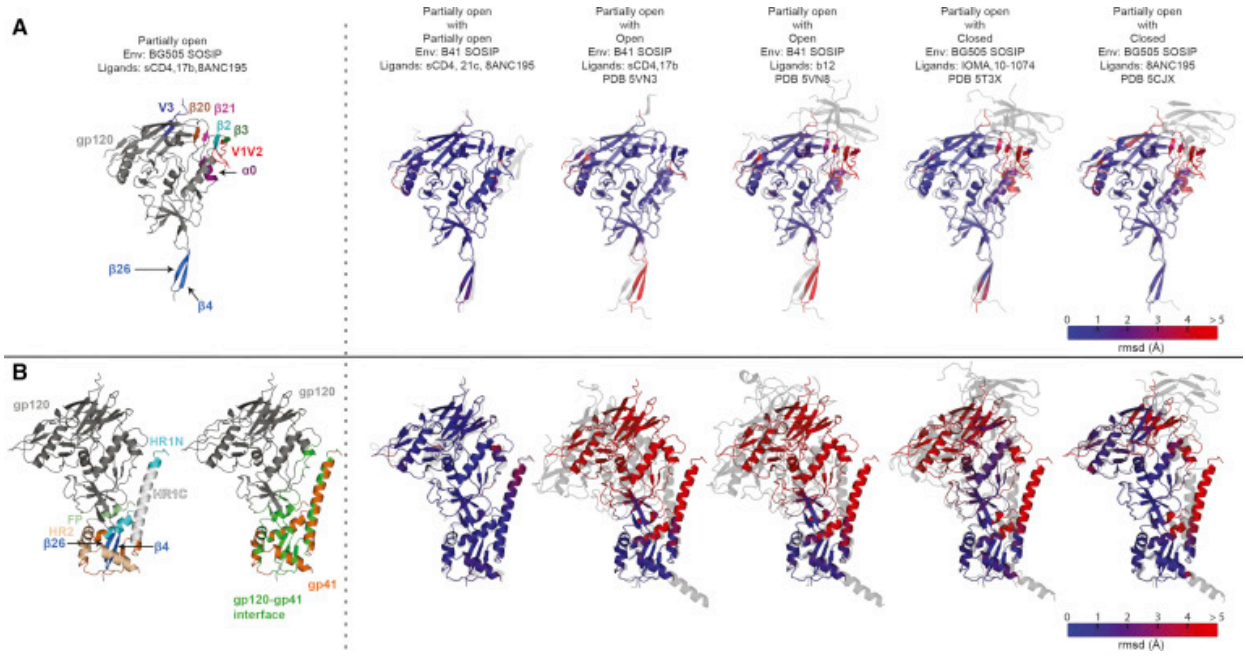

Figure 3.3. Conformations of the gp140 Protomer

(A) Superimpositions of gp120 monomer from the BG505-sCD4-17b-8ANC195 Env trimer structure with gp120s from other Env trimer structures. Left: gp120 monomer from the BG505-sCD4-17b-8ANC195 structure with highlighted structural elements of interest. Right: gp120 from the BG505-sCD4-17b-8ANC195 structure (blue-red colors indicating RMSDs) superimposed with the indicated gp120s (gray).

(B) Superimpositions of gp140 protomer from the BG505-sCD4-17b-8ANC195 Env trimer structure with gp140s from other Env trimer structures. Left: gp140 protomers from the BG505-sCD4-17b-8ANC195 structure with highlighted structural elements of interest (first structure) and highlighted gp120-gp41 interface regions (second structure). Right: gp140 from the BG505-sCD4-17b-8ANC195 structure (blue-red colors indicating RMSDs) superimposed with the indicated gp120s (gray).

Figure 3.4

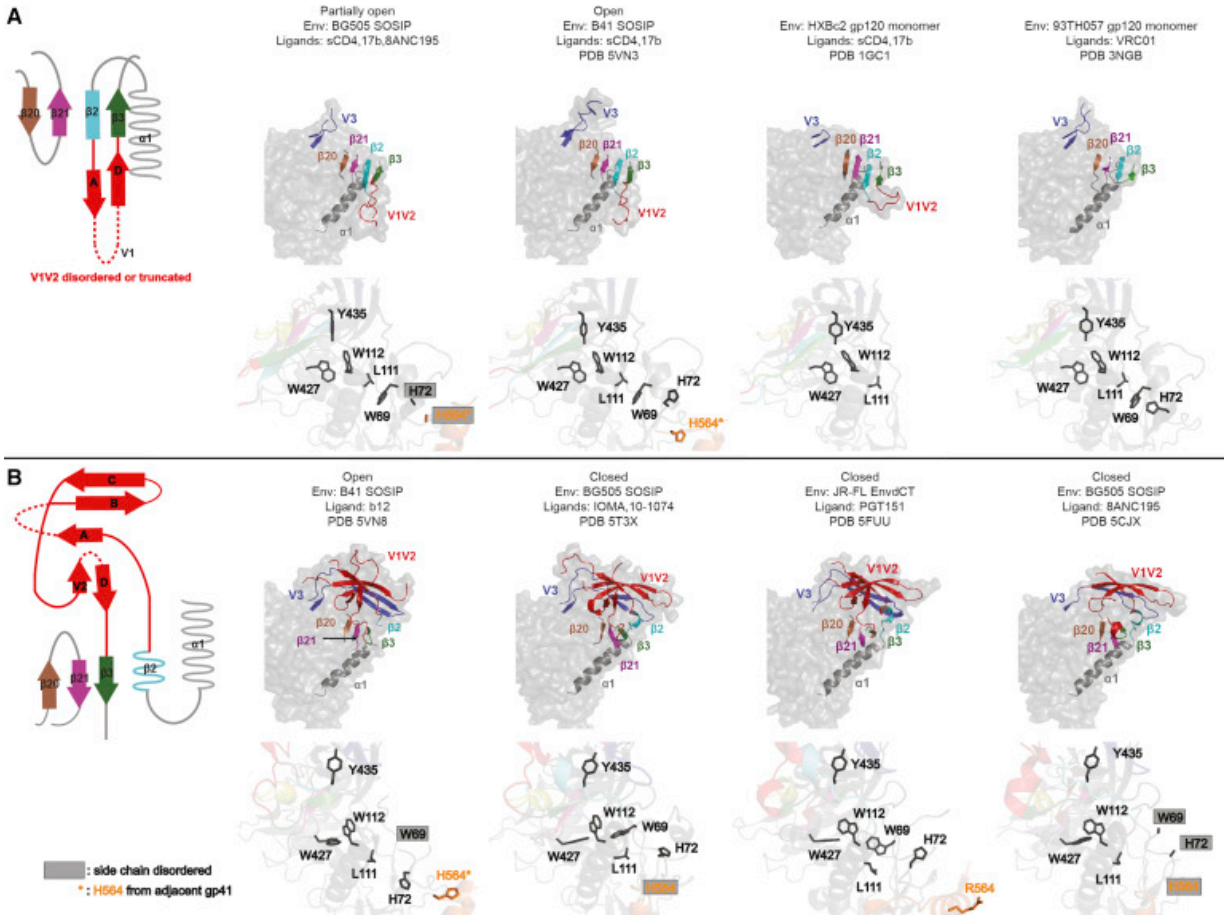

Figure 3.4. Network of Conserved Residues Regulating gp120 Conformational Changes

(A) Bridging-sheet and conserved side-chain conformations in open Env trimer and gp120 monomer structures. Left: topology diagram of 4-stranded bridging sheet. Right: cartoon representations of β20, β21, β2, β3, α1, V1V2, and V3 overlaid on a transparent gp120 monomer surface (top) and stick representations of side chains of conserved residues of corresponding structures (bottom).

(B) Bridging-sheet and conserved side-chain conformations in b12-bound open Env and closed Env trimer structures. Left: topology diagram of 3-stranded bridging sheet. Right: cartoon representations of β20, β21, β2, β3, α1, V1V2, and V3 overlaid on a transparent gp120 monomer

surface (top) and stick representations of side chains of conserved residues of corresponding structures (bottom).

Figure 3.5

A

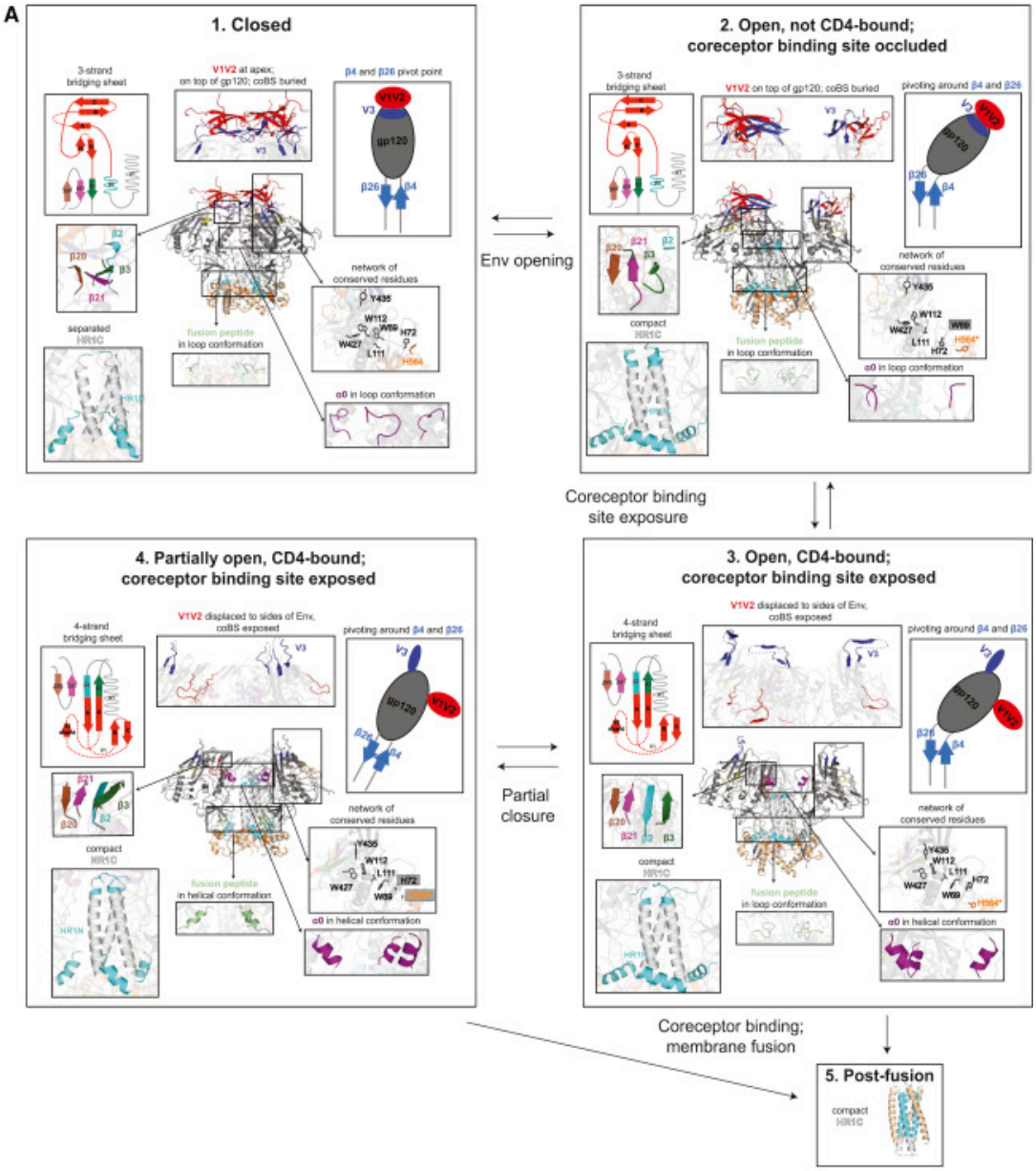

B

	gp120 conformation	V1V2	β2, β3, β20, β21	HR1C	α0	FP
closed	closed	at apex	3-strand	separated	loop	loop
open; coBS occluded	open	top of gp120	3-strand	compact	loop	loop
open; coBS exposed	open	displaced	4-strand	compact	helix	loop
partially open; coBS exposed	partially open	displaced	4-strand	compact	helix	helix
post-fusion	unknown	unknown	unknown	compact	unknown	helix

Figure 3.5. Model for Order of Conformational Changes Leading to Coreceptor Binding and Fusion

(A) Overview of features in different HIV-1 Env trimer conformational states. Five conformations that have been characterized by X-ray crystallography or cryo-EM are listed with their corresponding structural features. (1) PDB: 5T3Z; (2) PDB: 5VN8; (3) PDB: 5VN3; (4) this study; (5) PDB: 1AIK.

(B) Table summarizing structural features of the conformational states listed in (A). coBS, coreceptor binding site; FP, fusion peptide.

Tables

Table 3.1

Data collection/processing	
Microscope	Titan Krios
Voltage	300kV
Camera	Gatan K2 Summit
Camera mode	Super-resolution
Defocus range	1.0-2.5
Exposure time	15
Dosage rate	1.75 electrons/Å^2/subframe
Magnified pixel size	1.31 Å
Total dose	87.5 electrons/Å^2
Reconstruction	
Software	Relion-2.0
Symmetry	C3
Particles refined	143k
Final Resolution(Å)	3.54
Map sharpening B-factor (Å^2)	-95.4595
Model Statistics	
Mask CC	0.7744
Volume CC	0.759
Peak CC	0.602
All-atom clashscore	5.41
Ramachandran plot:	
outliers	0.00%
allowed	6.78%
favored	93.22%
Rotamer outliers	0.11%
C-beta deviations	0.00%
RMSD (bonds) (Å)	0.00
RMSD (angles) (°)	0.87
EMRinger Score	2.32

Table 3.1. Data collection and model statistics for the BG505-sCD4-17b-8ANC195 complex structure, related to Figure 3.1.

Table 3.2

Data collection/processing	
Microscope	Titan Krios
Voltage	300kV
Camera	Gatan K2 Summit
Camera mode	Super-resolution
Defocus range	1.7-3.5
Exposure time	10
Dosage rate	1.16 electrons/Å^2/subframe
Magnified pixel size	1.31 Å
Total dose	58.28 electrons/Å^2
Reconstruction	
Software	Relion-2.1
Symmetry	C3
Particles refined	215k
Final Resolution(Å)	4.24
Map sharpening B-factor (Å^2)	-220.00
Model Statistics	
Mask CC	0.808
Volume CC	0.805
Peak CC	0.550
All-atom clashscore	8.68
Ramachandran plot:	
outliers	0.19%
allowed	11.60%
favored	88.21%
Rotamer outliers	0.34%
C-beta deviations	0.00%
RMSD (bonds) (Å)	0.01
RMSD (angles) (°)	1.12
EMRinger Score	1.06

Table 3.2. Data collection and model statistics for the B41-sCD4-21c-8ANC195 complex structure, related to Figure 3.1.

Supplementary Figures

Supplementary Figure 3.1

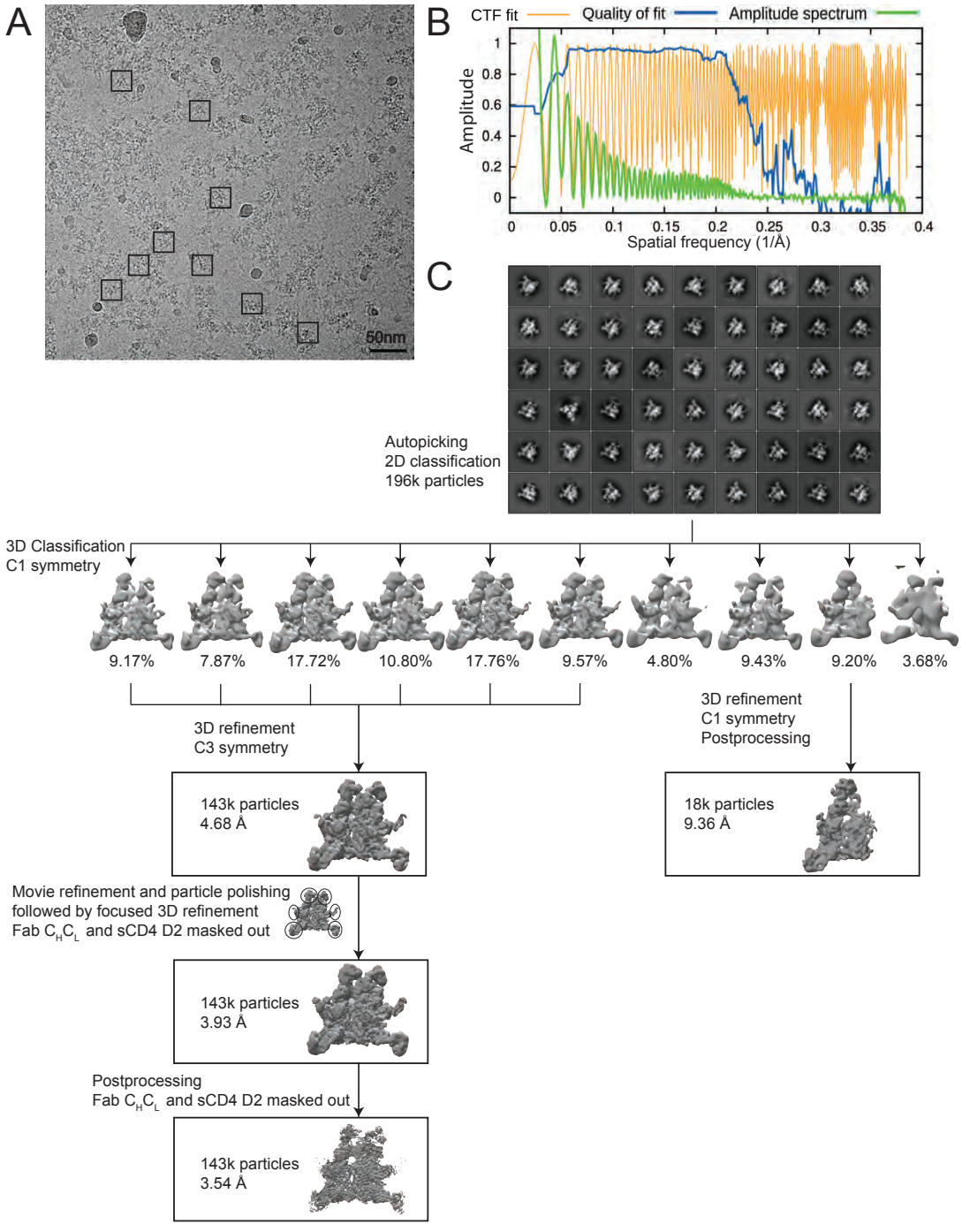

Supplementary Figure 3.1. Data processing for the BG505-sCD4-17b-8ANC195 complex structure, related to Figure 3.1.

(**A**) Representative motion corrected and dose-weighted micrograph of BG505-sCD4-17b-8ANC195 complex (examples of individual particles in boxes). Scale bar of 50nm is shown. The defocus value was ~2.3 μm underfocus. (**B**) CTF fitting of the micrograph shown in (A) using CTFFIND4 (Rohou and Grigorieff, 2015), showing a good fit to 3.3 Å. (**C**) Data processing scheme. 2D classification of autopicked particles resulted in 196k "good" particles that were 3D classified using a 60 Å low-pass-filtered cryo-EM structure (EMDB 8407) as the reference model. The 143k particles from the best six 3D classes were refined to 4.68 Å resolution using C3 symmetry. The particles in the 4.68 Å reconstruction were further movie refined and polished using RELION (Scheres, 2012), and then refined with the Fab C_HC_L domains and sCD4 D2 domains masked out. The final post-processing step generated a 3.54 Å structure with three bound sCD4 plus three 17b and three 8ANC195 Fabs per Env trimer. One 3D class with 18k particles with two sCD4, two 17b, and two 8ANC195 bound to each Env trimer was refined with C1 symmetry, resulting in a 9.36 Å structure.

Supplementary Figure 3.2

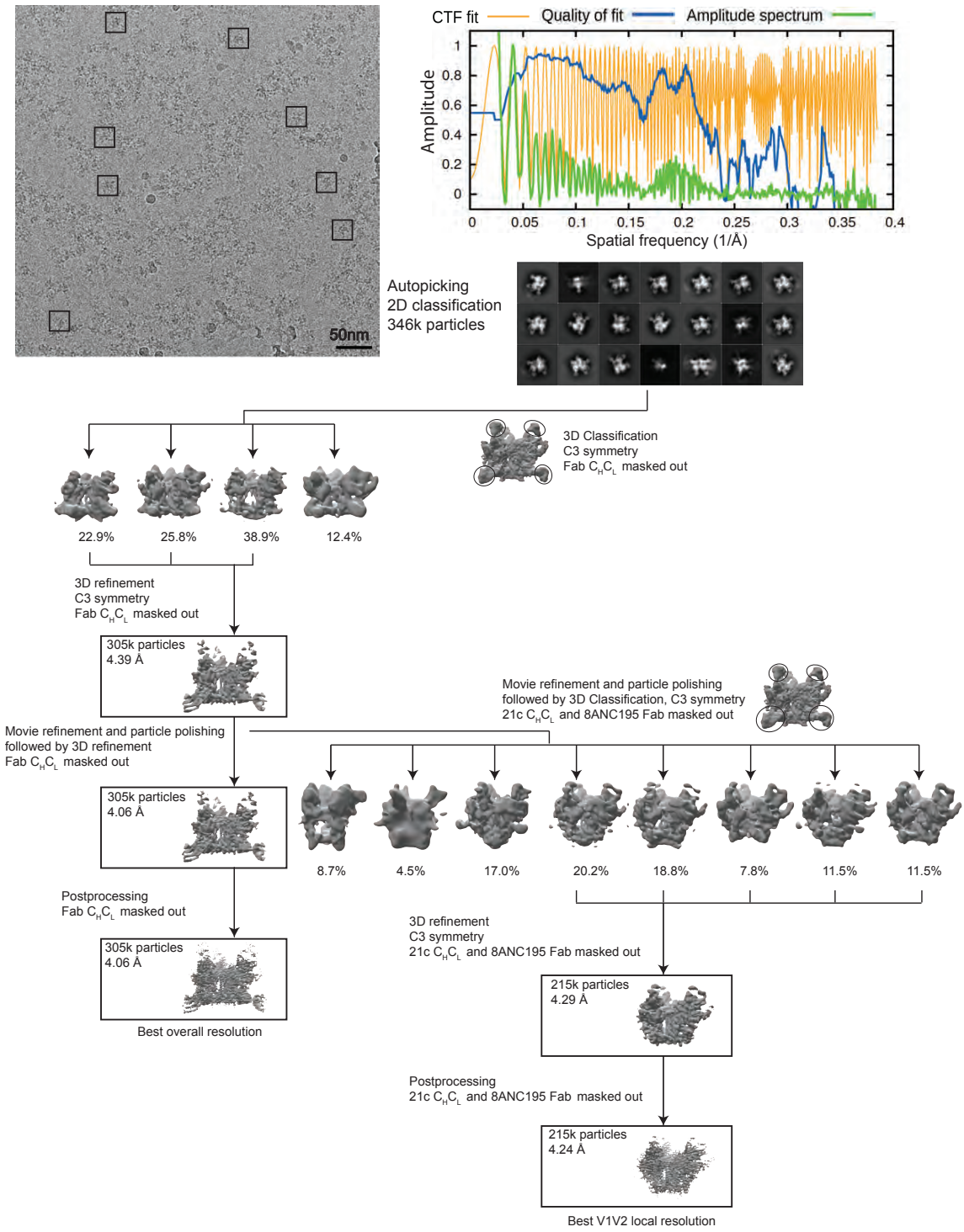

Supplementary Figure 3.2. Data processing for the B41-sCD4-21c-8ANC195 complex structure, related to Figure 1.

(**A**) Representative micrograph with examples of B41-sCD4-21c-8ANC195 complex in boxes. The defocus value was ~2.6 μm underfocus. (**B**) CTF fitting of the left micrograph using CTFFIND4 (Rohou and Grigorieff, 2015) showing a good fit to 4.7 Å. (**C**) Data processing scheme. 2D classification of autopicked particles resulted in 346k "good" particles that were 3D classified into four 3D classes using a 60 Å low-pass-filtered reference model assuming C3 symmetry. The reference model was made by replacing 17b Fab with 21c Fab in partially-open BG505-sCD4-17b-8ANC195 structure (PDB 5THR). The 21c Fab binding angle was modeled using a gp120-sCD4-21c crystal structure (PDB 3LQA). During 3D classification and the following refinement steps the Fab C_HC_L domains were masked out. The 305k particles from the best three 3D classes were refined to 4.39 Å resolution. The particles in the 4.39 Å reconstruction were further movie refined and polished using RELION (Scheres, 2012), and then refined to 4.06 Å. The final post-processing step generated a 4.06 Å structure with three bound sCD4 plus three 21c and three 8ANC195 Fabs per Env trimer. After movie refinement and particle polishing we performed another round of 3D classification, during which the 21c C_HC_L domains and the 8ANC195 Fabs were masked out, which improved the local resolution in the vicinity of V1V2. 305k particles were classified into 10 different classes assuming C3 symmetry, and 5 classes with obvious V1V2 densities were selected for model building of the displaced V1V2. After post-processing, the final resolution was 4.24 Å.

Supplementary Figure 3.3.

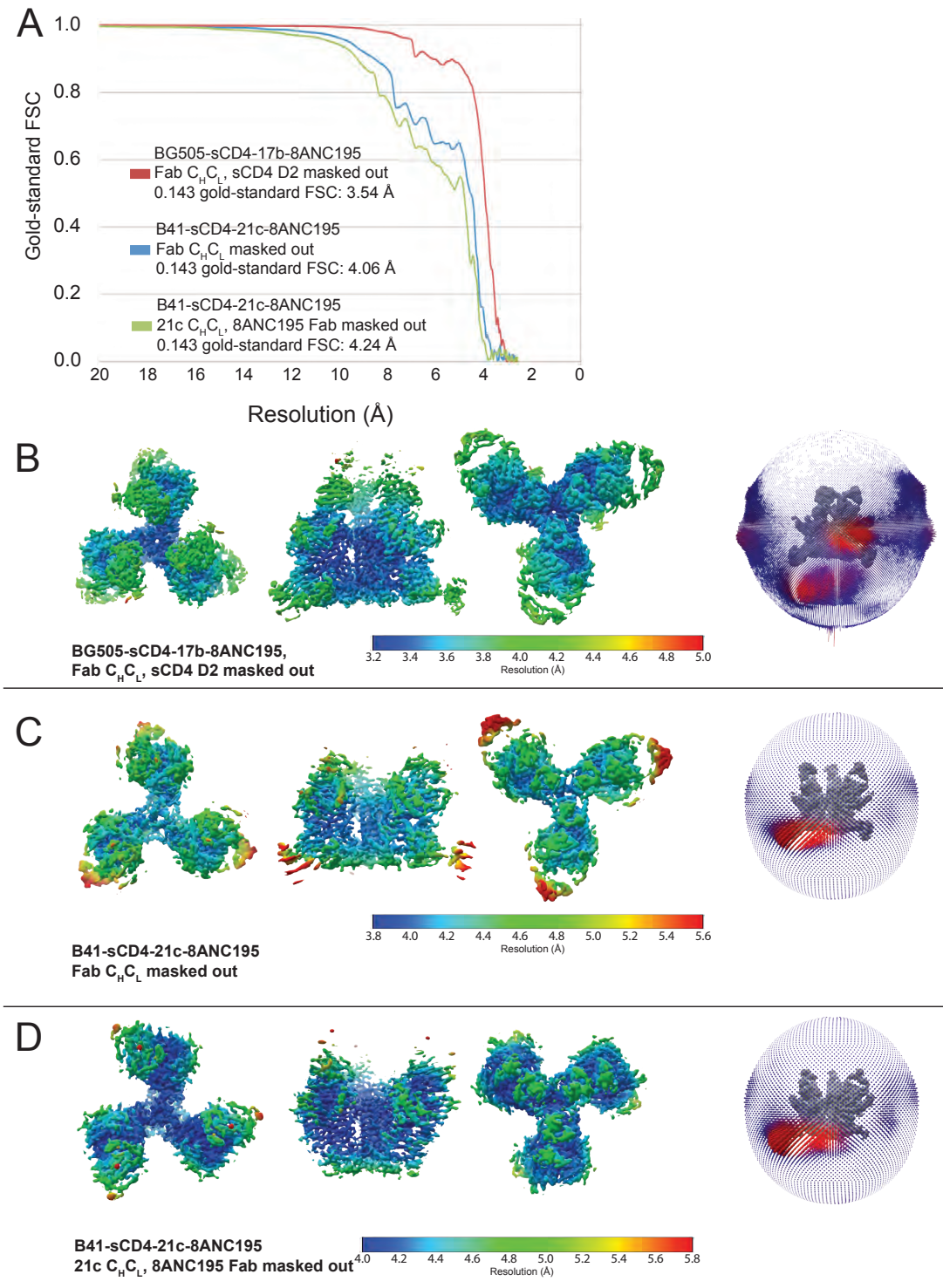

Supplementary Figure 3.3. Validation of the BG505-sCD4-17b-8ANC195 and B41-sCD4-21c-8ANC195 complex structures, related to Figure 3.1.

(**A**) Gold-standard FSC of 3.54 Å BG505-sCD4-17b-8ANC195 structure, 4.06 Å B41-sCD4-21c-8ANC195 structure, and 4.24 Å B41-sCD4-21c structure in which 8ANC195 Fabs were masked out. (**B**) Local resolution estimation and orientation distribution for the 3.54 Å BG505-sCD4-17b-8ANC195 structure. (**C**) Local resolution estimation and orientation distribution for the 4.06 Å B41-sCD4-21c-8ANC195 structure. (**D**) Local resolution estimation and orientation distribution for the 4.24 Å B41-sCD4-21c structure.

Supplementary Figure 3.4

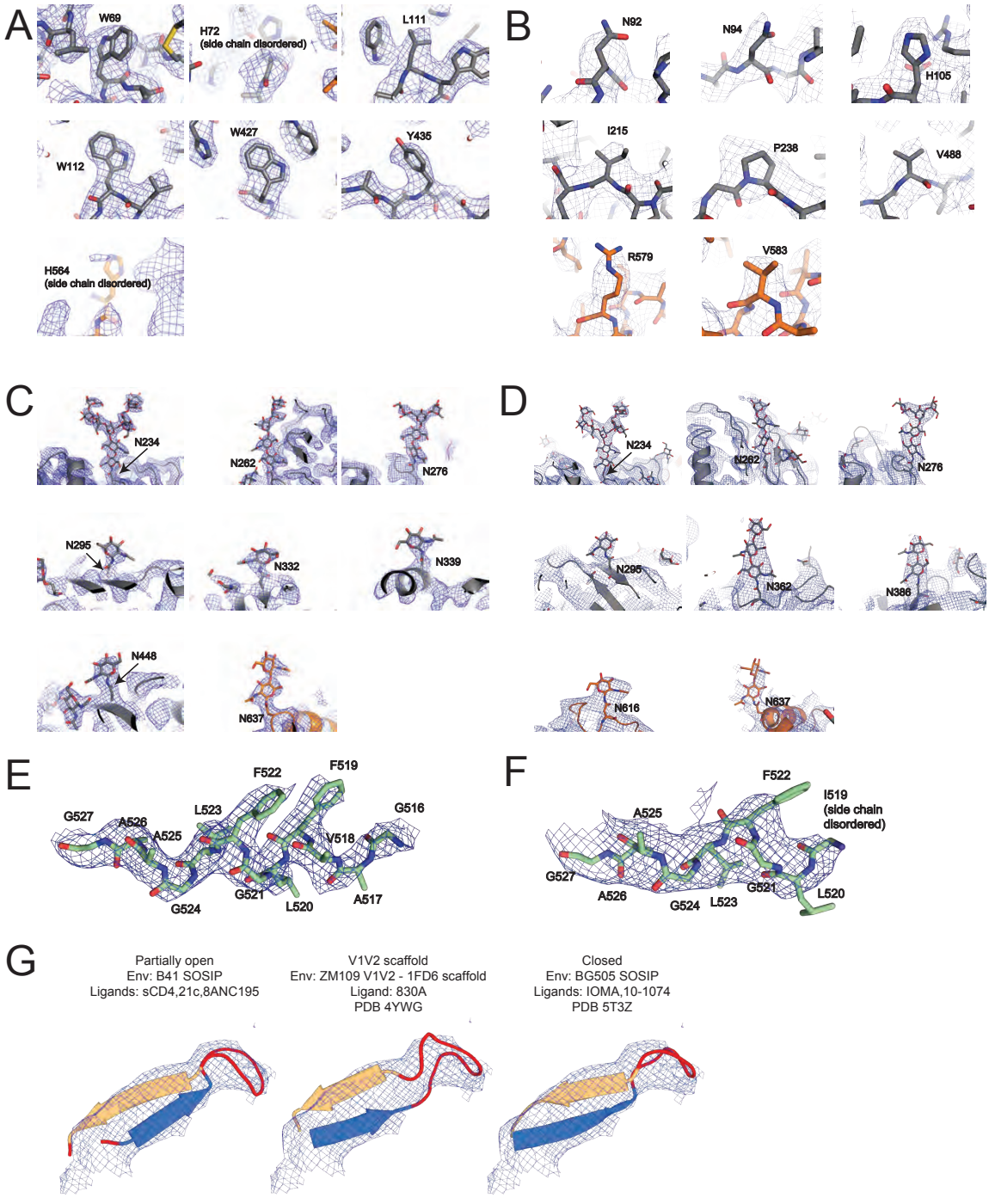

Supplementary Figure 3.4. Close-up views of cryo-EM maps, related to Figures 3.1 and 3.4.

Close-up views of selected density regions in the 3.54 Å BG505-sCD4-17b-8ANC195 and 4.24 Å B41-sCD4-21c-8ANC195 structures. Maps were contoured at 10.5 σ (0.0571 e/Å^3) for the BG505-sCD4-17b-8ANC195 structure (**A, C, E**) and 9.0 σ (0.0305 e/Å^3) for the B41-sCD4-21c-8ANC195 structure (**B, D, F, G**). (**A**) Cryo-EM densities of conserved residues shown in **Figure 4A** in the partially-open BG505-sCD4-17b-8ANC195 structure. (**B**) Cryo-EM densities of residues in the partially-open B41-sCD4-21c-8ANC195 structure. (**C, D**) Cryo-EM densities of N-linked glycans attached to the indicated Asn residues for BG505-sCD4-17b-8ANC195 (**C**) and B41-sCD4-21c-8ANC195 (**D**) structures. (**E, F**) Cryo-EM densities of fusion peptide regions in BG505-sCD4-17b-8ANC195 (**E**) and B41-sCD4-21c-8ANC195 (**F**) structures. (**G**) Cryo-EM density of the strand B–connecting loop–strand C region of the displaced V1V2 in the B41-sCD4-21c-8ANC195 structure. The density is shown as fit by strand B–connecting loop–strand C coordinates from the B41-sCD4-21c-8ANC195 structure (left), from a V1V2 scaffold structure (middle), and from a closed Env structure (right), demonstrating a consistent strand B–connecting loop–strand C geometry among different structures.

Supplementary Figure 3.5

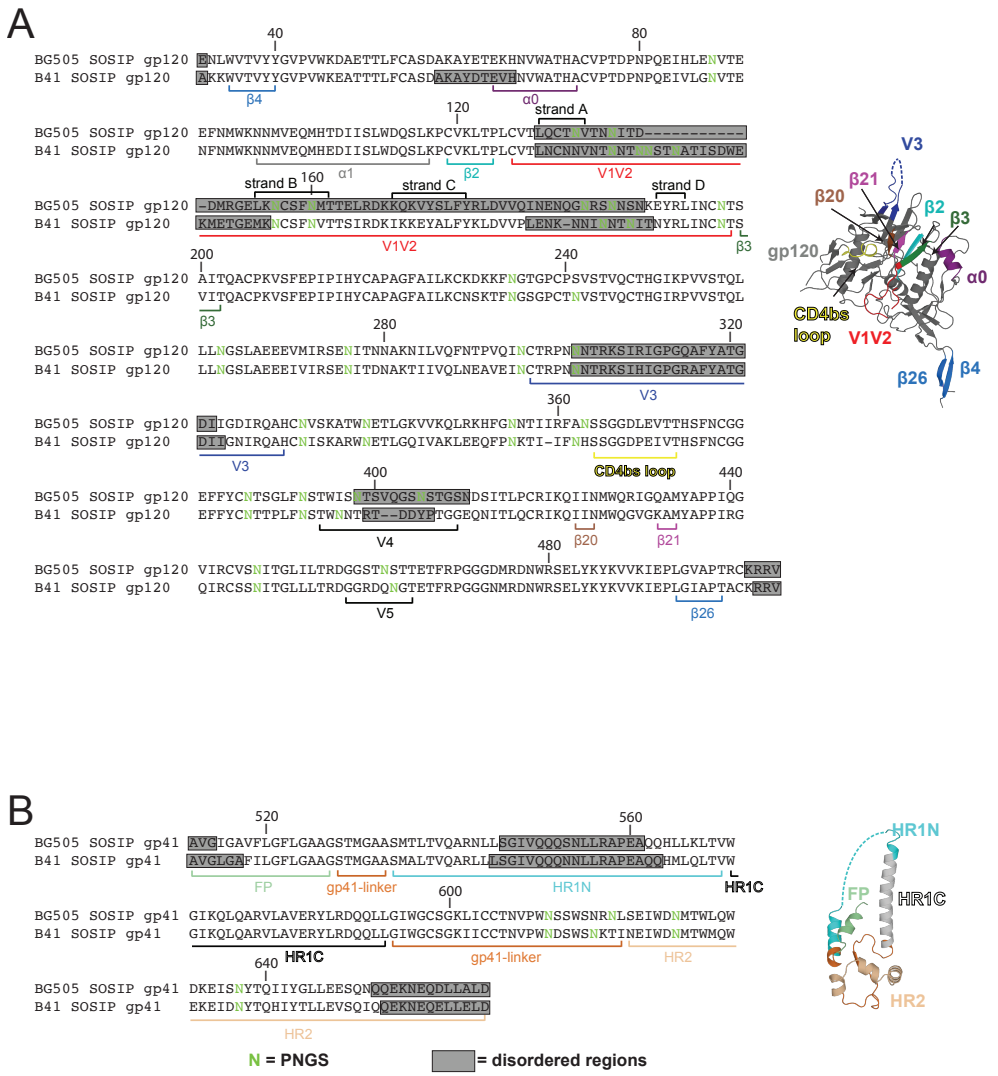

Supplementary Figure 3.5. Env sequence alignments and definitions of secondary structural elements, related to Figure 3.1, 3.2, and 3.3.

(A) Left: gp120 sequence alignment of BG505 SOSIP and B41 SOSIP. Potential N-linked glycosylation sites (PNGSs) are highlighted in green. Disordered regions in the BG505-sCD4-17b-8ANC195 and B41-sCD4-21c-8ANC195 structures are indicated by a grey background. Secondary structure elements are highlighted below the sequence alignments. Right: gp120 structure from the 3.54 Å BG505-sCD4-17b-8ANC195 complex structure. Secondary structure

elements are highlighted in the same colors as in the sequence alignment. (**B**) gp41 sequence alignment and structure as in (**A**).

Supplementary Figure 3.6

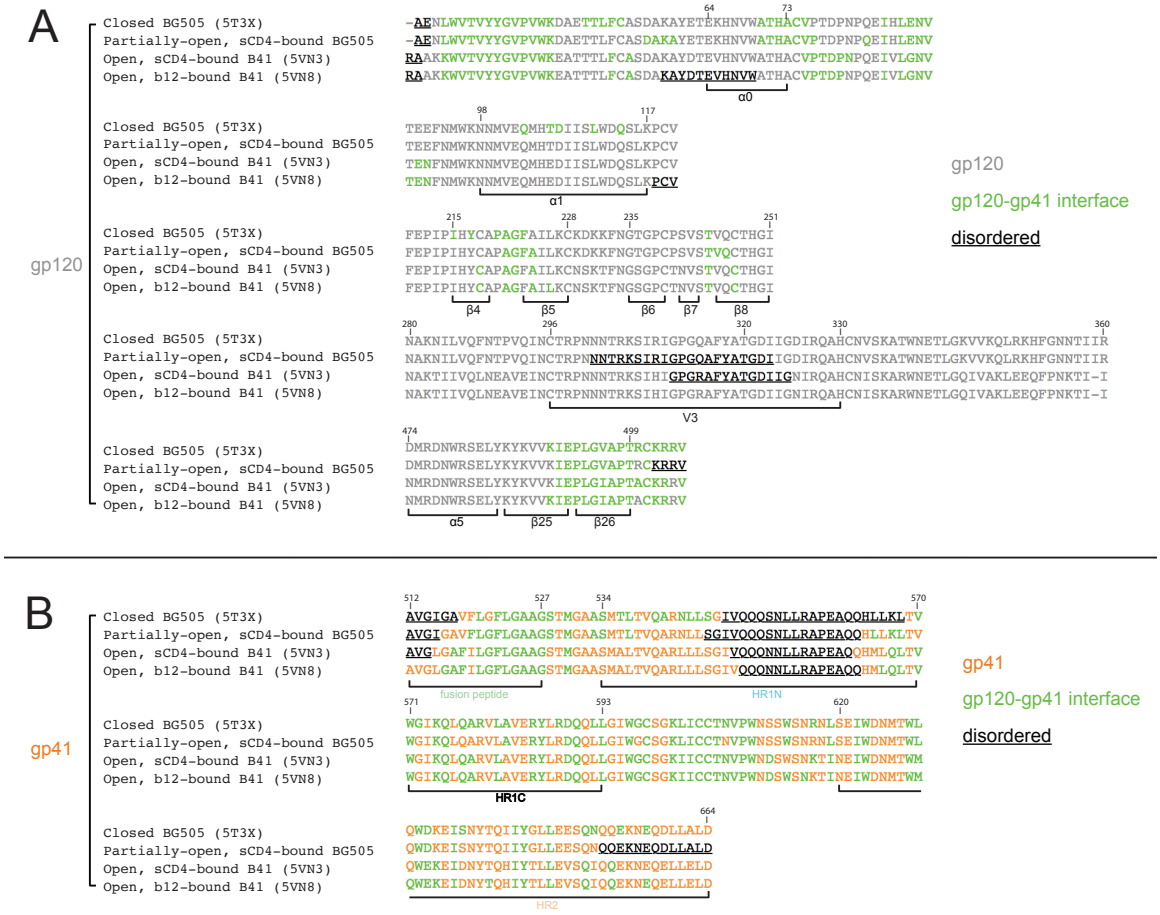

Supplementary Figure 3.6. gp120-gp41 interface residues, related to Figure 3.3.

(**A**) gp120 sequence alignment for partially-open BG505-sCD4-17b-8ANC195 structure (this study), open Envs (PDBs 5VN3 and 5VN8), and closed Envs (PDB 5T3X). Disordered regions are indicated by an underscore. gp120-gp41 interface residues (defined as the gp120 and gp41 residues that include atoms within 5 Å of each other) are highlighted in green. Secondary structure elements are labeled below the sequence alignment. (B) gp41 sequence alignment as in (**A**).

Supplementary Figure 3.7

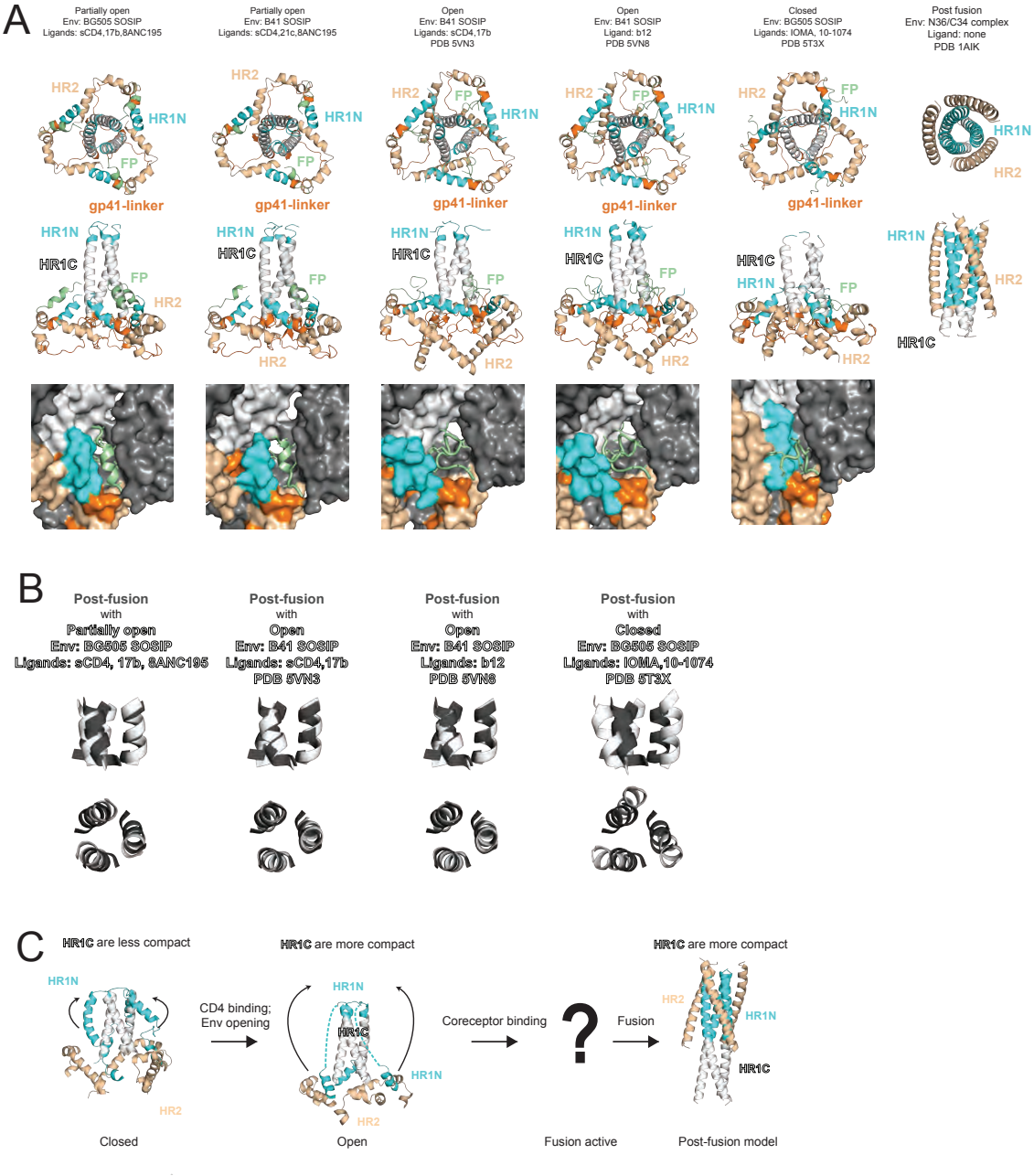

Supplementary Figure 3.7. gp41 structures in different conformations, related to Figure 3.3. **(A)** Trimeric gp41 structures from partially-open Envs **(**BG505-sCD4-17b-8ANC195 and B41-sCD4-21c-8ANC195**)**, open Envs (PDBs 5VN3 and 5VN8), closed Envs (PDB 5T3X), and a post-fusion gp41 core structure (PDB 1AIK). Upper panel: top views of gp41; middle panel: side views gp41; bottom panel: zoom-in view of fusion peptide residues (cartoon

representation) overlaid on surface representations of Env trimer structures. **(B)** Superimpositions of post-fusion gp41 HR1 structure with gp41 HR1 structures from Env in different conformations. Post-fusion gp41 HR1s are shown in black while gp41 HR1s from Env shown in white. (C) Proposed model of gp41 conformational changes during viral infection.

Supplementary Table

Trimer state	Ligand	Trimer type	EMDB /PBD ID	Resolution (Å)	Distance between V1V2 base (P124) (Å)	DIstance between CD4bs (D368) (Å)	Distance between V3 base (H330) (Å)
closed	8ANC195	BG505 SOSIP.664	5CJX	3.58	14	54	68
closed	PGT122, 35O22	BG505 SOSIP.664	4TVP	3.5	15	55	69
closed	PGT122	BG505 SOSIP.664	4NCO	4.7	14	56	70
closed	3H+109L, 35O22	BG505 SOSIP.664	5CEZ	3	14	56	69
closed	IOMA, 35O22	BG505 SOSIP.664	5T3Z	3.5	14	54	69
closed	PGT151	JR-FL EnvDCT	5FUU	4.19	16	56	69
					15±1	55±1	69±1
partially open	sCD4, 17b, 8ANC195	BG505 SOSIP.664	5THR	8.9	68	78	73
partially open	sCD4, 17b, 8ANC195	BG505 SOSIP.664	6CM3	3.54	67	79	76
partially open	sCD4, 21c, 8ANC195	B41 SOSIP.664	6EDU	4.06	69	79	73
					68±1	79±1	74±2
open	sCD4, 17b	B41 SOSIP.664	5VN3	3.7	79	84	73
open	b12	B41 SOSIP.664	5VN8	3.6	69	84	75

Supplementary Table 3.1. Distances between key residues in different Env trimer conformations, related to Figure 3.2. Inter-subunit distances were measured for indicated Cα atom positions in PyMol.

C h a p t e r I V

Asymmetric recognition of HIV-1 Envelope trimer by V1V2 loop-targeting antibodies

Abstract

HIV-1 surface glycoprotein Env trimer binds to host cell receptors to mediate membrane fusion. The prefusion Env trimer is stabilized by V1V2 loops that interact at the trimer apex. Broadly neutralizing antibodies (bNAbs) against V1V2 loops, exemplified by PG9, bind asymmetrically as a single Fab to the apex of the symmetric Env trimer using a protruding CDRH3 to penetrate the Env glycan shield. Here we characterized a distinct mode of V1V2 epitope recognition by the new bNAb BG1 in which two Fabs bind asymmetrically per Env trimer using a compact CDRH3. Comparisons between cryo-EM structures of Env trimer complexed with BG1 (6.2Å resolution) and PG9 (11.5Å resolution) revealed a new V1V2-targeting strategy by BG1. Analyses of the EM structures provided information relevant to vaccine design including molecular details for different modes of asymmetric recognition of Env trimer and a binding model for BG1 recognition of V1V2 involving glycan flexibility.

Adapted from

Wang, Haoqing, Harry B. Gristick, Louise Scharf, Anthony P. West Jr, Rachel P. Galimidi, Michael S. Seaman, Natalia T. Freund, Michel C. Nussenzweig, and Pamela J. Bjorkman. "Asymmetric recognition of HIV-1 Envelope trimer by V1V2 loop-targeting antibodies." Elife 6 (2017): e27389.

Introduction

The HIV-1 envelope (Env) glycoprotein trimer, a trimer of gp120-gp41 heterodimers, is the infectious machinery that targets host cell receptors CD4 and corecptors CCR5/CXCR4 to mediate fusion between the viral and host membranes (Wyatt and Sodroski, 1998). As the only viral protein on the surface of HIV-1 virions, Env trimer is the sole target of neutralizing antibodies that prevent viral infection (McCoy and Burton, 2017).

Although an infected host produces antibodies against HIV-1 Env, most are non-neutralizing or exhibit strain-specific neutralization that is ineffective in the face of HIV's ability to create resistant variants through rapid mutation (McCoy and Burton, 2017). Only a subset of HIV-1–infected individuals produce potent and broadly neutralizing antibodies (bNAbs) (Klein et al., 2013b; Landais et al., 2016), which can protect against and suppress infection in animal models (Barouch et al., 2013; Klein et al., 2012b; Shingai et al., 2013) and exhibit antiviral activity in human clinical trials (Caskey et al., 2015; Caskey et al., 2017; Lynch et al., 2015). HIV-1 bNAbs differ from most other antibodies in several ways. First, unlike most humoral immune responses, bNAbs usually take 1-3 years to develop (Klein et al., 2013b; Landais et al., 2016). Second, nearly all HIV-1 bNAbs exhibit high levels of somatic mutation, and many of these antibodies include long heavy chain complementarity determining region 3 (CDRH3) loops (West et al., 2014). These unusual features appear to be a significant barrier to eliciting such antibodies by immunization.

HIV-1 bNAbs have been mapped to distinct epitopes on HIV-1 Env including the variable 1 and 2 (V1V2) and variable 3 (V3) loops, the CD4 binding site (CD4bs) on gp120, the gp120-gp41 interface, and regions of gp41 including the membrane-proximal external region and fusion peptide (Burton and Mascola, 2015; Landais et al., 2016; McCoy and Burton, 2017; West et al., 2014). The V1V2 epitope is of interest because this region of gp120 undergoes large structural changes after binding to the primary receptor CD4: the interaction between CD4 and the gp120 portion of Env trimer stabilizes an open Env conformation that can interact with a chemokine receptor to induce

further conformational changes resulting in insertion of the fusion peptide on gp41 into the target cell membrane (Wyatt and Sodroski, 1998). Structures of soluble native-like Env trimers in the closed, prefusion state (Garces et al., 2015; Gristick et al., 2016; Julien et al., 2013a; Kong et al., 2015; Kwon et al., 2015; Lyumkis et al., 2013; Pancera et al., 2014; Scharf et al., 2015; Stewart-Jones et al., 2016; Ward and Wilson, 2017) showed that the V1V2 regions from the three gp120s interact around the trimer axis of symmetry to form a top layer of the trimer that shields V3 and the coreceptor binding site. In the CD4-bound state, the gp120 protomers are separated from each other (Liu et al., 2008; Tran et al., 2012), and the V1V2 loops are displaced by ~40 Å from the trimer apex to interact with CD4 on the sides of the trimer (Wang et al., 2016a).

Structural studies of V1V2 bNAbs include crystal structures of bNAb Fabs bound to monomeric V1V2 scaffolds (Gorman et al., 2016; McLellan et al., 2011; Pan et al., 2015; Pancera et al., 2013) and a low resolution single-particle EM structure of the V1V2 bNAb PG9 bound to a soluble, native-like Env trimer (Julien et al., 2013b). Crystal structures of monomeric V1V2 scaffolds bound to PG9 or to its PG16 relative revealed the V1V2 loop structure as a Greek key motif containing four b-strands that was recognized by the V1V2 bNAbs largely through interactions in which a long CDRH3 from the Fab reached through the Env glycan shield to contact a protein epitope in the V2 loop (McLellan et al., 2011; Pancera et al., 2013). The EM structure and complementary biophysical studies indicated that, unlike bNAbs in other epitope classes that bind symmetrically to Env trimers with three Fabs per trimer, only one PG9 bound per Env trimer, resulting in an asymmetric quaternary epitope at the Env apex (Julien et al., 2013b). Recent cryo-EM structures of Env trimer complexes with the V1V2 bNAb PGT145 also revealed one V1V2 Fab per Env trimer and details of quaternary contacts spanning the three gp120 protomers of Env (Lee et al., 2017; Liu et al., 2017).

A new V1V2 bNAb, BG1, was isolated along with bNAbs targeting non-overlapping sites on Env from an HIV-1 controller who developed elite levels of HIV-1 neutralizing activity (Freund et al., 2017). We characterized the binding properties of BG1 by performing biophysical studies to determine its stoichiometry of binding to an HIV-1 Env trimer and by solving structures of the BG1 Fab and a BG1 Fab-Env trimer complex. BG1 differs from other V1V2 antibodies in that two

BG1 Fabs bind per Env trimer to create a previously-unseen form of asymmetric recognition of the V1V2 loops at the Env trimer apex. This form of recognition does not require a protruding CDRH3, as found in other V1V2 bNAbs, and the BG1 epitope on Env trimer differs from previously-characterized V1V2 epitopes. The BG1 paratope may therefore represent a new target for HIV-1 vaccine development (Escolano et al., 2017).

Results

The heavy chains (HCs) of V1V2-directed bNAbs isolated from multiple donors contain long (28 – 35 residues) anionic CDRH3 loops (Figure 4.1A) that include sulfated/sulfonated tyrosines (Bonsignori et al., 2011; Doria-Rose et al., 2014; McLellan et al., 2011; Pan et al., 2015; Pancera et al., 2013; Walker et al., 2011; Walker et al., 2009). Structural studies of V1V2 bNAbs showed that the protruding CDRH3 is used to penetrate through the glycan shield on Env surrounding the $Asn160_{gp120}$ and $Asn156_{gp120}$ N-glycans to contact basic residues in the V2 loop (Gorman et al., 2016; McLellan et al., 2011; Pan et al., 2015; Pancera et al., 2010; Pancera et al., 2013; Pejchal et al., 2010). The BG1 CDRH3 length, 22 residues, is shorter than CDRH3 loops in other V1V2 bNAbs (Figure 4.1A), but longer than typical human antibody CDRH3s for which the most common length is 14 residues (Swindells et al., 2017). A 2.0 Å crystal structure of unbound BG1 Fab (Figure 4.1B; Table 4.1) revealed that, in contrast to the protruding CDRH3s in other V1V2 bNAbs, the BG1 CDRH3 does not extend notably beyond the antigen-binding site surface (Figure 4.1C). The relatively compact CDRH3 of BG1 results from folding into an irregular structure whose conformation is stabilized by $Tyr100C_{CDRH3}$ interactions with protein backbone atoms in CDRH1 and CDRH3 and by water-mediated H-bonds involving other residues (Figure 4.1D). None of the four tyrosines within the BG1 CDRH3 ($Tyr100A_{CDRH3}$, $Tyr100C_{CDRH3}$, $Tyr100J_{CDRH3}$ and $Tyr100L_{CDRH3}$) or within other CDRs show electron density for a sulfate group (Supplementary Figure 4.1). By contrast, the CRH3s of other V1V2 bNAbs form stable subdomains involving regions of two-stranded b-sheet (Figure 4.1E), sometimes containing sulfated tyrosine sidechains (e.g., PG9's $Tyr100G_{CDRH3}$ and $Tyr100H_{CDRH3}$) that interact with basic residues within V1V2 (Liu et al., 2017; McLellan et al., 2011; Pancera et al., 2013).

The CDRH2 loop of BG1 is two residues longer than CDRH2s of other V1V2 bNAbs (Figure 4.1A), and it extends further from the antigen-binding site than the CDRH2 loops of other V1V2 bNAbs. (Figure 4.1E). The combined effects of the relatively compact CDRH3 and protruding CDRH2 result in the BG1 antigen-binding site being more flat than the combining sites of other

V1V1 bNAbs (Figure 4.1E). The BG1 CDRH2 includes a solvent-exposed tryptophan at position 52B (Figure 4.1D) (lysine in the VH3-49*04 germline sequence from which BG1 is derived). Protein-protein interfaces often include surface-exposed hydrophobic residues (Dall'Acqua et al., 1996; Kelley and O'Connell, 1993; Wells and DeVos, 1996), suggesting that the long CDRH2, and this residue in particular, could be involved in the binding interface of BG1 with Env.

To characterize the BG1 interaction with Env, we determined the stoichiometry of binding of the BG1 Fab and Env trimer using size exclusion chromatography with multi-angle light scattering (SEC-MALS) and negative-stain EM single-particle analysis. SEC-MALS can be used to determine the stoichiometry of a complex by deriving the absolute molecular mass of the complex independent of shape and model (Wyatt, 1993). In the SEC-MALS experiment, we incubated a fully glycosylated soluble native-like Env trimer (BG505 SOSIP.664 (Sanders et al., 2013); hereafter called Env) with a 3-fold molar excess of a Fab from a V1V2 bNAb or with a Fab from the G52K5 variant of 8ANC195, a gp120-gp41–spanning bNAb (Scharf et al., 2014) (calculated assuming a molecular mass of 210 kDa for Env trimer). The molecular mass of the PG16 Fab–Env complex was consistent with a stoichiometry of 1 Fab per Env trimer (Figure 4.2A), as previously shown by SEC-MALS and negative-stain EM for PG9 (Julien et al., 2013b), and the 8ANC195–Env complex stoichiometry was 3 Fabs per trimer (Figure 4.2A), consistent with crystal and EM structures of 8ANC195–BG505 Env complexes (Scharf et al., 2015; Wang et al., 2016a). By contrast, the SEC-MALS profile for the BG1 Fab–Env complex indicated a stoichiometry of 2 Fabs per trimer (Figure 4.2A).

To confirm the conclusions from the SEC-MALS experiments, we examined the structures of BG1-Env-8ANC195, PG9-Env-8ANC195, and PG16-Env-8ANC195 complexes by negative-stain EM. Single-particle 3D reconstructions of these complexes at resolutions between 27 Å and 32 Å resolution (Figure 4.2B; Supplementary Figure 4.2) revealed three 8ANC195 Fabs bound to BG505 Env trimer in the expected positions at the gp120-gp41 interface (Scharf et al., 2014; Scharf et al., 2015; Wang et al., 2016a) of each complex. The BG1-Env-8ANC195 complex showed density for two BG1 Fabs per Env trimer, while the PG9-Env-8ANC195 and PG16-Env-

8ANC195 complexes each showed density for one Fab per trimer (Figure 4.2B). The positions of the single PG9 and PG16 Fabs at the apex of Env trimer were similar to each other and to a previous negative-stain PG9-Env structure (Julien et al., 2013b), whereas the BG1 Fabs bound Env in an orientation distinct from the orientations of PGT145 (Lee et al., 2017; Liu et al., 2017), PG9, and PG16 (Figure 4.2C).

The close proximity of two BG1 Fabs at the apex of Env trimer (Figure 4.2B) raised the possibility that BG1 IgG binds bivalently to Env trimer, which would result in increased avidity due to intra-spike crosslinking (Galimidi et al., 2015; Klein and Bjorkman, 2010). To evaluate this possibility, we compared the neutralization potencies of IgG and Fab forms of BG1 across multiple viral strains using in vitro neutralization assays (Montefiori, 2005) and calculated the molar neutralization ratio (MNR) for BG1 (defined as [IC_{50} Fab (nM)/IC_{50} IgG (nM)]; (Klein and Bjorkman, 2010)). This ratio would be 2.0 in the absence of avidity effects from intra-spike crosslinking or inter-spike crosslinking (which we argued is rare due to the low numbers and densities of spikes on HIV-1 virions (Galimidi et al., 2015; Klein and Bjorkman, 2010)), and no steric effects that would increase neutralization potencies for the larger IgGs versus the smaller Fabs (Klein and Bjorkman, 2010). Viruses with densely-packed spikes can exhibit MNRs over 1000 (Klein and Bjorkman, 2010), whereas mean MNRs for anti-HIV-1 bNAbs tend to be low (Galimidi et al., 2015; Klein and Bjorkman, 2010; West et al., 2012).

We found that the geometric mean MNR for BG1 was 8.4, sd_{geom} (geometric standard deviation) = 2.4 (Supplementary Table 4.1). To put this result into context, we derived MNRs using published data (Galimidi et al., 2015; West et al., 2012) for bNAbs that should not be capable of bivalent binding to a single Env trimer: PG9 and PG16 (because only one Fab binds per trimer), and the CD4bs bNAbs VRC01 and 3BNC60, whose adjacent epitopes on neighboring gp120s are located in positions that would not permit simultaneous binding by both Fabs of an IgG. The mean MNRs for these bNAbs were comparable to the mean MNR for BG1 (PG9: 6.0, sd_{geom} = 4.1; PG16: 10.3, sd_{geom} = 3.4; VRC01: 4.8, sd_{geom} = 3.1; 3BNC60: 8.1, sd_{geom} = 3.2) (Supplementary Table 4.2, 4.3). By contrast, the mean MNR for a 3BNC60-based reagent that exhibited neutralization potency increases suggestive of intra-spike crosslinking (a bivalent form of 3BNC60 in which two 3BNC60

Fabs were joined by a double-stranded DNA linker (Galimidi et al., 2015)) was 141, sd_{geom} = 2.1 (Supplementary Table 4.3). These results suggest that, like other natural HIV-1 bNAbs, BG1 IgG does not bind bivalently to Env trimers during neutralization.

In order to explore the details of how two BG1 Fabs bind asymmetrically to the three V1V2 loops in an Env trimer, we used single-particle cryo-EM to solve the structure of a BG1-Env complex. A single-particle reconstruction of a BG1-Env-8ANC195 complex with two BG1 Fabs per Env trimer was obtained at a resolution of ~6.2 Å (calculated using the 0.143 gold-standard Fourier shell coefficient cutoff criterion) (Scheres and Chen, 2012) (Figure 4.3; Supplementary Figure 4.3, 4.4; Table 4.2). To interpret the structure, the coordinates of BG1 Fab (this study) and 8ANC195 Fab (PDB code 4P9M) were fit by rigid body docking into the cryo-EM densities, after which the coordinates for three gp41 monomers (PDB 5FUU) (Lee et al., 2016) and three gp120 monomers (PDB 5T3X) (Gristick et al., 2016) were fit independently (Figure 4.3A). Coordinates for ordered N-linked glycans from a natively-glycosylated BG505 Env trimer structure (PDB 5T3X) (Gristick et al., 2016) were fit separately as rigid bodies at potential N-linked glycosylation sites (PNGSs) at which EM density was apparent (Figure 4.3B). After initial rigid body docking, refinement of the protein portions of the complex was carried out with geometric restraints for protein and N-glycan residues (Adams et al., 2010; Agirre et al., 2015). Unlike the PG9 Fab, in which the CDRH3 loop is ordered only when bound to the V1V2 scaffold (McLellan et al., 2011), the CDRH3 of BG1 was ordered in both the unbound (Figure 4.1E) and bound (Figure 4.3C) states. Within the limits of the resolution of the cryo-EM structure, the CDRH3 and CDRH2 loops of BG1_A and BG1_B adopted the same conformation as their counterparts in the unbound BG1 crystal structure (Figure 4.3C,D). In particular, the relatively compact CDRH3 loop observed in the unbound BG1 crystal structure (Figure 4.1E) was maintained in the 2:1 BG1-Env structure (Figure 4.3C). A 27 Å BG1-Env-8ANC195 complex with three BG1 Fabs per Env trimer (3:1 BG1-Env) was also reconstructed from a minor subset of the total particles (<10%) (Supplementary Figure 4.3), and coordinates were fit to the density by rigid body refinement (Supplementary Figure 4.4).

We also solved an 11.5 Å single-particle cryo-EM reconstruction of a PG9-Env-8ANC195 complex (Figure 4.4; Supplementary Figure 4.5). As described for the BG1-Env-8ANC195 cryo-

EM structure, coordinates of PG9 Fab (PDB 3U36) were fit, after which gp120 and gp41 subunits were fit independently. Since the CDRH3 of unliganded PG9 Fab (PDB 3U36) is disordered, we modeled the unliganded PG9 coordinates and the ordered CDRH3 from the PG9 Fab in the PG9-V1V2 scaffold structure (PDB 3U4E) (McLellan et al., 2011) separately into the EM density. The position of the single PG9 Fab on Env trimer in the cryo-EM structure was consistent with negative-stain structures reported here and previously (Julien et al., 2013b). The angle of approach of the PG9 Fab was different in the PG9-Env interaction predicted from modeling the PG9 Fab-monomeric V1V2 scaffold structure (McLellan et al., 2011) onto Env trimer versus in the PG9-Env EM structure (Figure 4.4B), likely due to accommodating glycans in a neighboring gp120 protomer in the trimeric Env that are not present in a monomeric V1V2 scaffold.

The 6.2 Å BG1-Env-8ANC195 structure with two BG1 Fabs (2:1 BG1-Env) showed interactions with two of the three gp120 protomers within Env trimer. To distinguish the structurally-distinct gp120 and BG1 subunits within the 2:1 BG1-Env structure, we defined the two gp120 subunits of Env that interact with BG1 Fabs as gp120_A and gp120_B, the corresponding BG1 Fabs as BG1_A and BG1_B, and the third gp120 subunit, which showed no contacts with BG1 Fabs, as gp120_C (Figure 4.3A; Figure 4.5A).

To compare the BG1-Env and PG9-Env interactions, we calculated approximate footprints of the each antibody on Env trimer (epitopes) and of Env on each antibody (paratopes). For the BG1-Env interaction, we used coordinates fit to the 6.2 Å BG1-Env structure, and for the PG9-Env interaction, we used coordinates fit to the 11.5 Å PG9-Env structure. To account for low resolution and/or modeling errors, we assigned contacts using a criterion of a distance of ≤7 Å between antibody-antigen Ca atoms for protein-protein contacts and ≤7 Å between protein Ca and glycan C1 atoms for antibody-antigen-glycan contacts. As shown in Figure 5A, the contact analysis predicted that both Fabs reached through the glycan shield between the $Asn156_{gp120}$ and $Asn160_{gp120}$ glycans to contact underlying V1V2 protein residues, but only PG9 made contacts with basic residues in a lysine-rich region of the V2 loop ($Lys168_{gp120}$ and $Lys169_{gp120}$). This prediction was validated by an analysis of in vitro neutralization data demonstrating that

substitution of $Lys169_{gp120}$ reduces neutralization potency for PG9, but has only minor effects on BG1 (Supplementary Figure 4.6). Conversely, substitution of $Thr132_{gp120}$ had more of an effect on BG1 neutralization than on PG9 neutralization (Supplementary Figure 4.6B).

Predicted protein-protein contacts were mediated by different CDR loops for BG1 versus PG9: CDRH2 for BG1 and CDRH3 for PG9. Contacts with Env glycans were also made differently for BG1 and PG9: The $Asn156_{gp120}$ glycan on both gp120_A and gp120_B was contacted by the BG1 CDRL1, and the $Asn160_{gp120}$ glycan was contacted on both gp120s by the CDRH2 and CDRH3 loops of BG1 and also by the CDRL3 in the case of BG1_B. By contrast, PG9 contacted only the $Asn160_{gp120}$ glycan on gp120_B, and these contacts were mediated exclusively by CDRH3. Examination of the paratopes on BG1 versus PG9 illustrated that BG1 uses several CDRs for interacting with Env, whereas PG9 uses only its protruding CDRH3 (Figure 4.5B; Figure 4.6A,B). In particular, Trp52B within CDRH2 of the BG1 heavy chain is in the vicinity of the protein portion of the V1V2 epitope (Figure 4.3D).

Comparison of the BG1 and PG9 epitopes on Env trimer rationalize differences in their relative neutralization potencies across HIV-1 strains. To find Env sequence features that contribute to BG1 potency variations, we analyzed in vitro neutralization results using previously-described methods (West et al., 2013). The analysis revealed that the presence of a potential N-linked glycosylation site (PNGS) at position 130 of gp120 correlated with weaker BG1 neutralization (geometric mean IC_{50} = 25.7 μg/mL for strains including PNGS 130, versus 1.5 μg/mL for strains lacking PNGS 130) (Figure 4.5A; Supplementary Figure 4.6). PG9 was also more potent on strains lacking PNGS 130 (geometric mean IC_{50} = 0.76 μg/mL for strains including PNGS 130, versus 0.24 μg/mL for strains lacking PNGS 130); however, the difference was larger for BG1 (17-fold for BG1 versus 3-fold for PG9). This result is rationalized by the BG1 and PG9 epitopes on Env trimer: although residue 130 ($Gln130_{gp120}$) is not part of a PNGS in the BG505 strain of Env in our structural studies, residue 130 lies directly within the protein region contacted by BG1, but is outside of the PG9 footprint (Figure 4.5A), suggesting that addition of an N-glycan at position 130 would more directly disrupt BG1 binding than PG9 binding.

To identify important common features of the BG1_A–gp120_A and BG1_B–gp120_B interactions, we aligned the two BG1-gp120 complexes by superimposing either the protein coordinates of the two V1V2 regions (Figure 4.7A) or by superimposing the $Asn156_{gp120}$ and $Asn160_{gp120}$ glycans of gp120_A and gp120_B (Figure 4.7B). When aligning the protein coordinates of the two V1V2 regions, the BG1 V_H-V_L domains superimposed with a root mean square deviation (rmsd) of 7.7 Å for 435 Ca atoms. The rmsd for the same number of Ca atoms decreased to 2.9 Å when we superimposed the $Asn156_{gp120}$ and $Asn160_{gp120}$ glycans of the two V1V2 regions. This comparison suggests that glycan contacts play a larger role than protein contacts in determining how BG1 recognizes the V1V2 epitope on Env.

To address why the 6.2 Å BG1-Env-8ANC195 structure shows two BG1 Fabs arranged asymmetrically on Env trimer, rather than three symmetrically-arranged BG1 Fabs, we used modeling to construct an Env complex containing a third BG1 Fab. The V_H-V_L domains for a third BG1 Fab (BG1 model) were positioned onto the gp120_C subunit assuming that a third BG1 Fab would interact with the $Asn156_{gp120}$ and $Asn160_{gp120}$ glycans in the common interaction observed for BG1_A and BG1_B (Figure 4.7B). Predicted van der Waals clashes (red dots) demonstrated that a third BG1 Fab cannot be accommodated on the Env trimer structure without steric clashing (Figure 4.7C). However, as indicated by the minor population of Env trimers with three BG1 Fabs in the 3:1 BG1-Env structure (Supplementary Figure 4.4), binding of three Fabs is possible (Figure 4.7D). When three Fabs were bound, the Env trimer appeared more open than Env in the 2:1 BG1-Env structure, as shown by a comparison of the BG1 Fab positions in the 2:1 and 3:1 BG1-Env structures (Figure 4.7E).

Discussion

The V1V2 epitope on HIV Env is targeted by bNAbs that make quaternary interactions that prevent opening of Env trimer to expose the V3 loop and coreceptor binding site, hence blocking conformational changes leading to fusion of the viral and host cell membranes (Bonsignori et al., 2011; Doria-Rose et al., 2014; McLellan et al., 2011; Pan et al., 2015; Pancera et al., 2013; Walker et al., 2011; Walker et al., 2009). Quaternary interactions visualized thus far for V1V2 bNAbs involve the binding of a single Fab to the apex of Env trimer (Julien et al., 2013b; Liu et al., 2017), but here we demonstrate that the stoichiometry of binding for the new V1V2 bNAb BG1 (Freund et al., 2017) is two Fabs per Env trimer, with a minor population of 3:1 BG1-Env complexes (Figures 4.2, 4.3; Supplementary Figure 4.3).

We previously noted that epitopes for HIV-1 bNAbs are located in positions not predicted to allow simultaneous binding of both Fabs from an IgG to a single Env trimer (Galimidi et al., 2015; Klein and Bjorkman, 2010). By definition, the two Fabs in IgG forms of V1V2 bNAbs that exhibit a 1 Fab per Env trimer stoichiometry cannot bind with avidity to an Env trimer, and epitopes on HIV-1 Env that show a 3:1 Fab-Env stoichiometry are located in positions that are too far apart to allow simultaneous binding of both Fabs in an IgG to one Env (Galimidi et al., 2015; Klein and Bjorkman, 2010). However, the V1V2 bNAb BG1 binds with a 2:1 Fab-Env stoichiometry to an epitope in close proximity on neighboring gp120 subunits at the apex of Env, suggesting that it might be possible for both Fabs of a single BG1 IgG to bind simultaneously to a single Env trimer. However, comparisons of neutralization potencies of BG1 Fab and IgG suggested that, as found for other HIV-1 bNAbs, potential avidity effects for BG1 IgG were marginal (Supplementary Table 4.1), consistent with no intra-spike crosslinking and only minimal inter-spike crosslinking or steric effects favoring an IgG over a Fab. The apparent absence of intra-spike crosslinking for BG1 IgG can be rationalized by the angle of approach the Fabs adopted in the 2:1 BG1-Env structure: adjacent Fabs were oriented such that they point away from each so that the C-termini of the C_H1 domains (to which the N-terminus of an IgG Fc would be attached) are too far apart (~85 Å) to be

spanned by a natural IgG hinge region (e.g., the C-termini of the two Fabs in the crystal structure of intact IgG b12 (Saphire et al., 2001) (PDB 1HZH) are separated by ~18 Å). Thus it appears that HIV-1 Env has evolved to prevent bivalent binding by IgGs to Env trimer even when Fabs from two separate IgGs can bind to nearby epitopes.

Previously-characterized V1V2 bNAbs made primary interactions with Env that involved a long, negatively-charged CDRH3 that reached through the Env glycan shield to contact basic residues in the V2 loop (Bonsignori et al., 2011; Doria-Rose et al., 2014; Julien et al., 2013b; Liu et al., 2017; McLellan et al., 2011; Pan et al., 2015; Pancera et al., 2013; Walker et al., 2011; Walker et al., 2009). Although BG1 is directed against the same general region of Env, its epitope shows glycan interactions dominating over protein interactions, and the relatively long BG1 CDRH3 (Figure 4.1A) is folded into a compact structure (Figure 4.1D,E) that is used to make contacts with Env glycans rather than Env protein residues (Figure 4.5A). The role of reaching through the glycan shield to contact protein residues is taken by BG1's unusually long CDRH2 (Figure 4.1E), resulting in a different epitope footprint on Env than seen for typical V1V2 bNAbs such as PG9 (Figure 4.5A).

Examination of the interactions of the two BG1 Fabs in the 2:1 BG1-Env complex solved by single particle cryo-EM suggests differences in the BG1_A and BG1_B interfaces with Env. The BG1_B Fab interacts not only with glycans on its primary subunit contact gp120_B; the complex structure also suggests a potential secondary interaction with the $Asn160_{gp120}$ glycan on a neighboring subunit, gp120_A, using CDRL1 (Figure 4.6A, right panel). By contrast to the BG1_B interactions with Env trimer, the 2:1 BG1-Env structure does not predict secondary contacts for BG1_A, a difference that may explain why BG1_A and BG1_B showed distinct angles of approach when we aligned the BG1_A–gp120_A and BG1_B–gp120_B complexes by superimposing the protein coordinates of the V1V2 regions (Figure 4.7A). Differences in the interactions of BG1_A and BG1_B with Env trimer suggests a model for BG1 Fab binding to Env (Figure 4.7F): If BG1_B binds first to the V1V2 epitope on gp120_B, its CDRL1 could then interact with the $Asn160_{gp120}$ glycan from gp120_A. After that, a second BG1 Fab, BG1_A, could recognize the $Asn156_{gp120}$ and $Asn160_{gp120}$ glycans from gp120_A. Because of the interaction between the BG1_B CDRL1 and

the Asn160$_{gp120}$ glycan from gp120_A, the angle of approach of BG1_B is shifted further towards the Env trimer 3-fold axis as compared with the angle of approach of with BG1_A (Figure 4.7C; fourth panel). In this model, the intrinsic flexibility of N-linked glycans would allow BG1_A to capture an Env conformation in which the glycans are shifted away from the trimer 3-fold axis such that a potential clash with BG1_B is avoided. In this binding mode, a third BG1 Fab cannot bind because it would clash with BG1_B. However, if the Fabs can capture a more open state of Env trimer in the absence of CD4 binding, three Fabs can be accommodated (Figure 4.7D,E). The low percentage of 3:1 BG1-Env complexes observed by cryo-EM (Supplementary Figure 4.3), despite incubation with a 9-fold molar excess of BG1 Fab (Methods), suggests that formation of 3:1 BG1-Env complexes is rare.

Our direct comparisons of BG1-Env and PG9-Env stoichiometry and cryo-EM structures illustrate the diversity of bNAb recognition of the V1V2 epitope at the apex of HIV-1 Env trimer. These results provide new information relevant to design of immunogens to raise antibodies against V1V2 (Escolano et al., 2017), an important target because the V1V2 loops are critical for maintaining the closed Env trimer structure in which the coreceptor binding site is shielded and conformational changes leading to fusion of the viral and host cell membranes are prevented. The more typical form of V1V2 recognition, in which a protruding CDRH3 from, e.g., PG9, is used to reach through the Asn156$_{gp120}$ and Asn160$_{gp120}$ glycans to contact protein residues on the V2 loop, results in a more potent bNAb (Figure 4.5A; Supplementary Figure 4.6). By contrast, the BG1 mode of V1V2 recognition, which is less potent, relies more on glycan contacts using relatively compact CDRs, and BG1's contacts with V1V2 protein residues are more easily disrupted by glycosylation at PNGS 130 (Figure 4.5A; Supplementary Figure 4.6). Thus immunogens designed to raise bNAbs against the V1V2 epitope would likely require removal of the Asn130$_{gp120}$ glycan in order to target both BG1- and PG9-style V1V2 bNAbs.

Methods

Protein Expression and Purification

Fabs (BG1, PG9, PG16, and the G52K5 variant of 8ANC195 (Scharf et al., 2014)) and BG1 IgG were expressed and purified as described (Scharf et al., 2016). Briefly, IgGs and 6xHis-tagged Fabs were expressed by transient transfection of HC and LC expression plasmids into HEK293-6E cells. Fabs and BG1 IgG were purified from cell supernatants using Ni-NTA (GE Healthcare) (for Fabs) or protein A (GE Healthcare) (for IgG) affinity chromatography followed by SEC on a Superdex 200 16/60 column (GE Healthcare). Proteins were stored in 20 mM Tris, pH 8.0, and 150 mM sodium chloride (TBS buffer) supplemented with 0.02% (wt/vol) sodium azide.

Structural studies of Fab-Env complexes were done using BG505 SOSIP.664, a soluble clade A gp140 trimer that includes 'SOS' substitutions ($A501C_{gp120}$, $T605C_{gp41}$), the 'IP' substitution ($I559P_{gp41}$), the N-linked glycan sequence at residue 332_{gp120} ($T332N_{gp120}$), an enhanced gp120-gp41 cleavage site (REKR to RRRRRR), and a stop codon after residue 664_{gp41} (Env numbering according to HX nomenclature) (Sanders et al., 2013). Protein was expressed in HEK293-6E cells (National Research Council of Canada) in the absence of kifunensine by transient transfection of plasmids encoding BG505 SOSIP and soluble furin at a ratio of 4:1 as previously described (Gristick et al., 2016). We isolated BG505 SOSIP protein from cell supernatants using a 2G12 immunoaffinity column made by covalently coupling 2G12 IgG monomer to an NHS-activated Sepharose column (GE Healthcare). Protein was eluted with 3M $MgCl_2$ followed by immediate buffer exchange into Tris-buffered saline pH 8.0 (TBS), and trimers were purified using Superdex 200 16/60 SEC (GE Healthcare), and then stored in TBS.

V1V2 Fab-Env-8ANC195 complexes were prepared for negative-stain and cryo-EM by incubating purified Env with a 9-fold molar excess of V1V2 Fab (either BG1, PG9, or PG16) overnight at 4 ˚C and then continuing the incubation with a 9-fold molar excess of 8ANC195 Fab. The ternary complex was isolated by SEC using a Superose 6 10/300 column (GE Healthcare).

X-ray Structure Determination

Crystals of BG1 Fab were obtained by combining 0.2 mL of a 10 mg/mL protein solution with 0.2 mL of 1.8 M ammonium sulfate, 0.1 M Bis-Tris pH 6.5, 2% v/v PEG 550 MME and 100 nM NDSB-256 at 20°C and cryoprotected in mother liquor supplemented with 20% (v/v) ethylene glycol. X-ray diffraction data were collected using a Pilatus 6M pixel detector (Dectris) at the Stanford Synchrotron Radiation Lightsource beamline 12-2. XDS was used to index, integrate and scale the data (Kabsch, 2010), and the structure was refined to 1.9 Å by iteratively refining with Phenix (Adams et al., 2010) and manual model building in Coot (Emsley and Cowtan, 2004). The BG1 Fab structure was solved by molecular replacement using 2909 Fab (PDB code 3PIQ) V_HV_L with CDR loops removed and C_H1C_L as search models. The final model (R_{work} = 18.9%, R_{free} = 21.2%) omits the following disordered residues: $Ser146_{HC}$-$Gly154_{HC}$, $Gly210_{HC}$-$Thr211_{HC}$, $Lys234_{HC}$-$Thr239_{HC}$, and $Cys214_{LC,}$ and has 96.7%, 3.3% and 0% of residues in the favored, allowed and disallowed regions, respectively, of the Ramachandran plot (Table 4.1). Hydrogen bonds were assigned using the following criteria: a distance of < 3.5 Å, and an A-D-H angle of > 90˚. Structures were superimposed and figures generated with PyMOL (Schrödinger, 2011) and UCSF Chimera (Pettersen et al., 2004). Rmsd calculations were done in PyMOL following pairwise Cα alignments without outlier rejection.

SEC-MALS

Purified Env, Fab, and Env-Fab complexes were characterized by SEC-MALS to determine absolute molecular masses (Wyatt, 1993). 80 µL of 1 mg/mL BG505 SOSIP.664 was mixed with a 3-fold molar excess of Fab (PG16, BG1, or $8ANC195_{G52K5}$) relative to Env trimer, and the reaction volume brought up to 100 µL with sample buffer containing 20 mM Tris (pH 8.0) and 150 mM NaCl. For controls, reactions containing individual components of BG505 SOSIP.664 or Fab were prepared in the same manner. The proteins or protein complexes were then equilibrated overnight at room temperature and injected onto a Superdex 200 10/300 GL gel-filtration chromatography column equilibrated with our sample buffer. The chromatography column was connected with an 18-angle light-scattering detector (DAWN HELEOS II; Wyatt Technology), a dynamic light-scattering detector (DynaPro Nanostar; Wyatt Technology), and a refractive index detector

(Optilab t-rEX; Wyatt Technology). Data were collected at 25°C at a flow rate of 0.5 mL/min every 1 second. The molecular mass of each protein or protein complex was obtained by data analysis using the program ASTRA 6.

Neutralization Assays.

Pseudovirus neutralization assays were conducted as described (Montefiori, 2005) by the Collaboration for AIDS Vaccine Discovery (CAVD) core neutralization facility for calculation of MNRs (defined in (Klein and Bjorkman, 2010)) for BG1 (Supplementary Table 4.1). MNRs for other HIV-1 bNAbs came from data published in previous papers (Galimidi et al., 2015; West et al., 2012). Average IC_{50} values and MNRs are geometric means calculated using the formula $(\prod a_i)^{(1/n)}$; $i = 1, 2, ..., n$. Geometric means are preferred statistics for data sets covering multiple orders of magnitude (Sheskin, 2004), as is found for neutralization data across multiple viral strains. For calculating mean IC_{50} values, strains with reported IC_{50}s of >n μg/mL were included as n μg/mL. Geometric standard deviations were calculated as the exponential of the standard deviation of the logarithms of the individual MNRs.

Negative-stain EM Data Collection and Processing

Purified V1V2 Fab-8ANC195-Env complexes (where the V1V2 Fab was either BG1, PG9, or PG16) were diluted to 10 μg/mL in TBS immediately before adding 3 μL to a glow discharged ultrathin C film on holey carbon support film, 400 mesh, Cu grids (Ted Pella, Inc.). Samples were stained with 3% uranyl acetate. Data were collected using FEI Tecnai T12 transmission electron microscope at 120 keV on a Gatan Ultrascan 2k x 2k CCD detector. Images were acquired using a 1 sec exposure time at a nominal magnification of 42,000x at 1 μm defocus, resulting in 2.5 Å per pixel. Particles were picked using manual picking in EMAN2.1 (Tang et al., 2007), and the CTF correction was done using EMAN2.1 (Huang et al., 2007). Initial reference-free 2D class averaging was performed using RELION (Scheres, 2012). After 2D classification, particles corresponding to good class averages were selected (Supplementary Figrue 4.2), and the particles were further sorted using 3D classification in RELION. A reference model was generated by docking a PG9-V1V2 scaffold structure (PDB 3U4E) onto an Env trimer structure in complex with 8ANC195 (PDB 5CJX) and low pass filtering the model to 60 Å. Refinement for each of the complex

structures was conducted using the best reconstruction from the 3D classification as a reference. The resolutions of final reconstructions were calculated with RELION (Scheres, 2012) using a gold-standard FSC and a 0.143 cutoff as recommended for resolution estimations for single particle EM reconstructions (Scheres and Chen, 2012) (Supplementary Figrue 4.2D).

Cryo-EM Data Collection and Processing

Purified BG1-Env-8ANC195 complex was diluted to 60 μg/mL in TBS and vitrified in liquid ethane using a Mark IV Vitrobot. Sample grids were prepared by adding 3 μL of complex to glow discharged 200 Mesh Quantifoil R1.2/1.3 copper grids. Images were recorded using SerialEM (Mastronarde, 2005) on a Titan Krios electron microscope equipped with Gatan K2 Summit direct detector and an energy filter with a slit width of 20 eV. Exposures (15 sec) were divided into 50 subframes with a dose rate of 2.92 electrons·pixel^{-1}·subframe^{-1}. After binning by 2 and motion correction, each image was 4k × 4k and 1.35 Å per pixel.

The dataset was motion corrected and dose weighted using Unblur and Summovie (Brilot et al., 2012; Campbell et al., 2012; Grant and Grigorieff, 2015). Motion-corrected micrographs without dose weighting were used for contrast transfer function (CTF) estimations. Motion-corrected micrographs with dose weighting were used for particle picking, and motion-corrected micrographs with dose weighting and restored noise power after filtering were used for all classification and refinement processes.

Particles were picked using the SWARM method of EMAN2.1 (Tang et al., 2007) (Supplementary Figure 4.3A), and CTF estimations were done using CTFFIND4 (Rohou and Grigorieff, 2015) (Supplementary Figure 4.3B). A total of 2837 movies were collected. After motion correction and dose weighting, CTF curves were confidently fit beyond 6 Å in 1371 micrographs; the others were discarded. A total of ~100,000 particles were picked. Particles were classified in 2D with RELION (Scheres, 2012), resulting in 1000 2D classes. Of these, 28 classes from 76k particles were selected as “good” classes (Supplementary Figure 4.3C). For 3D classification, the negative-stain BG1-Env-8ANC195 structure (Figure 4.2B) was used as a reference for initial 3D classification; eight 3D classes were then produced. After selecting three

3D classes as "good" classes, 66k particles remained for 3D refinement (Supplementary Figure 4.3C). Post-processing, particle polishing, and gold-standard FSC estimations were done after 3D refinement using RELION (Scheres, 2012) following procedures in the tutorial. Particle polishing did not improve the resolution of the reconstruction (data not shown), which was estimated to be 6.18 Å (Supplementary Figure 4.4A). Angular distribution plots showing were generated using RELION (Scheres, 2012) and visualized in UCSF Chimera (Goddard et al., 2007) (Supplementary Figure 4.4B; Supplementary Figure 4.5C). Local resolution estimations were done using ResMap (Kucukelbir et al., 2014) (Supplementary Figure 4.4C; Supplementary Figure 4.5D).

Using particles in the 6.18 Å reconstruction, we did another round of 3D classification in which the C_H-C_L domains of the two BG1 Fabs and the three 8ANC195 Fabs were masked out (Supplementary Figure 4.3C) to account for the ability of Fab C_H-C_L domains to adopt multiple conformations with respect to V_H-V_L domains due to different elbow bend angles (Stanfield et al., 2006). After selecting two 3D classes as "good" classes, 37k particles remained for 3D refinement (C_H-C_L domains were also masked out during 3D refinement), which generated a structure that was also estimated to be 6.18 Å resolution using the gold standard FSC (Supplementary Figure 4.4A). Unless otherwise noted, the reconstruction derived without masking out C_H-C_L domains was used for structural analyses.

Although we used the 2:1 BG1-Env-8ANC195 reconstruction from negative-stain EM as the reference for 3D classification, one subclass (generated from 6.8% of all particles after 2D classification) contained density corresponding to three BG1 Fabs after the first round of 3D classification (Supplementary Figure 4.3C; Supplementary Figure 4.4E). Particles within that subclass were further refined (using a 60 Å low-pass-filtered reconstruction of that subclass during 3D classification) and post-processed following the standard procedure described in the RELION tutorial, resulting in a 27 Å structure of three BG1 Fabs bound to the Env-8ANC195 complex.

Purified PG9-Env-8ANC195 complexes were used to prepared sample grids as described for BG1-Env-8ANC195 complexes. Images were recorded on a Titan Krios electron microscope equipped with a Falcon II direct detector using FEI's automated data collection software EPU. 2-sec

exposures were divided into 7 subframes, and the dose rate was 13.125 electrons·pixel^{-1}·subframe^{-1}. After binning by 2 and motion correction, each image was 4k × 4k and 1.75 Å per pixel. A total of 1767 movies were collected. The dataset was processed as described for the BG1-Env-8ANC195 complex. After motion correction and dose weighting, CTF curves were confidently fit to beyond 8 Å in 1223 micrographs; the others were discarded. A total of ~19k particles were picked. Particles were classified in 2D with RELION (Scheres, 2012), resulting in 200 2D classes. Of these, 15 classes from 12k particles were selected as "good" classes (Supplementary Figure 4.5A). For 3D classification, the negative-stain structure of PG9-Env-8ANC195 (Figure 4.2B) was used as a reference for initial 3D classification; two 3D classes were then produced. After selecting one 3D class as a "good" class, 9.5k particles remained for 3D refinement (Supplementary Figure 4.5A). The angular distribution of all refinement particles were generated using RELION (Scheres, 2012) and visualized in UCSF Chimera (Goddard et al., 2007) (Supplementary Figure 4.5C). Local resolution estimations were done by using ResMap (Kucukelbir et al., 2014) (Supplementary Figure 4.5D). After 3D refinement, postprocessing and gold-standard FSC estimations were done by using RELION (Scheres, 2012) following procedures in the tutorial (Supplementary Figure 4.5B).

Model Building

Coordinates from crystal structures of individual components of the V1V2 Fab-Env-8ANC195 were fit by rigid body docking into cryo-EM density maps. The coordinates of 8ANC195 Fab [Protein Data Bank (PDB 4P9M) and BG1 Fab (this study) were first docked into the corresponding densities, after which three gp41 monomer coordinates from a JR-FL trimer structure (PDB 5FUU) (Lee et al., 2016) were fit. We used the JR-FL gp41 coordinates because they included coordinates for the fusion peptide and $HR1_N$ regions (Lee et al., 2016). Residues that differed between the JR-FL and BG505 gp41 were altered, and residues outside of EM density were deleted. Three gp120 monomers from a natively-glycosylated BG505 Env structure (PDB 5T3X) (Gristick et al., 2016) were fit individually into protomer densities. Coordinates for ordered N-linked glycans from the natively-glycosylated Env structure (PDB 5T3X) (Gristick et al., 2016) were fit separately as rigid bodies at potential N-linked glycosylation sites (PNGSs) at which EM density was apparent (Figure 4.3B). Glycan rings outside of EM density were removed. After

initial rigid body docking, refinement of the complex was carried out using phenix.real_space_refine with secondary structure restraints for protein and geometric restraints for protein and N-glycan residues (Adams et al., 2010; Agirre et al., 2015).

Figures

Figure 4.1

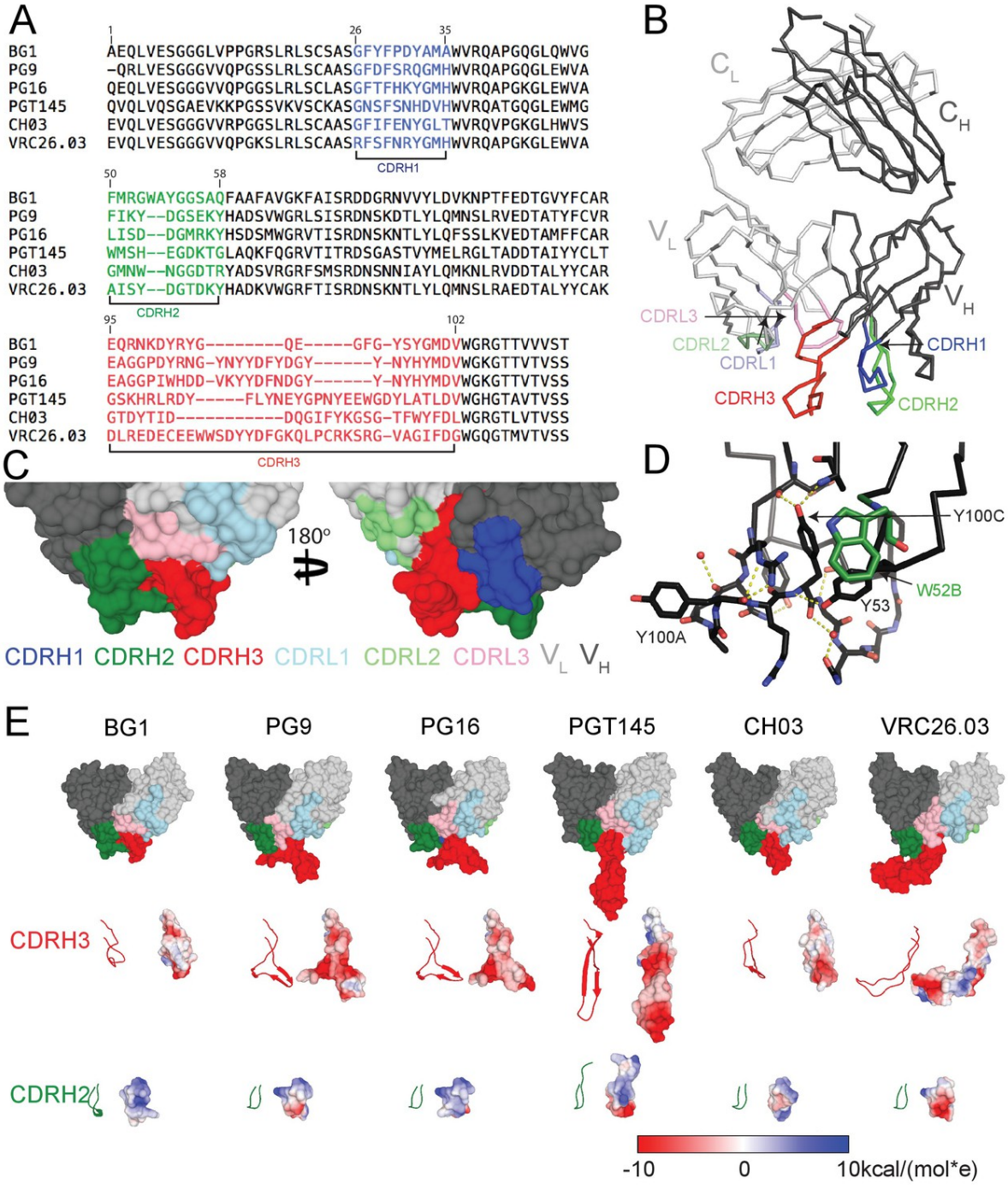

Figure 4.1. Comparison of BG1 and other V1V2 bNAbs.

(A) Sequences of the HCs of BG1 and representative other V1V2 bNAbs. Residue numbering (Kabat) refers to BG1, and the CDRs were defined using AbM (Swindells et al., 2017). (B) Crystal structure of BG1 Fab with highlighted CDRs. (C) Space-filling representations of antigen-binding site of BG1 in two orientations with CDRs highlighted. (D) Hydrogen bonds (dotted yellow lines) contributing to compact structure of CDRH3. Water molecules shown as red spheres. (E) Top: Space-filling representations of V_H-V_L domains of selected V1V2 bNAbs (BG1: this study; PG9: PDB 3U4E; PG16: PDB 3MUG; PGT145: PDB 3U1S; CH03: PDB 5ESV; VRC26.03: PDB 4OD1). Residues within CDRs are highlighted. CDRH3 (middle) and CDRH2 (bottom) loops shown in ribbon (left) and space-filling (right) representations. Electrostatic potentials are shown on the space filling representations using blue and red for positive and negative electrostatic potentials, respectively.

Figure 4.2

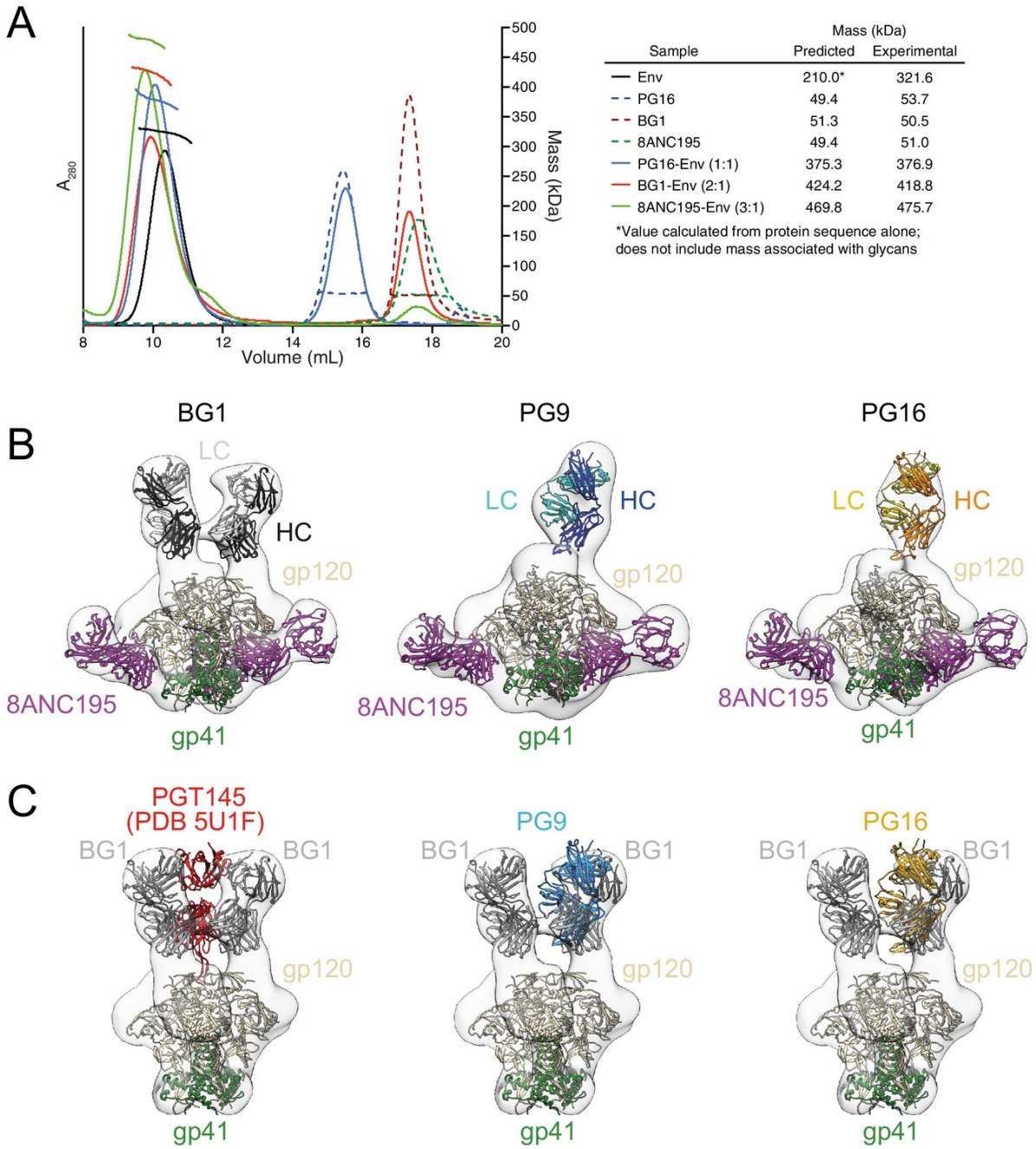

Figure 4.2. Fab-Env binding stoichiometries for V1V2 bNAbs.

(A) SEC-MALS profiles for BG505 SOSIP.664 Env trimer and complexes of Env trimer with BG1, PG16, and 8ANC195 Fabs. The absorbance at 280 nm (left y-axis) is plotted against elution volume from a Superdex 200 10/300 GL gel filtration column and overlaid with the molar mass determined for each peak (right y-axis). Predicted and calculated molecular masses are shown in the table. (B) Negative-stain single particle EM reconstructions BG1-Env-8ANC195, PG9-Env-8ANC195, and PG16-Env-8ANC195 complexes. EM density was fit with coordinates for the indicated Fabs and for BG505 Env trimer. (C) Density and coordinates from the BG1-Env portion of the BG1-Env-8ANC195 reconstruction (density for 8ANC195 Fabs removed) with coordinates for the indicated Fabs superimposed. The Env trimer portion from EM structures of complexes of PGT145-Env (PDB 5U1F), PG9-Env (panel B), or PG16-Env (panel B) were superimposed with the Env trimer portion of the BG1-Env-8ANC195 structure (panel B).

Figure 4.3

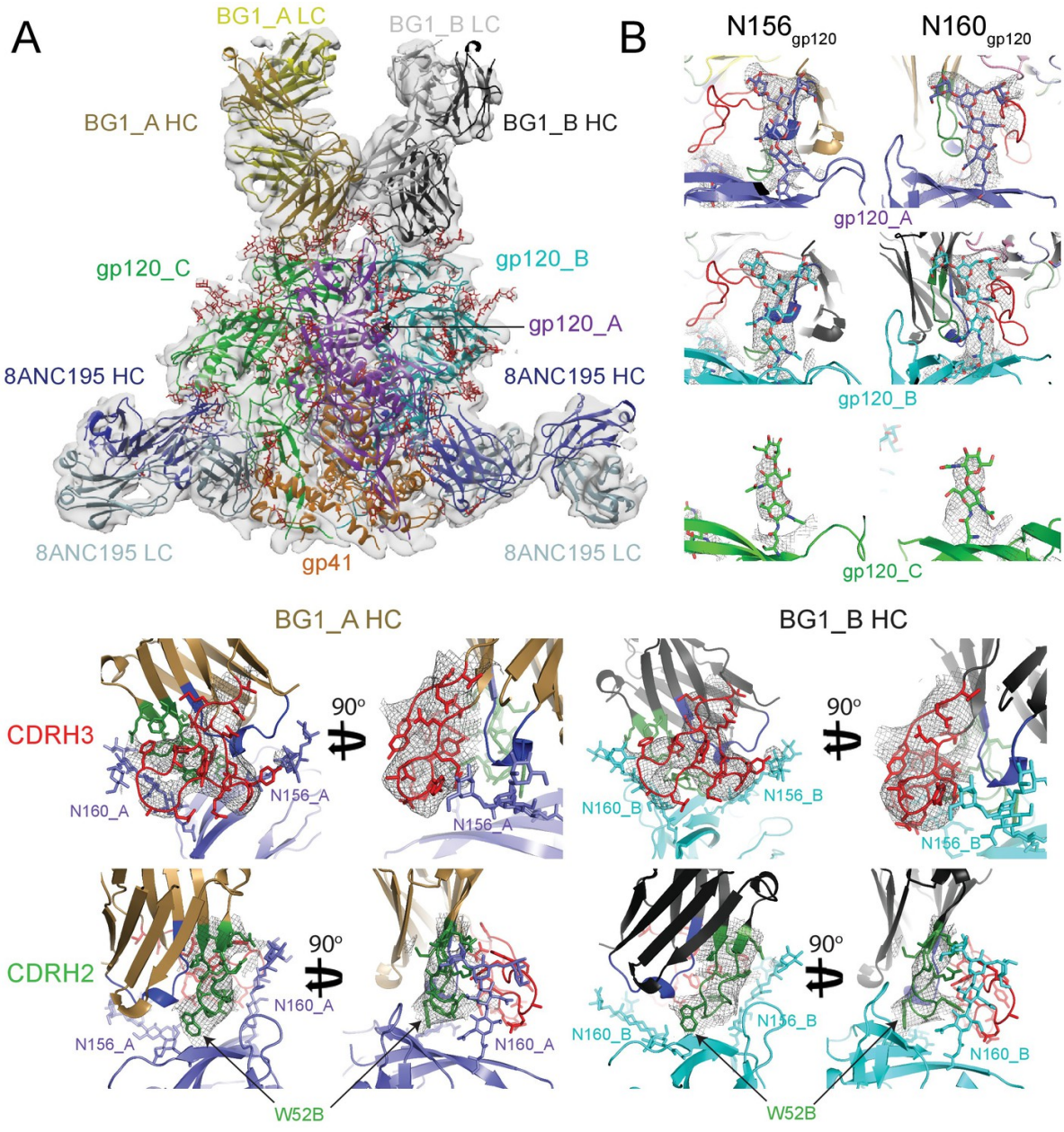

Figure 4.3. ~6.2 Å cryo-EM reconstruction of a BG1-Env-8ANC195 complex.

(A) EM density fit by coordinates for BG1_A (HC in brown; LC in yellow), BG1_B (HC in dark gray; LC in light gray), gp120s associated with BG1_A and BG1_B Fabs in purple and cyan, respectively; gp120_C in green, gp41 in orange, and 8ANC195 Fabs in dark blue (HC) and light

blue (LC). (B) Close-up views of densities contoured at 6.0σ (0.0378 e/Å^3) for glycans attached to Asn156$_{gp120}$ and Asn160$_{gp120}$ in the three gp120 protomers of Env trimer. Glycan residues built into the cryo-EM map densities are shown as sticks with oxygen atoms in red and nitrogen atoms in blue. (C, D) Close-up views of densities contoured at 6.0σ (0.0378 e/Å^3) surrounding CDRH3 (panel C) and CDRH2 (panel D) in BG1-gp120_A and BG1_B-gp120_B interactions. Asn156$_{gp120}$ and Asn160$_{gp120}$ glycans are shown as sticks. CDRH2 residue Trp54 (Figure 1D) is identified with an arrow.

Figure 4.4

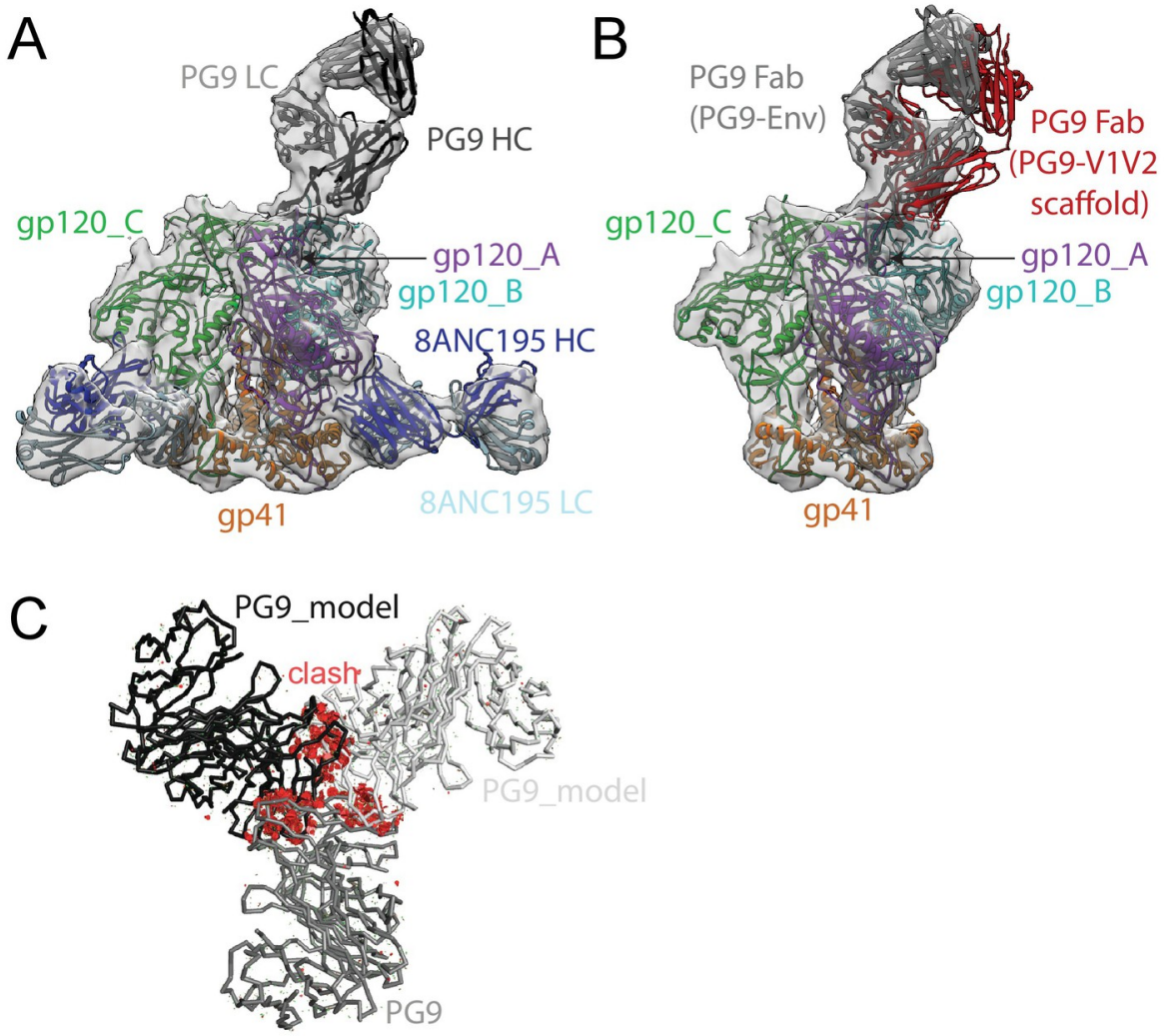

Figure 4.4. ~11.5 Å cryo-EM reconstruction of a PG9-Env-8ANC195 complex.

(A) EM density fit by coordinates for PG9 (HC in dark gray; LC in light gray), gp120 subunits in dark blue, cyan, and green, gp41 in orange, and 8ANC195 Fabs in dark blue (HC) and light blue (LC). (B) Density and coordinates from the PG9-Env portion of the PG9-Env-8ANC195 reconstruction (density for 8ANC195 Fabs removed) with coordinates for the PG9 Fab from the PG9-V1V2 scaffold structure (PDB 3U4E) superimposed. When the V1V2 scaffold from the PG9-V1V2 complex structure was superimposed with the V1V2 portion of the PG9-Env-8ANC195 structure (panel A), the angle of approach of the PG9 Fab differs from the angle observed in the

PG9-Env structure. (C) Hypothetical model of three PG9 Fabs bound per Env trimer. One PG9 Fab (PG9_A) is shown its experimentally-determined position from the PG9-Env-8ANC195 structure interacting mainly with gp120_A on Env trimer (view looking down the trimer three-fold axis). The V_H-V_L domains for second and third PG9 Fabs (PG9 model) were positioned onto the gp120_B and gp120_C subunits assuming the interaction observed for PG9_A with gp120_A. Predicted van der Waals clashes (red dots) were calculated using the show_bumps module in Pymol (Schrödinger, 2011).

Figure 4.5

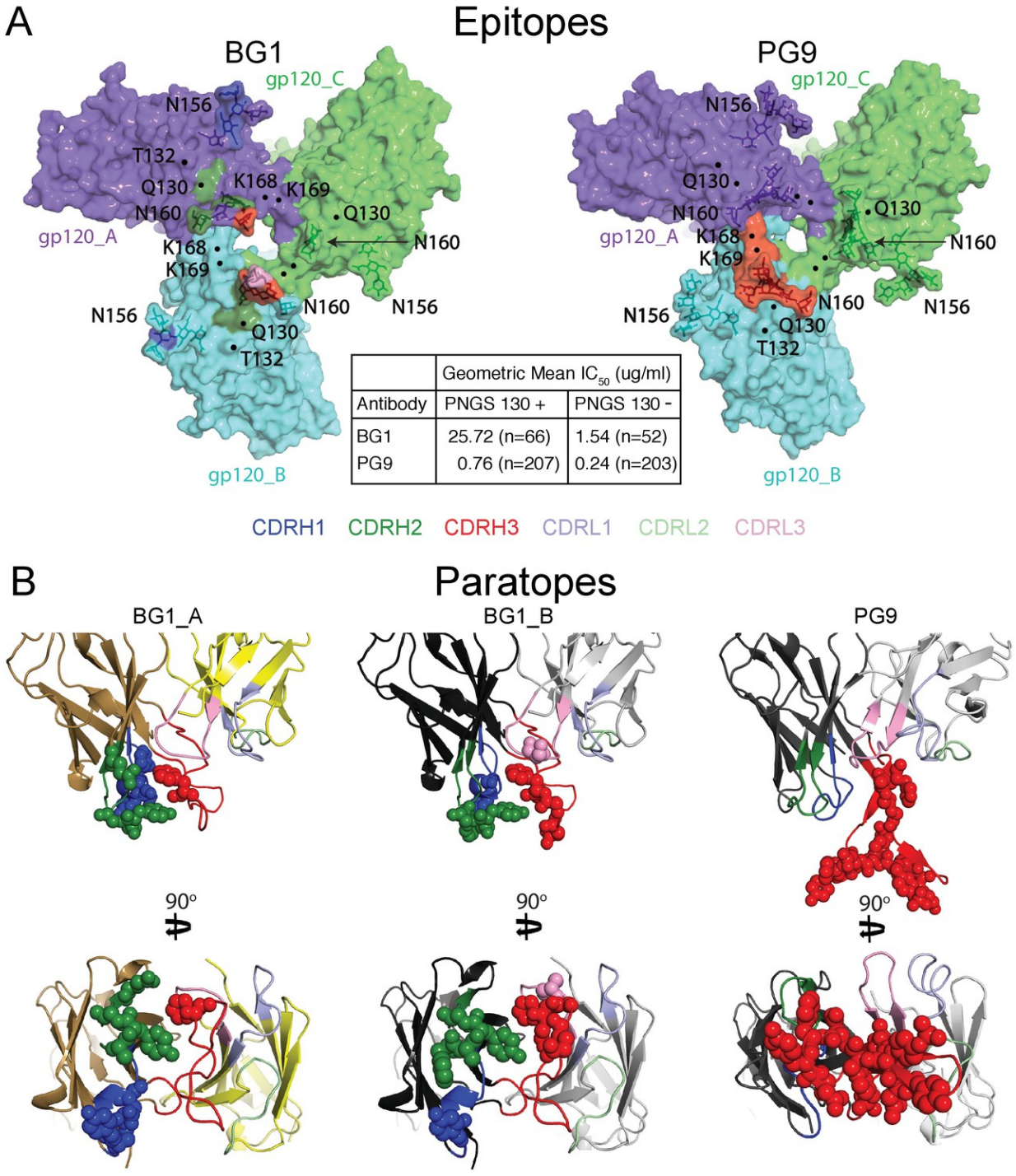

	Geometric Mean IC_{50} (ug/ml)	
Antibody	PNGS 130 +	PNGS 130 -
BG1	25.72 (n=66)	1.54 (n=52)
PG9	0.76 (n=207)	0.24 (n=203)

Figure 4.5. Comparison of BG1 and PG9 epitopes and paratopes.

(A) Epitopes on Env trimer (top view surface representations) were defined as protein or glycan residues whose Ca (for protein) or C1 (for glycans) atom was within 7 Å of the bound Fab. Contacts on Env are color-coded to indicate which CDR loop made the contact (CDRH3 in red, CDRH2 in green, and CDRH1 in dark blue). Glycans are shown as sticks with a nearby label to identify the glycan as attached to either $Asn156_{gp120}$ or $Asn160_{gp120}$, and locations of residues of interest ($Lys168_{gp120}$, $Lys169_{gp120}$, and $Gln130_{gp120}$) are indicated by black dots. Center box compares geometric mean IC_{50} values for BG1 and PG9 IgGs evaluated against HIV-1 strains either containing or not containing a PNGS at position 130 (number of HIV-1 strains indicated in the parentheses). IC_{50} values >50 μg/mL set to 50 μg/mL for geometric mean calculations. (B) Paratopes on BG1_A, BG1_B, and PG9 Fabs indicated by spheres on ribbon representations of V_H-V_L domains shown in two orientations related by a 90˚ rotation. CDRs are color coded as in panel A.

Figure 4.6

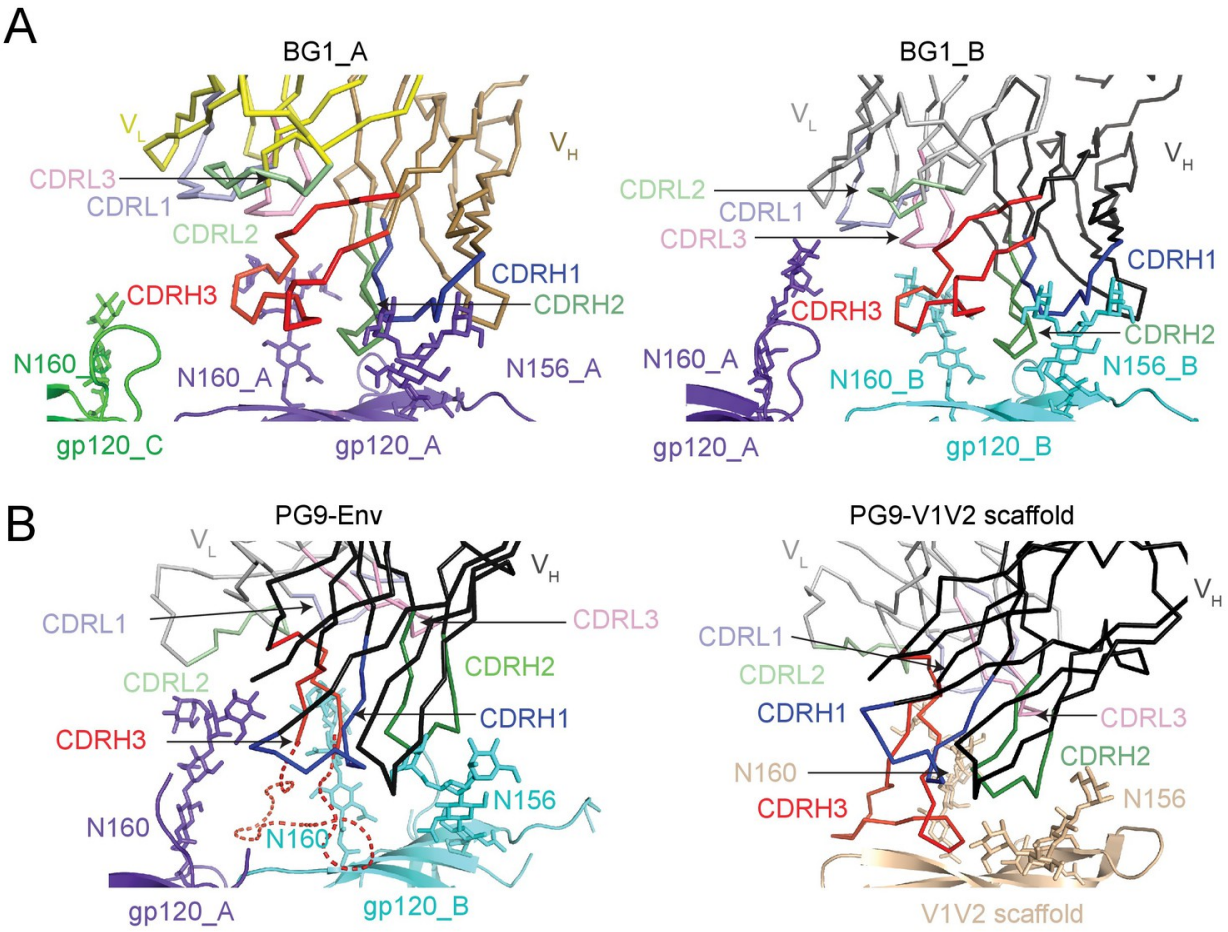

Figure 4.6. BG1 and PG9 interactions with V1V2.

(A) BG1 interactions with N-linked glycans attached to $Asn156_{gp120}$ and $Asn160_{gp120}$ shown for BG1_A (left) and BG1_B (right). (B) PG9 interactions with N-linked glycans attached to $Asn156_{gp120}$ and $Asn160_{gp120}$ from PG9-Env cryo-EM structure reported here (left) and from the crystal structure of PG9-V1V2 scaffold (PDB 3U4E) (right). The position of the CDRH3 loop in the PG9-Env cryo-EM structure is shown by a dashed line representing the position of CDRH3 in the PG9-V1V2 scaffold structure.

Figure 4.7

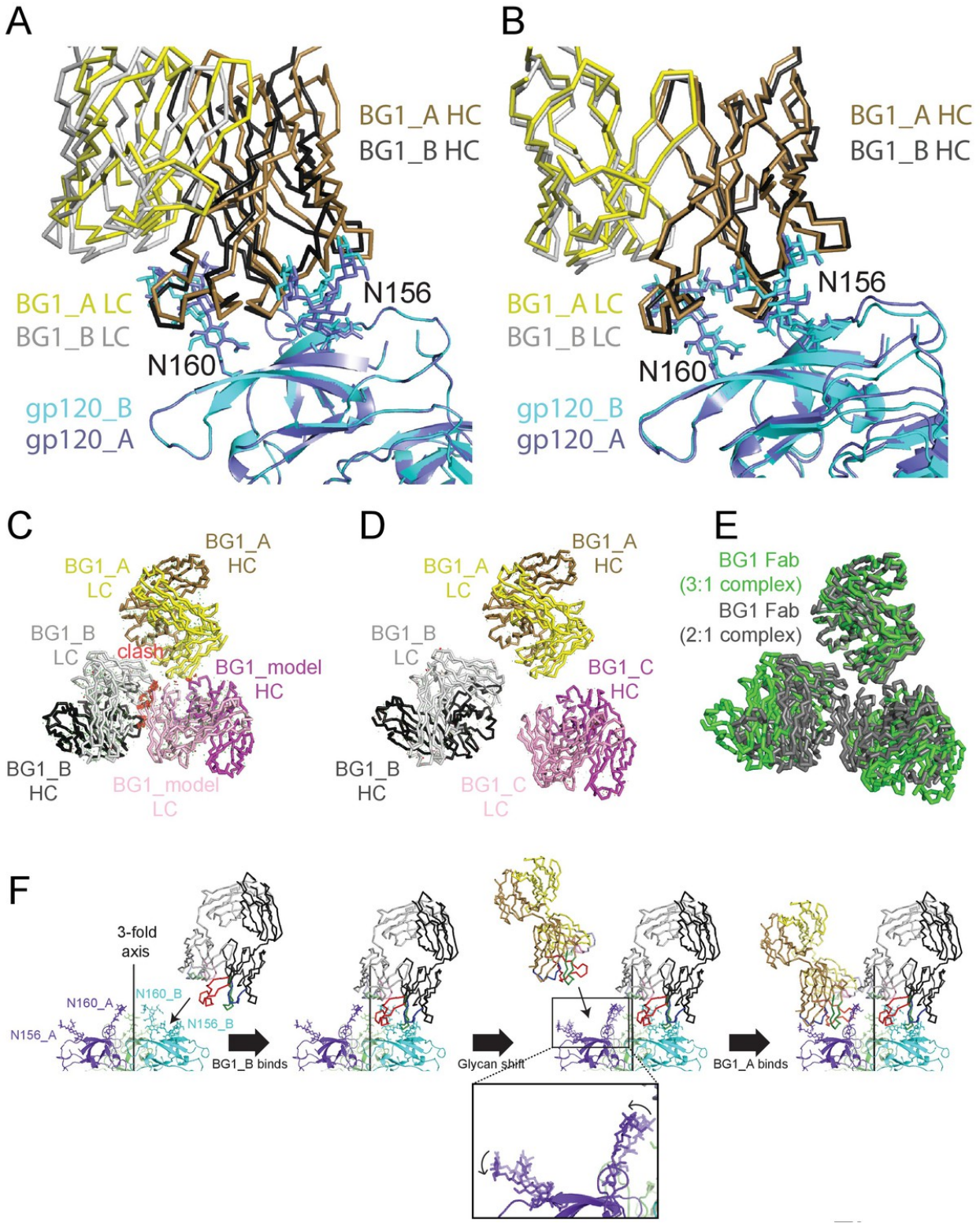
A
BG1_A HC
BG1_B HC
BG1_A LC
BG1_B LC
N156
N160
gp120_B
gp120_A
B
BG1_A HC
BG1_B HC
BG1_A LC
BG1_B LC
N156
N160
gp120_B
gp120_A
C
BG1_A HC
BG1_A LC
BG1_B LC
clash
BG1_model HC
BG1_B HC
BG1_model LC
D
BG1_A HC
BG1_A LC
BG1_B LC
BG1_C HC
BG1_B HC
BG1_C LC
E
BG1 Fab (3:1 complex)
BG1 Fab (2:1 complex)
F
3-fold axis
N160_A
N160_B
N156_A
N156_B
BG1_B binds
Glycan shift
BG1_A binds

Figure 4.7. Asymmetry of BG1 interactions with Env trimer.

(A,B) Superposition of the two BG1 binding sites in the 2:1 BG1-Env structure by aligning either the V1V2 regions of gp120_A and gp120_B (panel A) or the $Asn156_{gp120}$ and $Asn160_{gp120}$ glycans within gp120_A and gp120_B (panel B). (C) Hypothetical model of three BG1 Fabs bound per Env trimer based on Fab orientations in the 2:1 BG1-Env structure. The BG1_A and BG_1 B Fabs are shown in their respective positions on the gp120_A and gp120_B subunits of Env trimer (view looking down the trimer three-fold axis). A third BG1 Fab (BG1 model) was positioned onto the gp120_C subunit assuming that it would interact with the $Asn156_{gp120}$ and $Asn160_{gp120}$ glycans in the common interaction observed for BG1_A and BG1_B (panel B). Predicted van der Waals clashes (red dots) were calculated using the show_bumps module in Pymol (Schrödinger, 2011). (D) Positions of three BG1 Fabs in the 27 Å 3:1 BG1-Env structure (no predicted van der Waals clashes). (E) Comparison of BG1 Fab positions in the 2:1 BG1-Env structure (gray; the third Fab is from the model shown in panel C) and the 3:1 BG1-Env structure (green) after superimposing the BG1_A Fabs. (F) Model for binding of two BG1 Fabs to form the 2:1 BG1-Env structure. Panels 1 and 2: BG1_B binds first to the V1V2 epitope on gp120_B such that its CDRL1 interacts with the $Asn160_{gp120}$ glycan from gp120_A. Panels 3 and 4: BG1_A recognizes the $Asn156_{gp120}$ and $Asn160_{gp120}$ glycans from gp120_A. The flexible glycans are shifted away from the trimer 3-fold axis (indicated by arrows in the close-up view of the third panel) such that a potential clash with BG1_B is avoided.

Tables

Table 4.1

	BG1 Fab
Data collection	
Beamline	SSRL 12-2
Wavelength	0.9795 Å
Temperature (°K)	100
Space group	$P3_221$
Cell dimensions	
a, *b*, *c* (Å)	95.6, 95.6, 103.9
a, b, g (°)	90, 90, 120
Resolution (Å)	82.82-2.00 (2.05-2.00)*
R_{merge}	.11 (.98)
R_{pim}	.07 (.72)
I / sI	7.9 (1.6)
CC (1/2)	.99 (.63)
Completeness (%)	100 (100)
Redundancy	5.5 (5.5)
Refinement	
Resolution (Å)	38.5-2.0 (2.05-2.00)
No. reflections	43,296
R_{free} Reflections	4,169
R_{work} / R_{free}	0.189/0.212
No. atoms	
Protein	3,257
Ligand/ion	313
Water	
B-factors	
Protein	39.83
Ligand/ion	43.17
Average	40.12
R.m.s. deviations	
Bond lengths (Å)	0.011
Bond angles (°)	1.15

#Number of xtals used for each structure during data processing.

*Values in parentheses are for highest-resolution shell.

Table 4.1 BG1 Fab crystal structure data collection and refinement statistics.

Table 4.2

Data collection/processing	
Microscope	Titan Krios
Voltage	300kV
Camera	Gatan K2 Summit
Camera mode	counting
Defocus range	1.5-3.5
Exposure time	15 sec
Dosage rate	2.92 electrons·pixel^{-1}·subframe^{-1}
Magnified pixel size	1.35
Total Dose (e/A2)	80
Reconstruction	
Software	Relion-1.4
Symmetry	C1
Particles refined	
Resolution(automask, Å)	6.18
Resolution(masked out Fab CHCL domains, Å)	6.18
Map sharpening B-factor (Å2)	-24.7274
Model Statistics	
Map CC (whole unit cell):	0.931
Map CC (around atoms):	0.731
All-atom clashscore	17.66
Ramachandran plot:	
outliers:	0.44%
allowed:	7.44%
favored:	92.12%
rmsd (bonds):	0.01
rmsd (angles):	1.11
Rotamer outliers:	0.85%
C-beta deviations:	0

Table 4.2 BG1-Env-8ANC195 complex cryo-EM structure data collection and model statistics.

Supplementary Figures

Supplementary Figure 4.1

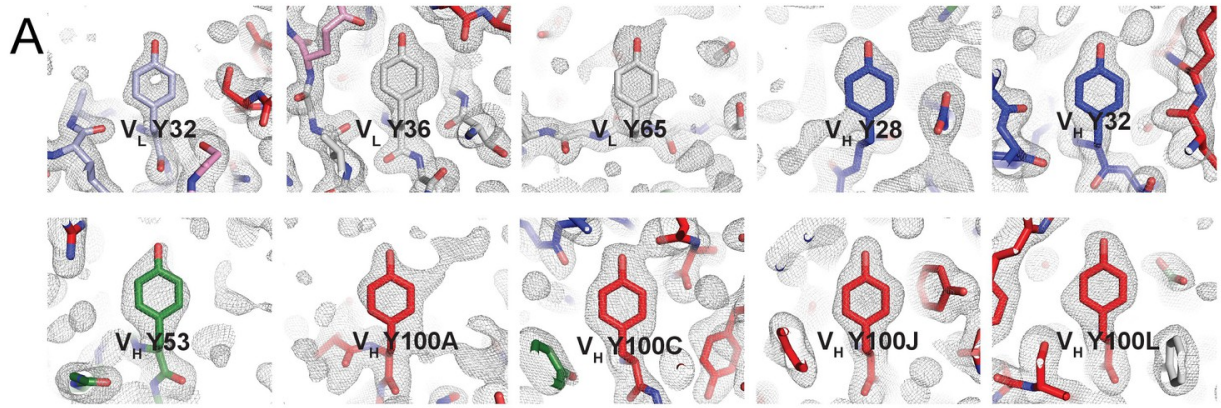

Supplementary Figure 4.1. Electron densities for tyrosines within BG1 Fab CDRs. (A) Tyrosine residues located within the antigen binding site are shown in stick representation together with their electron densities (contoured at 1.0σ) from a $2F_o$-F_c simulated annealing composite omit map.

Supplementary Figure 4.2

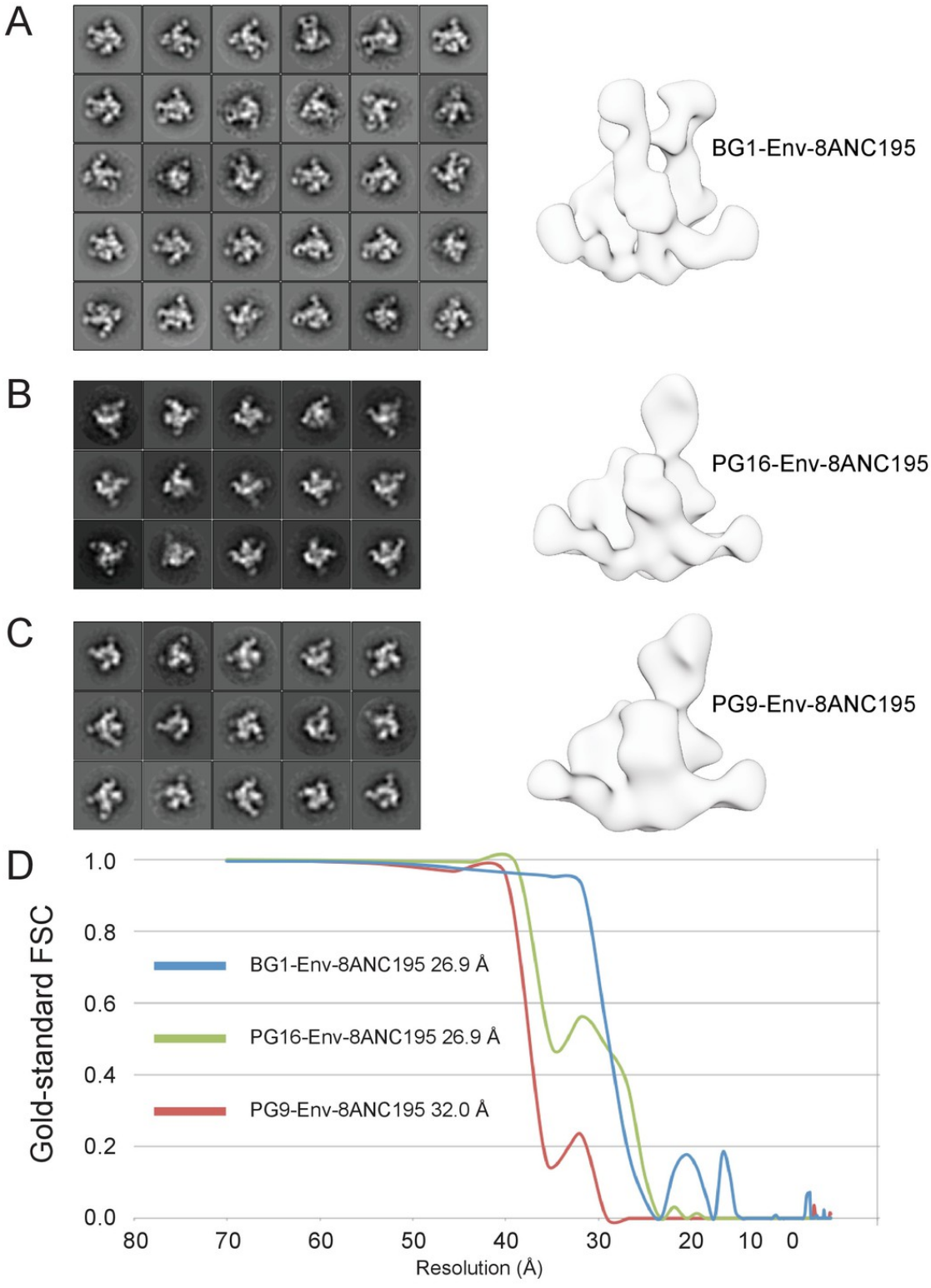

Supplementary Figure 4.2. Negative-stain EM structures of V1V2 bNAb-Env-8ANC195 complexes.

(A-C) 2D class averages and the final structures after refinement for BG1-Env-8ANC195 (panel A), PG16-Env-8ANC195 (panel B), and PG9-Env-8ANC195 (panel C). (D) Gold-standard FSC for each structure.

Supplementary Figure 4.3

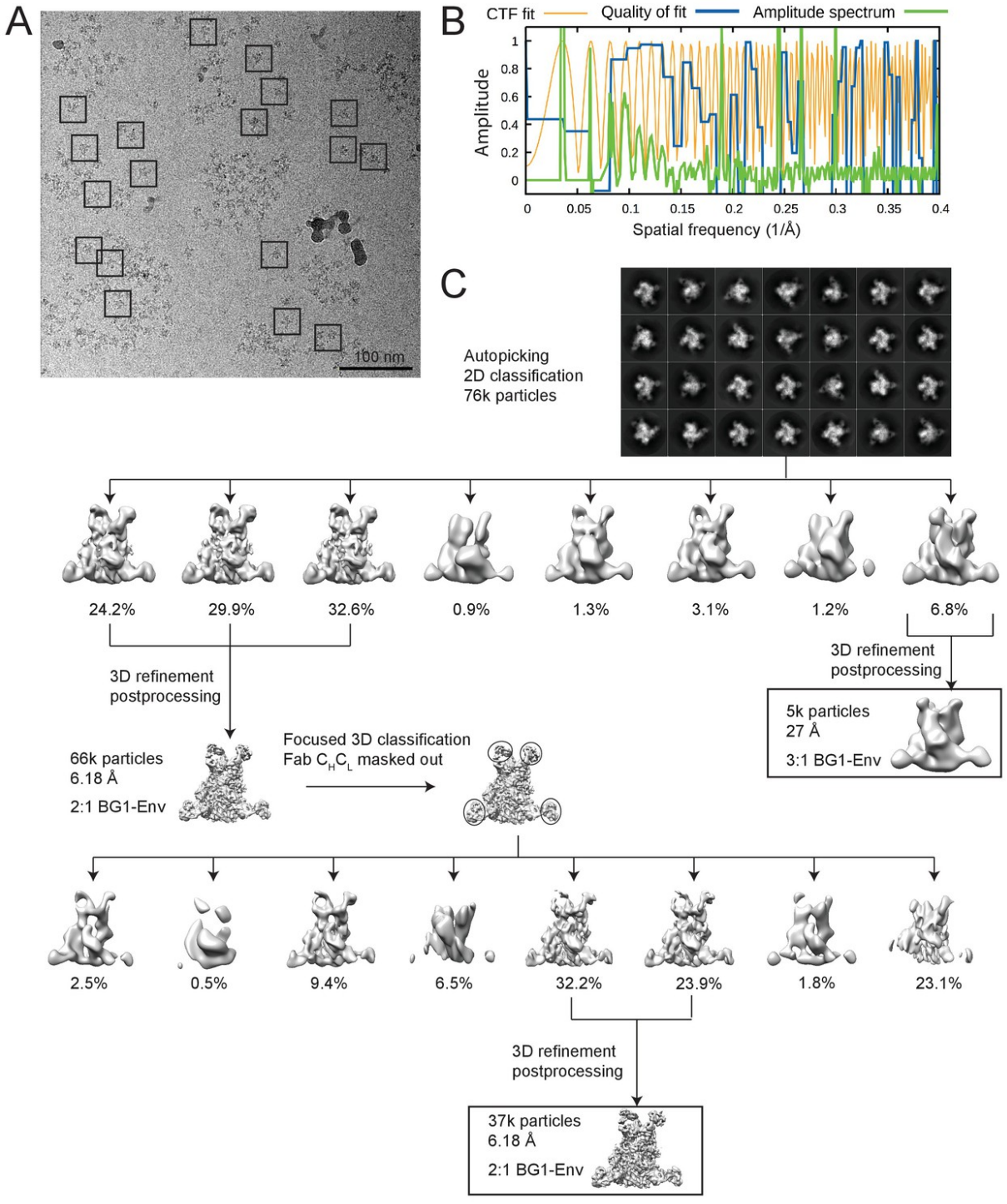

Supplementary Figure 4.3. Cryo-EM data processing for the BG1-Env-8ANC195 complex structure.

(A) Representative micrograph. Examples of complex particles are boxed. The accumulated dose and defocus values were ~80 e-/Å^2 and ~1.8 μm underfocus. (B) CTF fitting of the left micrograph (generated using CTFFIND4) shows a good fit to 4.9 Å. (C) Data processing scheme. 2D classification of autopicked particles resulted in 76K particles that were 3D classified using a low-pass-filtered negative-stain 2:1 BG1-Env EM structure as a reference model. The particles from the best three 3D classes were refined to 6.18 Å resolution. One 3D class showed three BG1 bound to each Env trimer (see Figure 3–figure supplement 2). The particles in 6.18 Å reconstruction were further 3D classified with the Fab C_HC_L domains masked out. Then the best two 3D classes were refined to 6.18 Å resolution. (E) Gold-standard FSCs of reconstructions generated using different strategies (see Figure 3–figure supplement 2). (F) Local resolution estimation. The complex is shown from top (left), side (middle), and bottom (right) views.

Supplementary Figure 4.4

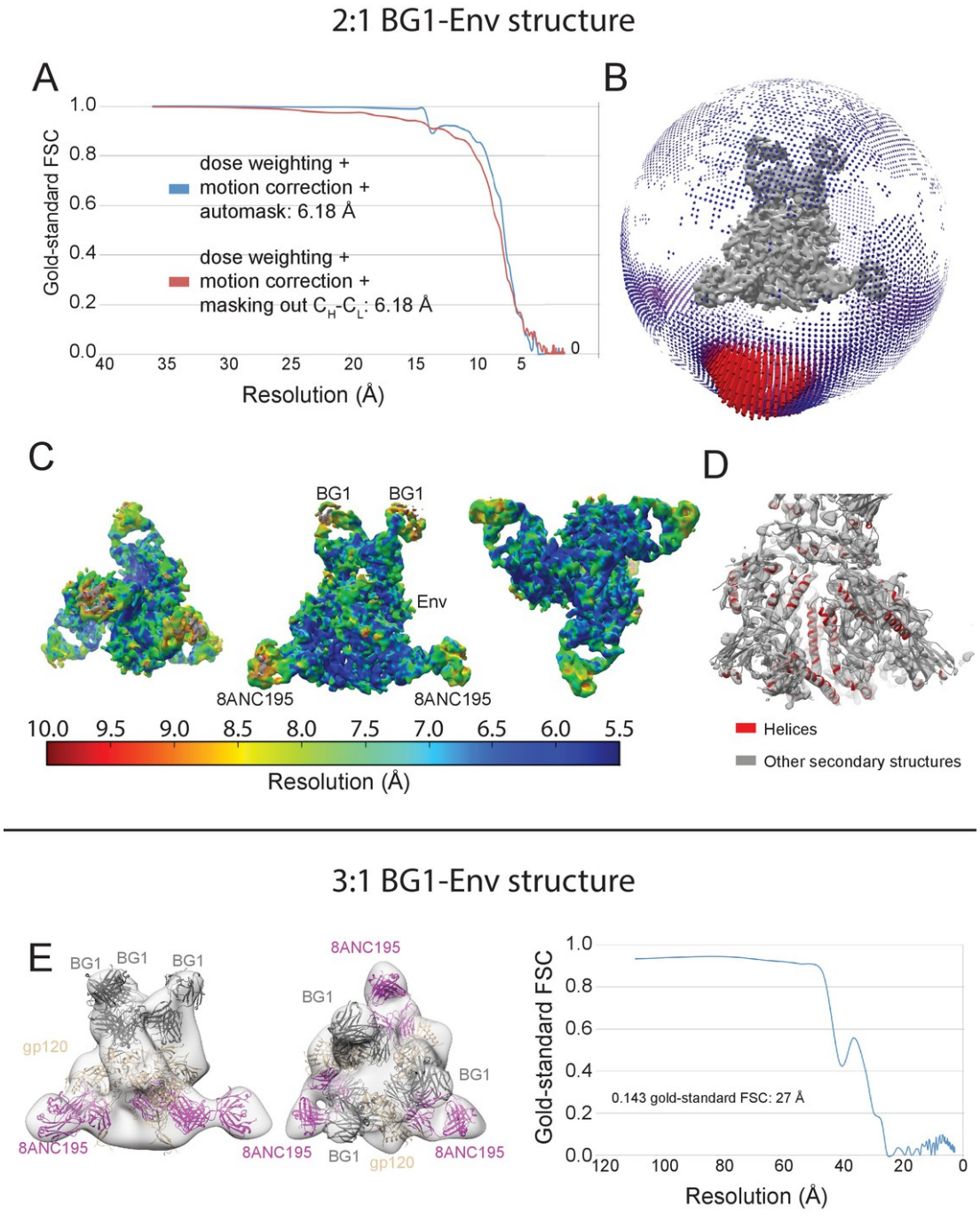

Supplementary Figure 4.4 Validation of the 2:1 and 3:1 BG1-Env structures.

(A) Gold-standard FSCs of 2:1 BG1-Env reconstructions generated using different strategies. (B) Orientation distribution of the 6.2 Å 2:1 BG1-Env reconstruction without masking out Fab C_HC_L domains. (C) Local resolution estimation for the 2:1 BG1-Env structure. The complex is shown from top (left), side (middle), and bottom (right) views. (D) Cryo-EM map contoured to show densities for a-helices (red); other secondary structures shown in grey. (E) 27 Å cryo-EM structure of a 3:1 BG1-Env complex. Cryo-EM map with fitted components are shown from side (left) and top (middle) views. Right: Gold-standard FSC indicating 27 Å resolution for the reconstruction.

Supplementary Figure 4.5

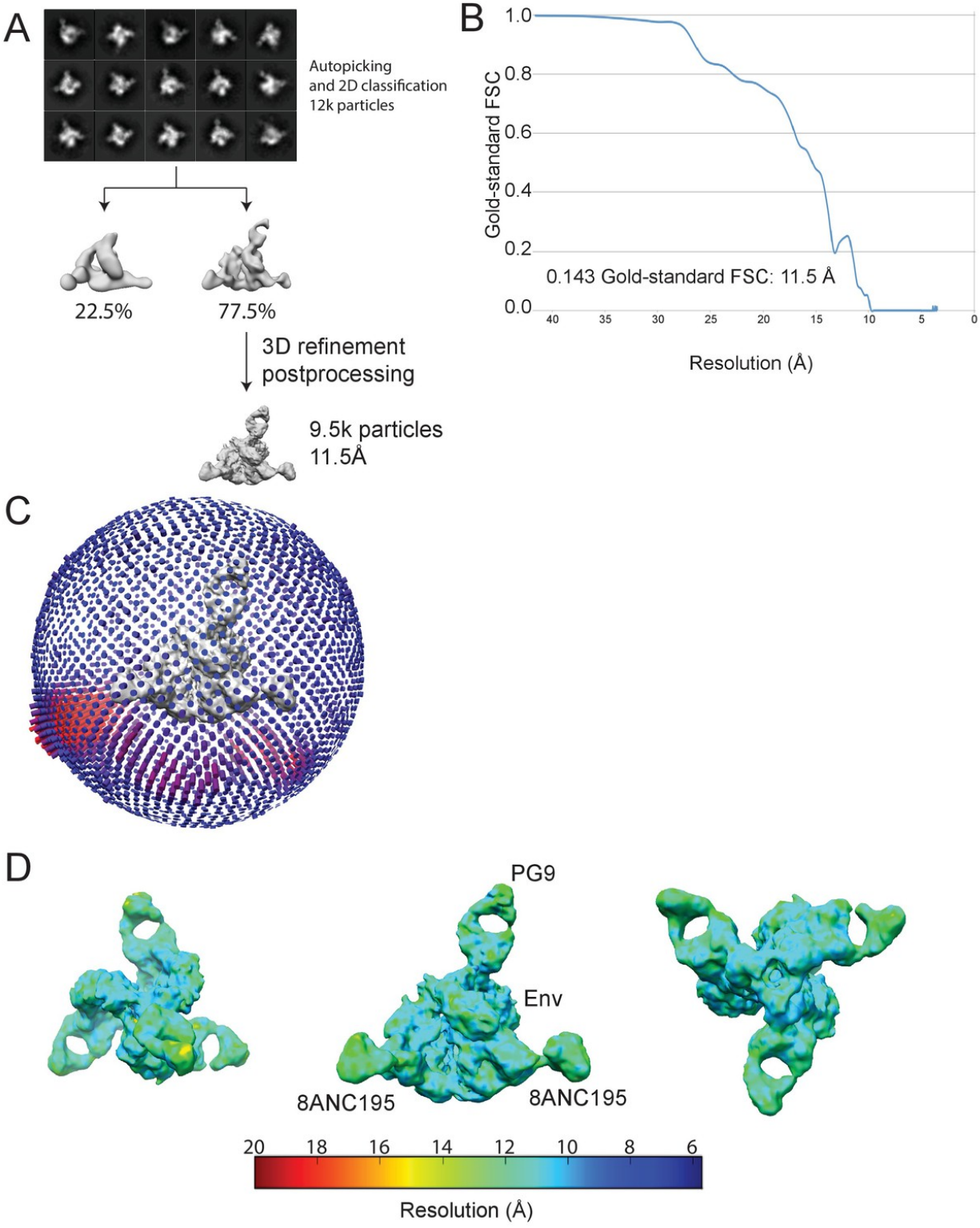

Supplementary Figure 4.5. Cryo-EM data processing for PG9-Env-8ANC195 complex structure.

(A) Data processing scheme. 2D classification of autopicked particles resulted in 12K particles that were 3D classified using a low-pass-filtered negative-stain PG9-Env-8ANC195 EM structure as a reference model. The particles from the best class were refined to 11.5 Å resolution. (B) Orientation distribution of the reconstruction. (C) Local resolution estimation. The complex is shown from top (left), side (middle), and bottom (right) views. (D) Gold-standard FSC indicating 11.5 Å resolution for the reconstruction.

Supplementary Figure 4.6

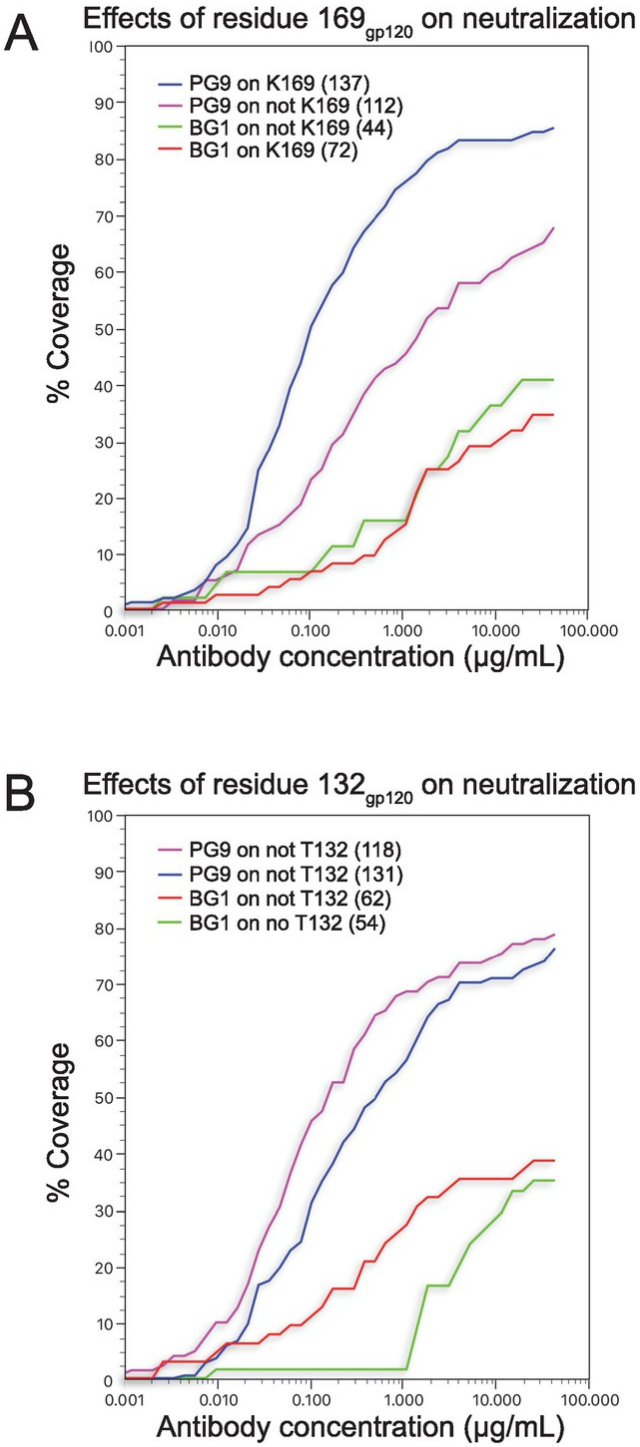

Supplementary Figure 4.6. Coverage curves for results of in vitro neutralization across panels of viruses that do or do not include a lysine at position 169_{gp120} (panel A) or a threonine at position 132_{gp120} (panel B). The number of strains used to calculate each curve is shown in parentheses in the key inside each graph.

Supplementary Tables

Supplementary Table 4.1

		BG1		
Virus	Clade	IgG	Fab	MNR
C1080.c03	CRF01_AE	0.02	0.3	16.0
WITO4160.33	B	0.03	0.2	9.0
191955_A11	A (T/F)	0.01	0.2	12.0
Q23.17	A	0.01	0.2	33.0
AC10.0.29	B	0.1	1.2	12.9
Ce1176_A3	C (T/F)	0.1	15.5	110.6
BG505/T332N	A	0.2	2.4	12.0
X1193_c1	G	1.7	8.5	4.9
CAP45.2.00.G3	C	0.6	3.8	6.1
6535.3	B	1.4	4.7	3.3
REJO4541.67	B	4.1	18.9	4.6
CNE5	CRF01_AE	2.7	15.9	6.0
62357_14_D3_4589	B (T/F)	12.0	55.8	4.7
CNE52	BC	8.2	53.6	6.5
3365.v2.c2	A	6.6	113.1	17.0
ZM249M.PL1	C	9.7	44.7	4.6
235-47	CRF02_AG	7.3	59.4	8.1
1394C9G1(Rev-)	C (T/F)	18.4	103.8	5.6
Ce704809221_1B3	C (T/F)	38.9	264.6	6.8
CNE20	BC	19.8	31.2	1.6
HIV-16055-2.3	C	39.7	351.5	8.9
Geometric mean		1.2	10.2	8.4
Geometric std. dev.				2.4

Supplementary Table 4.1. Neutralization potencies of Fab and IgG forms of BG1. Molar neutralization ratios (MNR) for BG1 was defined as IC_{50} Fab (nM)/IC_{50} IgG (nM).

Supplementary Table 4.2

		VRC01			PG9			PG16		
Virus	Clade	IgG	Fab	MNR	IgG	Fab	MNR	IgG	Fab	MNR
6535.3	B	6.9	40	5.8	4.1	170	41.5	285	1800	6.3
QH0692.42	B	7.5	14.0	1.9						
SC422661.8	B	0.62	2.3	3.7	20	220	11.0	120	850	7.1
PVO.4	B	4.4	10	2.3	80	500	6.3	89.5	260	2.9
TRO.11	B	2.4	12	5.0	240	1900	7.9	19.4	390	20.1
AC10.0.29	B	5.8	16	2.8	0.53	5.4	10.2	0.22	1.2	5.5
REJO4541.67	B	0.21	1.0	4.8	0.1	7.5	57.7	0.11	26	236.4
TRJO4551.58	B	0.62	1.6	2.6	3.9	200	51.3	25.5	240	9.4
WITO4160.33	B	0.41	2.3	5.6	0.33	0.42	1.3	0.095	0.51	5.4
CAAN5342.A2	B	5.8	16	2.8	80	240	3.0	140	590	4.2
THRO4156.18	B	36	70	1.9	270	1500	5.6	85.5	2000	23.4
RHPA4259.7	B	0.27	1.0	3.7	180	1500	8.3	3.4	53	15.6
Du156.12	C	0.62	1.2	1.9	0.33	2.8	8.5	0.16	0.67	4.2
Du172.17	C				3.3	9.30	2.8	0.41	2.6	6.3
Du422.1	C				2.9	7.1	2.4	0.95	28	29.5
ZM197M.PB7	C	4.3	6.9	1.6	6.7	13	1.9	8.1	73	9.0
ZM214M.PL15	C	1.7	8.4	4.9						
ZM233M.PB6	C	5.3	220	41.5	0.23	0.20	0.9	0.034	0.081	2.4
ZM249M.PL1	C	0.62	1.4	2.3	1.4	0.99	0.7	0.81	4.3	5.3
ZM53M.PB12	C	4.6	15	3.3	0.4	3.9	9.8	0.25	1.1	4.4
ZM109F.PB4	C	1.5	7.2	4.8	1.0	260	260.0			
ZM135M.PL10a	C	4.9	41	8.4						
CAP45.2.00.G3	C				0.020	0.12	6.0	0.027	0.061	2.3
CAP210.2.00.E8	C				3.1	6.2	2.0	0.47	14	29.8
Q23.17	A	0.41	4.3	10.5				0.014	0.20	14.3
Q842.d12	A	0.34	0.62	1.8	0.20	1.3	6.5	0.18	0.63	3.5
Q259.d2.17	A	0.69	110	159.4	1.5	0.99	0.7	0.068	19	279.4
3718.v3.c11	A	2.5	130	52.0	0.47	2.9	6.2	0.068	2.1	30.9
0330.v4.c3	A	0.41	1.2	2.9	0.13	0.97	7.5	0.14	0.69	4.9
3415.v1.c1	A	0.34	1	2.9	0.53	1.8	3.4	0.14	2.3	16.4
Geometric mean		1.6	7.4	4.8	2.2	13.3	6.0	1.0	10.5	10.3
Geometric std. dev.				3.1			4.1			3.4

Supplementary Table 4.2. Neutralization potencies of Fab and IgG forms of VRC01, PG9, and PG16. Molar neutralization ratios (MNR) was defined as IC_{50} Fab (nM)/IC_{50} IgG (nM).

Supplementary Table 4.3

Virus	Clade	3BNC60-62bp-3BNC60	3BNC60 Fab	MNR	3BNC60 IgG	3BNC60 Fab	MNR
6535.3	B	0.24	27	112.5	4.0	27	6.8
SC422661.8	B	0.02	1.0	50.0	0.3	1.0	3.3
PVO.4	B	0.01	1.3	130.0	0.1	1.3	13.0
TRO.11	B	0.01	1.3	130.0	0.2	1.3	6.5
TRJO4551.58	B	0.03	4.8	160.0			
CAAN5342.A2	B	0.16	6.2	38.8	3.6	6.2	1.7
THRO4156.18	B	0.43	23	53.5	3.5	23	6.6
RHPA4259.7	B	0.007	1.5	214.3	0.3	1.5	5.0
Du156.12	C	0.03	9.4	313.3	0.3	9.4	31.3
Du172.17	C	1	210	210.0	16	210	13.1
ZM197M.PB7	C	0.11	15	136.4	3.8	15	3.9
ZM214M.PL15	C	0.07	6.9	98.6	1.7	6.9	4.1
ZM233M.PB6	C	0.08	14	175.0	1.4	14	10.0
ZM249M.PL1	C	0.01	2.7	270.0	0.3	2.7	9.0
ZM53M.PB12	C	0.11	5.2	47.3	1.3	5.2	4.0
ZM109F.PB4	C	0.05	39	780.0	0.3	39	130.0
ZM135M.PL10a	C	0.03	3.7	123.3	0.4	3.7	9.3
Q842.d12	A	0.001	0.21	210.0	0.09	0.21	2.3
Q259.d2.17	A	0.007	3.7	528.6	0.03	3.7	123.3
0330.v4.c3	A	0.007	0.62	88.6	0.2	0.62	3.1
3415.v1.c1	A	0.04	4.6	115.0	0.9	4.6	5.1
Geometric mean		0.04	5.06	141.44	0.63	5.07	8.08
Geometric std. dev.				2.1			3.2

Supplementary Table 4.3. Neutralization potencies of Fab and IgG forms of 3BNC60 and 3BNC60 based diFab.

Bibliography

Abela, I.A., Berlinger, L., Schanz, M., Reynell, L., Gunthard, H.F., Rusert, P., and Trkola, A. (2012). Cell-cell transmission enables HIV-1 to evade inhibition by potent CD4bs directed antibodies. PLoS Pathog *8*, e1002634.

Adams, P.D., Afonine, P.V., Bunkoczi, G., Chen, V.B., Davis, I.W., Echols, N., Headd, J.J., Hung, L.W., Kapral, G.J., Grosse-Kunstleve, R.W.*, et al.* (2010). PHENIX: a comprehensive Python-based system for macromolecular structure solution. Acta Crystallogr D Biol Crystallogr *66*, 213-221.

Afonine, P.V., Poon, B.K., Read, R.J., Sobolev, O.V., Terwilliger, T.C., Urzhumtsev, A., and Adams, P.D. (2018). Real-space refinement in Phenix for cryo-EM and crystallography. bioRxiv, 249607.

Agirre, J., Iglesias-Fernandez, J., Rovira, C., Davies, G.J., Wilson, K.S., and Cowtan, K.D. (2015). Privateer: software for the conformational validation of carbohydrate structures. Nat Struct Mol Biol *22*, 833-834.

Barouch, D.H., Whitney, J.B., Moldt, B., Klein, F., Oliveira, T.Y., Liu, J., Stephenson, K.E., Chang, H.W., Shekhar, K., Gupta, S.*, et al.* (2013). Therapeutic efficacy of potent neutralizing HIV-1-specific monoclonal antibodies in SHIV-infected rhesus monkeys. Nature *503*, 224-228.

Barre-Sinoussi, F., Ross, A.L., and Delfraissy, J.F. (2013). Past, present and future: 30 years of HIV research. Nat Rev Microbiol *11*, 877-883.

Blattner, C., Lee, J.H., Sliepen, K., Derking, R., Falkowska, E., de la Pena, A.T., Cupo, A., Julien, J.P., van Gils, M., Lee, P.S.*, et al.* (2014). Structural delineation of a quaternary, cleavage-dependent epitope at the gp41-gp120 interface on intact HIV-1 Env trimers. Immunity *40*, 669-680.

Bonsignori, M., Hwang, K.K., Chen, X., Tsao, C.Y., Morris, L., Gray, E., Marshall, D.J., Crump, J.A., Kapiga, S.H., Sam, N.E.*, et al.* (2011). Analysis of a clonal lineage of HIV-1 envelope V2/V3 conformational epitope-specific broadly neutralizing antibodies and their inferred unmutated common ancestors. J Virol *85*, 9998-10009.

Brilot, A.F., Chen, J.Z., Cheng, A., Pan, J., Harrison, S.C., Potter, C.S., Carragher, B., Henderson, R., and Grigorieff, N. (2012). Beam-induced motion of vitrified specimen on holey carbon film. J Struct Biol *177*, 630-637.

Burton, D.R., Ahmed, R., Barouch, D.H., Butera, S.T., Crotty, S., Godzik, A., Kaufmann, D.E., McElrath, M.J., Nussenzweig, M.C., and Pulendran, B. (2012). A blueprint for HIV vaccine discovery. Cell host & microbe *12*, 396-407.

Burton, D.R., and Mascola, J.R. (2015). Antibody responses to envelope glycoproteins in HIV-1 infection. Nat Immunol *16*, 571-576.

Burton, D.R., Pyati, J., Koduri, R., Sharp, S.J., Thornton, G.B., Parren, P.W., Sawyer, L.S., Hendry, R.M., Dunlop, N., Nara, P.L.*, et al.* (1994). Efficient neutralization of primary isolates of HIV-1 by a recombinant human monoclonal antibody. Science *266*, 1024-1027.

Campbell, M.G., Cheng, A., Brilot, A.F., Moeller, A., Lyumkis, D., Veesler, D., Pan, J., Harrison, S.C., Potter, C.S., Carragher, B.*, et al.* (2012). Movies of ice-embedded particles enhance resolution in electron cryo-microscopy. Structure *20*, 1823-1828.

Carr, C.M., and Kim, P.S. (1993). A spring-loaded mechanism for the conformational change of influenza hemagglutinin. Cell *73*, 823-832.

Caskey, M., Klein, F., Lorenzi, J.C., Seaman, M.S., West, A.P., Jr., Buckley, N., Kremer, G., Nogueira, L., Braunschweig, M., Scheid, J.F.*, et al.* (2015). Viraemia suppressed in HIV-1-infected humans by broadly neutralizing antibody 3BNC117. Nature *522*, 487-491.

Caskey, M., Schoofs, T., Gruell, H., Settler, A., Karagounis, T., Kreider, E.F., Murrell, B., Pfeifer, N., Nogueira, L., Oliveira, T.Y.*, et al.* (2017). Antibody 10-1074 suppresses viremia in HIV-1-infected individuals. Nat Med *23*, 185-191.

Chan, D.C., Fass, D., Berger, J.M., and Kim, P.S. (1997). Core structure of gp41 from the HIV envelope glycoprotein. Cell *89*, 263-273.

Chan, D.C., and Kim, P.S. (1998). HIV entry and its inhibition. Cell *93*, 681-684.

Chung, N.P., Matthews, K., Kim, H.J., Ketas, T.J., Golabek, M., de Los Reyes, K., Korzun, J., Yasmeen, A., Sanders, R.W., Klasse, P.J.*, et al.* (2014). Stable 293 T and CHO cell lines expressing cleaved, stable HIV-1 envelope glycoprotein trimers for structural and vaccine studies. Retrovirology *11*, 33.

Dall'Acqua, W., Goldman, E.R., Eisenstein, E., and Mariuzza, R.A. (1996). A mutational analysis of the binding of two different proteins to the same antibody. Biochem *35*, 9667-9676.

Diskin, R., Marcovecchio, P.M., and Bjorkman, P.J. (2010). Structure of a clade C HIV-1 gp120 bound to CD4 and CD4-induced antibody reveals anti-CD4 polyreactivity. Nat Struct Mol Biol *17*, 608-613.

Diskin, R., Scheid, J.F., Marcovecchio, P.M., West, A.P., Jr., Klein, F., Gao, H., Gnanapragasam, P.N., Abadir, A., Seaman, M.S., Nussenzweig, M.C.*, et al.* (2011). Increasing the potency and breadth of an HIV antibody by using structure-based rational design. Science *334*, 1289-1293.

Doria-Rose, N.A., Schramm, C.A., Gorman, J., Moore, P.L., Bhiman, J.N., DeKosky, B.J., Ernandes, M.J., Georgiev, I.S., Kim, H.J., Pancera, M.*, et al.* (2014). Developmental pathway for potent V1V2-directed HIV-neutralizing antibodies. Nature *509*, 55-62.

Emsley, P., and Cowtan, K. (2004). Coot: model-building tools for molecular graphics. Acta Crystallogr D Biol Crystallogr *60*, 2126-2132.

Endres, M.J., Clapham, P.R., Marsh, M., Ahuja, M., Turner, J.D., McKnight, A., Thomas, J.F., Stoebenau-Haggarty, B., Choe, S., and Vance, P.J. (1996). CD4-independent infection by HIV-2 is mediated by fusin/CXCR4. Cell *87*, 745-756.

Escolano, A., Dosenovic, P., and Nussenzweig, M.C. (2017). Progress toward active or passive HIV-1 vaccination. J Exp Med *214*, 3-16.

Freed, E.O. (2015). HIV-1 assembly, release and maturation. Nature Reviews Microbiology *13*, 484.

Freund, N.T., Wang, H., Scharf, L., Nogueira, L., Horwitz, J.A., Bar-On, Y., Golijanin, J., Sievers, S.A., Sok, D., Cai, H.*, et al.* (2017). Coexistence of potent HIV-1 broadly neutralizing antibodies and antibody-sensitive viruses in a viremic controller. Science translational medicine *9*.

Galimidi, R.P., Klein, J.S., Politzer, M.S., Bai, S., Seaman, M.S., Nussenzweig, M.C., West, A.P., Jr., and Bjorkman, P.J. (2015). Intra-spike crosslinking overcomes antibody evasion by HIV-1. Cell *160*, 433–446.

Garces, F., Lee, J.H., de Val, N., Torrents de la Pena, A., Kong, L., Puchades, C., Hua, Y., Stanfield, R.L., Burton, D.R., Moore, J.P.*, et al.* (2015). Affinity Maturation of a Potent Family of HIV Antibodies Is Primarily Focused on Accommodating or Avoiding Glycans. Immunity *43*, 1053-1063.

Goddard, T.D., Huang, C.C., and Ferrin, T.E. (2007). Visualizing density maps with UCSF Chimera. J Struct Biol *157*, 281-287.

Gorman, J., Soto, C., Yang, M.M., Davenport, T.M., Guttman, M., Bailer, R.T., Chambers, M., Chuang, G.Y., DeKosky, B.J., Doria-Rose, N.A.*, et al.* (2016). Structures of HIV-1 Env V1V2 with broadly neutralizing antibodies reveal commonalities that enable vaccine design. Nat Struct Mol Biol *23*, 81-90.

Grant, T., and Grigorieff, N. (2015). Measuring the optimal exposure for single particle cryo-EM using a 2.6 A reconstruction of rotavirus VP6. Elife *4*, e06980.

Gristick, H.B., von Boehmer, L., West, A.P., Jr., Schamber, M., Gazumyan, A., Golijanin, J., Seaman, M.S., Fatkenheuer, G., Klein, F., Nussenzweig, M.C.*, et al.* (2016). Natively glycosylated HIV-1 Env structure reveals new mode for antibody recognition of the CD4-binding site. Nat Struct Mol Biol *23*, 906-915.

Gristick, H.B., Wang, H., and Bjorkman, P.J. (2017). X-ray and EM structures of a natively glycosylated HIV-1 envelope trimer. Acta Crystallogr D Struct Biol *73*, 822-828.

Harris, A., Borgnia, M.J., Shi, D., Bartesaghi, A., He, H., Pejchal, R., Kang, Y.K., Depetris, R., Marozsan, A.J., Sanders, R.W., *et al.* (2011). Trimeric HIV-1 glycoprotein gp140 immunogens and native HIV-1 envelope glycoproteins display the same closed and open quaternary molecular architectures. Proc Natl Acad Sci U S A *108*, 11440-11445.

Harrison, S.C. (2015). Viral membrane fusion. Virology *479-480*, 498-507.

Haynes, B.F., Fleming, J., St Clair, E.W., Katinger, H., Stiegler, G., Kunert, R., Robinson, J., Scearce, R.M., Plonk, K., Staats, H.F., *et al.* (2005). Cardiolipin polyspecific autoreactivity in two broadly neutralizing HIV-1 antibodies. Science *308*, 1906-1908.

Hoffman, T.L., LaBranche, C.C., Zhang, W., Canziani, G., Robinson, J., Chaiken, I., Hoxie, J.A., and Doms, R.W. (1999). Stable exposure of the coreceptor-binding site in a CD4-independent HIV-1 envelope protein. Proceedings of the National Academy of Sciences *96*, 6359-6364.

Horwitz, J.A., Halper-Stromberg, A., Mouquet, H., Gitlin, A.D., Tretiakova, A., Eisenreich, T.R., Malbec, M., Gravemann, S., Billerbeck, E., Dorner, M., *et al.* (2013). HIV-1 suppression and durable control by combining single broadly neutralizing antibodies and antiretroviral drugs in humanized mice. Proc Natl Acad Sci U S A *110*, 16538-16543.

Huang, C.C., Lam, S.N., Acharya, P., Tang, M., Xiang, S.H., Hussan, S.S., Stanfield, R.L., Robinson, J., Sodroski, J., Wilson, I.A., *et al.* (2007). Structures of the CCR5 N terminus and of a tyrosine-sulfated antibody with HIV-1 gp120 and CD4. Science *317*, 1930-1934.

Huang, J., Kang, B.H., Pancera, M., Lee, J.H., Tong, T., Feng, Y., Imamichi, H., Georgiev, I.S., Chuang, G.Y., Druz, A., *et al.* (2014). Broad and potent HIV-1 neutralization by a human antibody that binds the gp41-gp120 interface. Nature *515*, 138-142.

Julien, J.P., Cupo, A., Sok, D., Stanfield, R.L., Lyumkis, D., Deller, M.C., Klasse, P.J., Burton, D.R., Sanders, R.W., Moore, J.P., *et al.* (2013a). Crystal structure of a soluble cleaved HIV-1 envelope trimer. Science *342*, 1477-1483.

Julien, J.P., Lee, J.H., Cupo, A., Murin, C.D., Derking, R., Hoffenberg, S., Caulfield, M.J., King, C.R., Marozsan, A.J., Klasse, P.J., *et al.* (2013b). Asymmetric recognition of the HIV-1 trimer by broadly neutralizing antibody PG9. Proc Natl Acad Sci U S A *110*, 4351-4356.

Kabsch, W. (2010). XDS. Acta Crystallogr D Biol Crystallogr *66*, 125-132.

Kanki, P.J., Travers, K.U., Marlink, R., Essex, M., MBoup, S., Gueye-NDiaye, A., Siby, T., Thior, I., Sankale, J., and Hsieh, C. (1994). Slower heterosexual spread of HIV-2 than HIV-1. The Lancet *343*, 943-946.

Kelley, R.F., and O'Connell, M.P. (1993). Thermodynamic analysis of an antibody functional epitope. Biochem *32*, 6828-6835.

Kimanius, D., Forsberg, B.O., Scheres, S.H., and Lindahl, E. (2016). Accelerated cryo-EM structure determination with parallelisation using GPUs in RELION-2. Elife *5*.

Klein, F., Diskin, R., Scheid, J.F., Gaebler, C., Mouquet, H., Georgiev, I.S., Pancera, M., Zhou, T., Incesu, R.B., Fu, B.Z*., et al.* (2013a). Somatic mutations of the immunoglobulin framework are generally required for broad and potent HIV-1 neutralization. Cell *153*, 126-138.

Klein, F., Gaebler, C., Mouquet, H., Sather, D.N., Lehmann, C., Scheid, J.F., Kraft, Z., Liu, Y., Pietzsch, J., and Hurley, A. (2012a). Broad neutralization by a combination of antibodies recognizing the CD4 binding site and a new conformational epitope on the HIV-1 envelope protein. Journal of Experimental Medicine *209*, 1469-1479.

Klein, F., Halper-Stromberg, A., Horwitz, J.A., Gruell, H., Scheid, J.F., Bournazos, S., Mouquet, H., Spatz, L.A., Diskin, R., Abadir, A*., et al.* (2012b). HIV therapy by a combination of broadly neutralizing antibodies in humanized mice. Nature *492*, 118-122.

Klein, F., Mouquet, H., Dosenovic, P., Scheid, J.F., Scharf, L., and Nussenzweig, M.C. (2013b). Antibodies in HIV-1 vaccine development and therapy. Science *341*, 1199-1204.

Klein, J.S., and Bjorkman, P.J. (2010). Few and far between: how HIV may be evading antibody avidity. PLoS Pathog *6*, e1000908.

Kong, L., Torrents de la Pena, A., Deller, M.C., Garces, F., Sliepen, K., Hua, Y., Stanfield, R.L., Sanders, R.W., and Wilson, I.A. (2015). Complete epitopes for vaccine design derived from a crystal structure of the broadly neutralizing antibodies PGT128 and 8ANC195 in complex with an HIV-1 Env trimer. Acta Crystallogr D Biol Crystallogr *71*, 2099-2108.

Kong, R., Xu, K., Zhou, T., Acharya, P., Lemmin, T., Liu, K., Ozorowski, G., Soto, C., Taft, J.D., and Bailer, R.T. (2016). Fusion peptide of HIV-1 as a site of vulnerability to neutralizing antibody. Science *352*, 828-833.

Kremer, J.R., Mastronarde, D.N., and McIntosh, J.R. (1996). Computer visualization of three-dimensional image data using IMOD. J Struct Biol *116*, 71-76.

Kucukelbir, A., Sigworth, F.J., and Tagare, H.D. (2014). Quantifying the local resolution of cryo-EM density maps. Nat Methods *11*, 63-65.

Kwon, Y.D., Finzi, A., Wu, X., Dogo-Isonagie, C., Lee, L.K., Moore, L.R., Schmidt, S.D., Stuckey, J., Yang, Y., Zhou, T*., et al.* (2012). Unliganded HIV-1 gp120 core structures assume the CD4-bound conformation with regulation by quaternary interactions and variable loops. Proc Natl Acad Sci U S A *109*, 5663-5668.

Kwon, Y.D., Pancera, M., Acharya, P., Georgiev, I.S., Crooks, E.T., Gorman, J., Joyce, M.G., Guttman, M., Ma, X., Narpala, S*., et al.* (2015). Crystal structure, conformational fixation and entry-related interactions of mature ligand-free HIV-1 Env. Nat Struct Mol Biol *22*, 522-531.

Kwong, P.D., Doyle, M.L., Casper, D.J., Cicala, C., Leavitt, S.A., Majeed, S., Steenbeke, T.D., Venturi, M., Chaiken, I., and Fung, M. (2002). HIV-1 evades antibody-mediated neutralization through conformational masking of receptor-binding sites. Nature *420*, 678.

Kwong, P.D., and Mascola, J.R. (2012). Human antibodies that neutralize HIV-1: identification, structures, and B cell ontogenies. Immunity *37*, 412-425.

Kwong, P.D., Wyatt, R., Robinson, J., Sweet, R.W., Sodroski, J., and Hendrickson, W.A. (1998). Structure of an HIV gp120 envelope glycoprotein in complex with the CD4 receptor and a neutralizing human antibody. Nature *393*, 648-659.

Landais, E., Huang, X., Havenar-Daughton, C., Murrell, B., Price, M.A., Wickramasinghe, L., Ramos, A., Bian, C.B., Simek, M., Allen, S.*, et al.* (2016). Broadly Neutralizing Antibody Responses in a Large Longitudinal Sub-Saharan HIV Primary Infection Cohort. PLoS Pathog *12*, e1005369.

Laskey, S.B., and Siliciano, R.F. (2014). A mechanistic theory to explain the efficacy of antiretroviral therapy. Nature Reviews Microbiology *12*, 772.

Lee, J.H., Andrabi, R., Su, C.Y., Yasmeen, A., Julien, J.P., Kong, L., Wu, N.C., McBride, R., Sok, D., Pauthner, M.*, et al.* (2017). A Broadly Neutralizing Antibody Targets the Dynamic HIV Envelope Trimer Apex via a Long, Rigidified, and Anionic beta-Hairpin Structure. Immunity *46*, 690-702.

Lee, J.H., Ozorowski, G., and Ward, A.B. (2016). Cryo-EM structure of a native, fully glycosylated, cleaved HIV-1 envelope trimer. Science *351*, 1043-1048.

Li, Z., Zhou, N., Sun, Y., Ray, N., Lataillade, M., Hanna, G.J., and Krystal, M. (2013). Activity of the HIV-1 attachment inhibitor BMS-626529, the active component of the prodrug BMS-663068, against CD4-independent viruses and HIV-1 envelopes resistant to other entry inhibitors. Antimicrobial agents and chemotherapy *57*, 4172-4180.

Liu, J., Bartesaghi, A., Borgnia, M.J., Sapiro, G., and Subramaniam, S. (2008). Molecular architecture of native HIV-1 gp120 trimers. Nature *455*, 109-113.

Liu, Q., Acharya, P., Dolan, M.A., Zhang, P., Guzzo, C., Lu, J., Kwon, A., Gururani, D., Miao, H., Bylund, T.*, et al.* (2017). Quaternary contact in the initial interaction of CD4 with the HIV-1 envelope trimer. Nat Struct Mol Biol *24*, 370-378.

Ludtke, S.J., Durmaz, T., Chen, M., and Bell, J.M. (2017). New Strategies for Improving CryoEM Single Particle Analysis in EMAN2.2. Microscopy and Microanalysis *23*, 810-811.

Lynch, R.M., Boritz, E., Coates, E.E., DeZure, A., Madden, P., Costner, P., Enama, M.E., Plummer, S., Holman, L., Hendel, C.S.*, et al.* (2015). Virologic effects of broadly neutralizing antibody VRC01 administration during chronic HIV-1 infection. Science translational medicine *7*, 319ra206.

Lyumkis, D., Julien, J.P., de Val, N., Cupo, A., Potter, C.S., Klasse, P.J., Burton, D.R., Sanders, R.W., Moore, J.P., Carragher, B.*, et al.* (2013). Cryo-EM structure of a fully glycosylated soluble cleaved HIV-1 envelope trimer. Science *342*, 1484-1490.

Ma, X., Lu, M., Gorman, J., Terry, D.S., Hong, X., Zhou, Z., Zhao, H., Altman, R.B., Arthos, J., Blanchard, S.C.*, et al.* (2018). HIV-1 Env trimer opens through an asymmetric intermediate in which individual protomers adopt distinct conformations. Elife *7*.

Mastronarde, D.N. (2005). Automated electron microscope tomography using robust prediction of specimen movements. J Struct Biol *152*, 36-51.

McCoy, L.E., and Burton, D.R. (2017). Identification and specificity of broadly neutralizing antibodies against HIV. Immunol Rev *275*, 11-20.

McCoy, L.E., and Weiss, R.A. (2013). Neutralizing antibodies to HIV-1 induced by immunization. Journal of Experimental Medicine *210*, 209-223.

McLellan, J.S., Pancera, M., Carrico, C., Gorman, J., Julien, J.P., Khayat, R., Louder, R., Pejchal, R., Sastry, M., Dai, K.*, et al.* (2011). Structure of HIV-1 gp120 V1/V2 domain with broadly neutralizing antibody PG9. Nature *480*, 336-343.

Meffre, E., Milili, M., Blanco-Betancourt, C., Antunes, H., Nussenzweig, M.C., and Schiff, C. (2001). Immunoglobulin heavy chain expression shapes the B cell receptor repertoire in human B cell development. The Journal of clinical investigation *108*, 879-886.

Merk, A., and Subramaniam, S. (2013). HIV-1 envelope glycoprotein structure. Curr Opin Struct Biol *23*, 268-276.

Montefiori, D.C. (2005). Evaluating neutralizing antibodies against HIV, SIV, and SHIV in luciferase reporter gene assays. Current protocols in immunology / edited by John E Coligan [et al *Chapter 12*, Unit 12 11.

Moore, J.P., McKeating, J.A., Weiss, R.A., and Sattentau, Q.J. (1990). Dissociation of gp120 from HIV-1 virions induced by soluble CD4. Science *250*, 1139-1142.

Mouquet, H., Scheid, J.F., Zoller, M.J., Krogsgaard, M., Ott, R.G., Shukair, S., Artyomov, M.N., Pietzsch, J., Connors, M., Pereyra, F.*, et al.* (2010). Polyreactivity increases the apparent affinity of anti-HIV antibodies by heteroligation. Nature *467*, 591-595.

Munro, J.B., Gorman, J., Ma, X., Zhou, Z., Arthos, J., Burton, D.R., Koff, W.C., Courter, J.R., Smith, A.B., 3rd, Kwong, P.D.*, et al.* (2014). Conformational dynamics of single HIV-1 envelope trimers on the surface of native virions. Science *346*, 759-763.

Munro, J.B., and Lee, K.K. (2018). Probing Structural Variation and Dynamics in the HIV-1 Env Fusion Glycoprotein. Curr HIV Res *16*, 5-12.

Munro, J.B., and Mothes, W. (2015). Structure and Dynamics of the Native HIV-1 Env Trimer. J Virol *89*, 5752-5755.

Murphy, K.M., and Reiner, S.L. (2002). Decision making in the immune system: the lineage decisions of helper T cells. Nature Reviews Immunology *2*, 933.

Naydenova, K., and Russo, C.J. (2017). Measuring the effects of particle orientation to improve the efficiency of electron cryomicroscopy. Nat Commun *8*, 629.

Nicastro, D., Schwartz, C., Pierson, J., Gaudette, R., Porter, M.E., and McIntosh, J.R. (2006). The molecular architecture of axonemes revealed by cryoelectron tomography. Science *313*, 944-948.

Ozorowski, G., Pallesen, J., de Val, N., Lyumkis, D., Cottrell, C.A., Torres, J.L., Copps, J., Stanfield, R.L., Cupo, A., Pugach, P.*, et al.* (2017). Open and closed structures reveal allostery and pliability in the HIV-1 envelope spike. Nature *547*, 360-363.

Pan, R., Gorny, M.K., Zolla-Pazner, S., and Kong, X.P. (2015). The V1V2 Region of HIV-1 gp120 Forms a Five-Stranded Beta Barrel. J Virol *89*, 8003-8010.

Pancera, M., Changela, A., and Kwong, P.D. (2017). How HIV-1 entry mechanism and broadly neutralizing antibodies guide structure-based vaccine design. Curr Opin HIV AIDS *12*, 229-240.

Pancera, M., McLellan, J.S., Wu, X., Zhu, J., Changela, A., Schmidt, S.D., Yang, Y., Zhou, T., Phogat, S., Mascola, J.R.*, et al.* (2010). Crystal structure of PG16 and chimeric dissection with somatically related PG9: structure-function analysis of two quaternary-specific antibodies that effectively neutralize HIV-1. J Virol *84*, 8098-8110.

Pancera, M., Shahzad-Ul-Hussan, S., Doria-Rose, N.A., McLellan, J.S., Bailer, R.T., Dai, K., Loesgen, S., Louder, M.K., Staupe, R.P., Yang, Y.*, et al.* (2013). Structural basis for diverse N-glycan recognition by HIV-1-neutralizing V1-V2-directed antibody PG16. Nat Struct Mol Biol *20*, 804-813.

Pancera, M., Zhou, T., Druz, A., Georgiev, I.S., Soto, C., Gorman, J., Huang, J., Acharya, P., Chuang, G.Y., Ofek, G.*, et al.* (2014). Structure and immune recognition of trimeric pre-fusion HIV-1 Env. Nature *514*, 455-461.

Pejchal, R., Walker, L.M., Stanfield, R.L., Phogat, S.K., Koff, W.C., Poignard, P., Burton, D.R., and Wilson, I.A. (2010). Structure and function of broadly reactive antibody PG16 reveal an H3 subdomain that mediates potent neutralization of HIV-1. Proc Natl Acad Sci U S A *107*, 11483-11488.

Pettersen, E.F., Goddard, T.D., Huang, C.C., Couch, G.S., Greenblatt, D.M., Meng, E.C., and Ferrin, T.E. (2004). UCSF Chimera--a visualization system for exploratory research and analysis. J Comput Chem *25*, 1605-1612.

Pugach, P., Ozorowski, G., Cupo, A., Ringe, R., Yasmeen, A., de Val, N., Derking, R., Kim, H.J., Korzun, J., Golabek, M.*, et al.* (2015). A native-like SOSIP.664 trimer based on an HIV-1 subtype B env gene. J Virol *89*, 3380-3395.

Roberts, J.D., Bebenek, K., and Kunkel, T.A. (1988). The accuracy of reverse transcriptase from HIV-1. Science *242*, 1171-1173.

Rohou, A., and Grigorieff, N. (2015). CTFFIND4: Fast and accurate defocus estimation from electron micrographs. J Struct Biol *192*, 216-221.

Sanders, R.W., Derking, R., Cupo, A., Julien, J.P., Yasmeen, A., de Val, N., Kim, H.J., Blattner, C., de la Pena, A.T., Korzun, J.*, et al.* (2013). A next-generation cleaved, soluble HIV-1 Env Trimer, BG505 SOSIP.664 gp140, expresses multiple epitopes for broadly neutralizing but not non-neutralizing antibodies. PLoS Pathog *9*, e1003618.

Saphire, E.O., Parren, P.W., Pantophlet, R., Zwick, M.B., Morris, G.M., Rudd, P.M., Dwek, R.A., Stanfield, R.L., Burton, D.R., and Wilson, I.A. (2001). Crystal structure of a neutralizing human IGG against HIV-1: a template for vaccine design. Science *293*, 1155-1159.

Scanlan, C.N., Offer, J., Zitzmann, N., and Dwek, R.A. (2007). Exploiting the defensive sugars of HIV-1 for drug and vaccine design. Nature *446*, 1038.

Scharf, L., Scheid, J.F., Lee, J.H., West, A.P., Jr., Chen, C., Gao, H., Gnanapragasam, P.N., Mares, R., Seaman, M.S., Ward, A.B.*, et al.* (2014). Antibody 8ANC195 reveals a site of broad vulnerability on the HIV-1 envelope spike. Cell reports *7*, 785-795.

Scharf, L., Wang, H., Gao, H., Chen, S., McDowall, A.W., and Bjorkman, P.J. (2015). Broadly Neutralizing Antibody 8ANC195 Recognizes Closed and Open States of HIV-1 Env. Cell *162*, 1379-1390.

Scharf, L., West, A.P., Sievers, S.A., Chen, C., Jiang, S., Gao, H., Gray, M.D., McGuire, A.T., Scheid, J.F., Nussenzweig, M.C.*, et al.* (2016). Structural basis for germline antibody recognition of HIV-1 immunogens. Elife *5*.

Scheid, J.F., Mouquet, H., Feldhahn, N., Seaman, M.S., Velinzon, K., Pietzsch, J., Ott, R.G., Anthony, R.M., Zebroski, H., Hurley, A.*, et al.* (2009). Broad diversity of neutralizing antibodies isolated from memory B cells in HIV-infected individuals. Nature *458*, 636-640.

Scheid, J.F., Mouquet, H., Ueberheide, B., Diskin, R., Klein, F., Olivera, T.Y., Pietzsch, J., Fenyo, D., Abadir, A., Velinzon, K.*, et al.* (2011). Sequence and Structural Convergence of Broad and Potent HIV Antibodies That Mimic CD4 Binding. Science *333*, 1633-1637.

Scheres, S.H. (2012). RELION: implementation of a Bayesian approach to cryo-EM structure determination. J Struct Biol *180*, 519-530.

Scheres, S.H., and Chen, S. (2012). Prevention of overfitting in cryo-EM structure determination. Nat Methods *9*, 853-854.

Schrödinger, L. (2011). The PyMOL Molecular Graphics System (The PyMOL Molecular Graphics System).

Sheskin, D. (2004). Handbook of Parametric and Nonparametric Statistical Procedures, 3rd edn (Boca Raton: Chapman & Hall/CRC).

Shingai, M., Nishimura, Y., Klein, F., Mouquet, H., Donau, O.K., Plishka, R., Buckler-White, A., Seaman, M., Piatak, M., Jr., Lifson, J.D*., et al.* (2013). Antibody-mediated immunotherapy of macaques chronically infected with SHIV suppresses viraemia. Nature *503*, 277-280.

Song, Y., DiMaio, F., Wang, R.Y., Kim, D., Miles, C., Brunette, T., Thompson, J., and Baker, D. (2013). High-resolution comparative modeling with RosettaCM. Structure *21*, 1735-1742.

Stadtmueller, B.M., Bridges, M.D., Dam, K.-M., Lerch, M.T., Huey-Tubman, K.E., Hubbell, W.L., and Bjorkman, P.J. (2018). DEER Spectroscopy Measurements Reveal Multiple Conformations of HIV-1 SOSIP Envelopes that Show Similarities with Envelopes on Native Virions. Immunity.

Stanfield, R.L., Zemla, A., Wilson, I.A., and Rupp, B. (2006). Antibody elbow angles are influenced by their light chain class. J Mol Biol *357*, 1566-1574.

Stewart-Jones, G.B.E., Soto, C., Lemmin, T., Chuang, G.-Y., Druz, A., Kong, R., Thomas, P.V., Wagh, K., Zhou, T., Behrens, A.-J*., et al.* (2016). Trimeric HIV-1-Env Structures Define Glycan Shields from Clades A, B, and G. Cell *165*, 813-826.

Sullivan, N., Sun, Y., Sattentau, Q., Thali, M., Wu, D., Denisova, G., Gershoni, J., Robinson, J., Moore, J., and Sodroski, J. (1998). CD4-Induced conformational changes in the human immunodeficiency virus type 1 gp120 glycoprotein: consequences for virus entry and neutralization. J Virol *72*, 4694-4703.

Sundquist, W.I., and Kräusslich, H.-G. (2012). HIV-1 assembly, budding, and maturation. Cold Spring Harbor perspectives in medicine, a006924.

Swindells, M.B., Porter, C.T., Couch, M., Hurst, J., Abhinandan, K.R., Nielsen, J.H., Macindoe, G., Hetherington, J., and Martin, A.C. (2017). abYsis: Integrated Antibody Sequence and Structure-Management, Analysis, and Prediction. J Mol Biol *429*, 356-364.

Tang, G., Peng, L., Baldwin, P.R., Mann, D.S., Jiang, W., Rees, I., and Ludtke, S.J. (2007). EMAN2: an extensible image processing suite for electron microscopy. J Struct Biol *157*, 38-46.

Tange, O. (2011). Gnu parallel-the command-line power tool. The USENIX Magazine *36*, 42-47.

Tiller, T., Tsuiji, M., Yurasov, S., Velinzon, K., Nussenzweig, M.C., and Wardemann, H. (2007). Autoreactivity in human IgG+ memory B cells. Immunity *26*, 205-213.

Tran, E.E., Borgnia, M.J., Kuybeda, O., Schauder, D.M., Bartesaghi, A., Frank, G.A., Sapiro, G., Milne, J.L., and Subramaniam, S. (2012). Structural mechanism of trimeric HIV-1 envelope glycoprotein activation. PLoS Pathog *8*, e1002797.

Trkola, A., Dragic, T., Arthos, J., Binley, J.M., Olson, W.C., Allaway, G.P., Cheng-Mayer, C., Robinson, J., Maddon, P.J., and Moore, J.P. (1996). CD4-dependent, antibody-sensitive interactions between HIV-1 and its co-receptor CCR-5. Nature *384*, 184.

Walker, L.M., Huber, M., Doores, K.J., Falkowska, E., Pejchal, R., Julien, J.P., Wang, S.K., Ramos, A., Chan-Hui, P.Y., Moyle, M.*, et al.* (2011). Broad neutralization coverage of HIV by multiple highly potent antibodies. Nature *477*, 466–470.

Walker, L.M., Phogat, S.K., Chan-Hui, P.Y., Wagner, D., Phung, P., Goss, J.L., Wrin, T., Simek, M.D., Fling, S., Mitcham, J.L.*, et al.* (2009). Broad and Potent Neutralizing Antibodies from an African Donor Reveal a New HIV-1 Vaccine Target. Science *326*, 285-289.

Walls, A.C., Tortorici, M.A., Bosch, B.-J., Frenz, B., Rottier, P.J., DiMaio, F., Rey, F.A., and Veesler, D. (2016). Cryo-electron microscopy structure of a coronavirus spike glycoprotein trimer. Nature *531*, 114.

Walls, A.C., Tortorici, M.A., Snijder, J., Xiong, X., Bosch, B.-J., Rey, F.A., and Veesler, D. (2017). Tectonic conformational changes of a coronavirus spike glycoprotein promote membrane fusion. Proceedings of the National Academy of Sciences, 201708727.

Wang, H., Barnes, C.O., Yang, Z., Nussenzweig, M.C., and Bjorkman, P.J. (2018). Partially Open HIV-1 Envelope Structures Exhibit Conformational Changes Relevant for Coreceptor Binding and Fusion. Cell Host Microbe *24*, 579-592 e574.

Wang, H., Cohen, A.A., Galimidi, R.P., Gristick, H.B., Jensen, G.J., and Bjorkman, P.J. (2016a). Cryo-EM structure of a CD4-bound open HIV-1 envelope trimer reveals structural rearrangements of the gp120 V1V2 loop. Proc Natl Acad Sci U S A *113*, E7151-E7158.

Wang, H., Gristick, H.B., Scharf, L., West, A.P., Galimidi, R.P., Seaman, M.S., Freund, N.T., Nussenzweig, M.C., and Bjorkman, P.J. (2017). Asymmetric recognition of HIV-1 Envelope trimer by V1V2 loop-targeting antibodies. Elife *6*.

Wang, R.Y.-R., Song, Y., Barad, B.A., Cheng, Y., Fraser, J.S., and DiMaio, F. (2016b). Automated structure refinement of macromolecular assemblies from cryo-EM maps using Rosetta. Elife *5*.

Ward, A.B., and Wilson, I.A. (2017). The HIV-1 envelope glycoprotein structure: nailing down a moving target. Immunol Rev *275*, 21-32.

Wardemann, H., Yurasov, S., Schaefer, A., Young, J.W., Meffre, E., and Nussenzweig, M.C. (2003). Predominant autoantibody production by early human B cell precursors. Science *301*, 1374-1377.

Weissenhorn, W., Dessen, A., Harrison, S.C., Skehel, J.J., and Wiley, D.C. (1997). Atomic structure of the ectodomain from HIV-1 gp41. Nature *387*, 426-430.

Wells, J.A., and DeVos, A.M. (1996). Hematopoietic receptor complexes. Ann Rev Biochem *65*, 609-634.

West, A.P., Jr., Galimidi, R.P., Foglesong, C.P., Gnanapragasam, P.N., Klein, J.S., and Bjorkman, P.J. (2010). Evaluation of CD4-CD4i antibody architectures yields potent, broadly cross-reactive anti-human immunodeficiency virus reagents. J Virol *84*, 261-269.

West, A.P., Jr., Galimidi, R.P., Gnanapragasam, P.N., and Bjorkman, P.J. (2012). Single-Chain Fv-Based Anti-HIV Proteins: Potential and Limitations. J Virol *86*, 195-202.

West, A.P., Jr., Scharf, L., Horwitz, J., Klein, F., Nussenzweig, M.C., and Bjorkman, P.J. (2013). Computational analysis of anti-HIV-1 antibody neutralization panel data to identify potential functional epitope residues. Proc Natl Acad Sci U S A *110*, 10598-10603.

West, A.P., Jr., Scharf, L., Scheid, J.F., Klein, F., Bjorkman, P.J., and Nussenzweig, M.C. (2014). Structural Insights on the Role of Antibodies in HIV-1 Vaccine and Therapy. Cell *156*, 633-648.

White, T.A., Bartesaghi, A., Borgnia, M.J., de la Cruz, M.J., Nandwani, R., Hoxie, J.A., Bess, J.W., Lifson, J.D., Milne, J.L., and Subramaniam, S. (2011). Three-dimensional structures of soluble CD4-bound states of trimeric simian immunodeficiency virus envelope glycoproteins determined by using cryo-electron tomography. J Virol *85*, 12114-12123.

White, T.A., Bartesaghi, A., Borgnia, M.J., Meyerson, J.R., de la Cruz, M.J., Bess, J.W., Nandwani, R., Hoxie, J.A., Lifson, J.D., Milne, J.L*., et al.* (2010). Molecular architectures of trimeric SIV and HIV-1 envelope glycoproteins on intact viruses: strain-dependent variation in quaternary structure. PLoS Pathog *6*, e1001249.

Wyatt, P.J. (1993). Light scattering and the absolute characterization of macromolecules. Analytica Chimica Acta *272*, 1-40.

Wyatt, R., and Sodroski, J. (1998). The HIV-1 envelope glycoproteins: fusogens, antigens, and immunogens. Science *280*, 1884-1888.

Xiang, S.H., Doka, N., Choudhary, R.K., Sodroski, J., and Robinson, J.E. (2002). Characterization of CD4-induced epitopes on the HIV type 1 gp120 envelope glycoprotein recognized by neutralizing human monoclonal antibodies. AIDS Res Hum Retroviruses *18*, 1207-1217.

Zheng, S.Q., Keszthelyi, B., Branlund, E., Lyle, J.M., Braunfeld, M.B., Sedat, J.W., and Agard, D.A. (2007). UCSF tomography: an integrated software suite for real-time electron microscopic tomographic data collection, alignment, and reconstruction. J Struct Biol *157*, 138-147.

Zheng, S.Q., Palovcak, E., Armache, J.P., Verba, K.A., Cheng, Y., and Agard, D.A. (2017). MotionCor2: anisotropic correction of beam-induced motion for improved cryo-electron microscopy. Nat Methods *14*, 331-332.

Zhou, T., Xu, L., Dey, B., Hessell, A.J., Van Ryk, D., Xiang, S.H., Yang, X., Zhang, M.Y., Zwick, M.B., Arthos, J.*, et al.* (2007). Structural definition of a conserved neutralization epitope on HIV-1 gp120. Nature *445*, 732-737.

Zhu, P., Liu, J., Bess, J., Jr., Chertova, E., Lifson, J.D., Grise, H., Ofek, G.A., Taylor, K.A., and Roux, K.H. (2006). Distribution and three-dimensional structure of AIDS virus envelope spikes. Nature *441*, 847-852.